Dynamics and Control of Flexure-based Large Range Nanopositioning Systems

by

Gaurav K Parmar

A dissertation submitted in partial fulfillment
of the requirements for the degree of
Doctor of Philosophy
(Department of Mechanical Engineering)
in The University of Michigan
2014

Doctoral Committee:

Associate Professor Shorya Awtar, Chair
Assistant Professor Kira L Barton
Associate Professor Heath Hofmann
Assistant Professor Chinedum E Okwudire

To my Parents

ACKNOWLEDGEMENTS

I would like to thank my advisor, Professor Shorya Awtar, for his guidance and support throughout my graduate studies. I am also grateful to Professor Kira Barton, Professor Heath Hofmann, and Professor Chinedum Okwudire, for agreeing to be in my doctoral committee and providing much needed comments and criticism. I would like to also thank Dr. John Kramar at the National Institute of Science and Technology, for partially funding this research through a Measurement Science and Engineering Fellowship.

A big thank you goes to my colleagues at the Precision Systems Design Laboratory for all the help and support they offered me over the years. I would like to specifically acknowledge collaborative efforts within our group. The work for the moving magnet actuator in Chapter II was done is collaboration with David Hiemstra. Leqing Cui contributed to the dynamic modeling of XY flexure mechanism in Chapter IV and Kai Wu helped with the system identification experiments on the XY nanopositioning system.

Finally, I dedicate this thesis to my parents, whose unconditional love and countless sacrifices have made my education possible.

TABLE OF CONTENTS

CHAPTER

LIST OF FIGURES

Figure

LIST OF TABLES

Table

LIST OF APPENDICES

Appendix

ABSTRACT

Dynamics and Control of Flexure-based Large Range Nanopositioning Systems

by

Gaurav K Parmar

Chair: Shorya Awtar

The objective of this thesis is to demonstrate desktop-size and cost-effective flexure-based multi-axis nanopositioning capability over a motion range of several millimeters per axis. Increasing the motion range will overcome one of the main drawbacks of existing nanopositioning systems, thereby significantly improving the coverage area in nanometrology and nanomanufacturing applications.

A single-axis nanopositioning system, comprising a symmetric double parallelogram flexure bearing and a traditional-architecture moving magnet actuator, is designed, fabricated, and tested. A figure of merit for the actuator is derived and shown to directly impact the system-level trade-offs in terms of range, resolution, bandwidth, and temperature rise. While linear feedback controllers provide good positioning performance for point-to-point commands, the tracking error for dynamic commands prove to be inadequate due to the nonlinearities in the actuator and its driver. To overcome this, an iterative learning controller is implemented in conjunction with linear feedback to reduce the periodic component of the tracking error by more than two orders of magnitude. Experimental results demonstrate 10 nm RMS tracking error over 8 mm motion range in response to a 2 Hz bandlimited triangular command.

For the XY nanopositioning system, a lumped-parameter model of an existing XY flexure bearing is developed in order to understand the unexplained variation observed in the transfer function zeros over the operating range of motion. It is shown that the kinematic coupling, due to geometric nonlinearities in the beam mechanics, and small dimensional asymmetry, due to manufacturing tolerances, may conspire to produce complex-conjugate nonminimum phase zeros at certain operating points in the system's workspace. This phenomenon significantly restricts the overall performance of the feedback control system. After intentional use of large asymmetry is employed to overcome this problem, independent feedback and iterative learning controllers are implemented along each axis. Experimental results demonstrate 20 nm RMS radial tracking error while traversing a 2 mm diameter circle at 2 Hz.

Moving forward, investigating new architectures for the moving magnet actuator having an improved figure of merit would ease the system-level trade-offs and help achieve better performance. Also, the dynamic modeling effort could be extended to gain physical explanation for the existence of complex-conjugate nonminimum phase zeros in mechanical structures.

CHAPTER I

Introduction and Overview

1.1 Introduction

A nanopositioning system or a nanopositioner is a mechatronic motion system capable of generating and measuring motion with nanometric *motion quality.* Motion quality refers to precision, accuracy, and resolution. A nanopositioning system generally comprises a bearing for motion guidance, actuators that generate the motion, associated actuator drivers, sensors that measure the motion, associated signal conditioning electronics, a control algorithm to meet the required motion specifications, control hardware that executes the control algorithm, a power source, and often a computer-based user interface. Some nanopositioning systems may further incorporate a transmission that transmits motion from the actuator to the bearing while providing some modulation or isolation, and damping elements that help reject undesired vibrations. Although it is the physical components and their integration that makes a nanopositioning system capable of achieving nanometric motion quality, the motion quality ultimately depends upon the closed-loop dynamic performance provided by the control system.

The motion quality of a nanopositioning system is generally characterized by its resolution, precision, and accuracy. These terms are described qualitatively in Fig. 1.1 [1] in a point-to-point positioning setup. Precision is the ability of the system to go

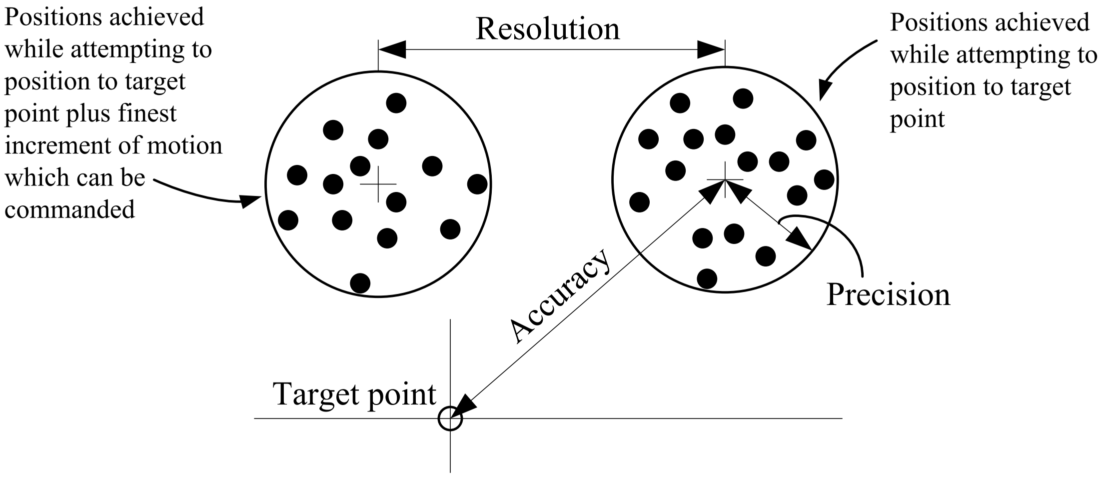

Fig. 1.1: Qualitative illustration of accuracy, precision and resolution [1]

through the same commanded position again and again from either direction. Accuracy is the measure of the closeness or agreement between the commanded position and the measured position. Resolution can be thought as the smallest increment in the position such that the consecutive steps can be differentiated. The motion quality of the nanopositioner is the major factor that directly influences the performance attributes of its applications. A more thorough discussion about the definitions of the abovementioned performance specifications and systematic characterization procedure to evaluate them can be found in [2].

1.2 Applications

Due to their high motion quality, there are several existing and emerging nanotechnology applications where nanopositioners are becoming increasingly important. References [3, 4] provide a good overview of numerous applications in the field of semiconductors, data storage, optoelectronics, biotechnology, nanomanufacturing, nanometrology etc., in which a nanopositioner is a key enabling component. For example, as shown in the schematic in Fig. 1.2, nanopositioners form an important subsystem of various scanning probe microscopes (SPM) such as atomic force mi-

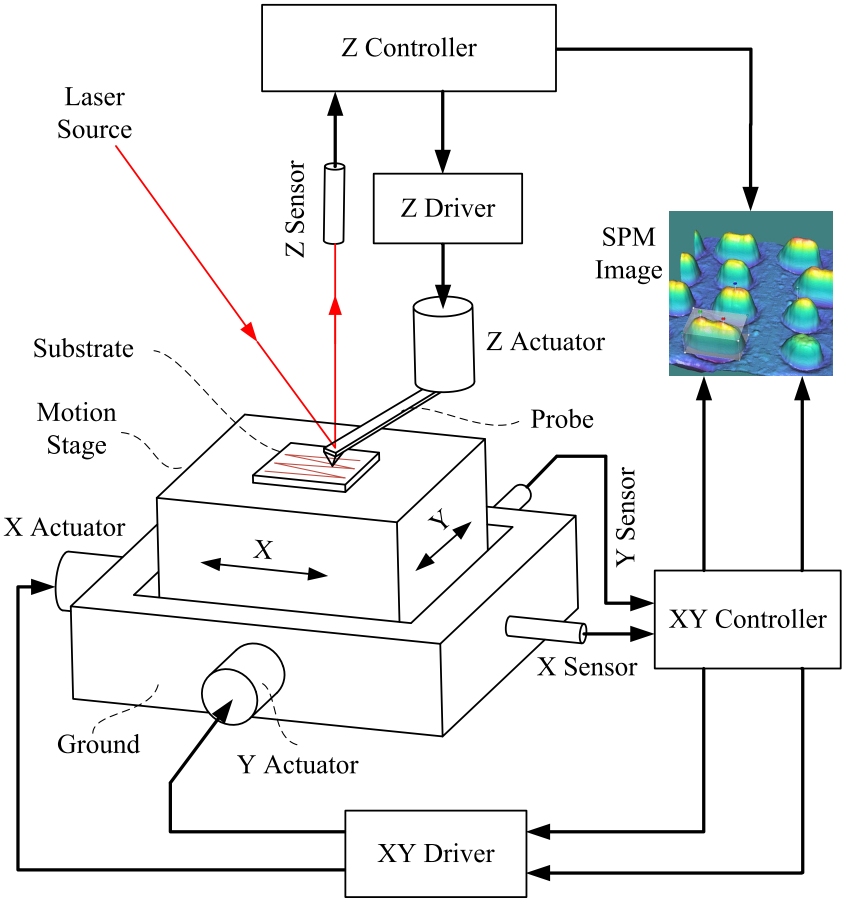

Fig. 1.2: An XY nanopositioning system employed in scanning probe microscopy

croscopes (AFM) and scanning tunneling microscopes (STM). In these applications, the nanopositioner moves the sample or the probe in a raster pattern with nanometric motion quality. The probe, mounted on a flexible cantilever, follows the surface profile, and this movement is detected by a sensor. This measurement, along with the position measurements from the nanopositioner, provides a three dimensional topographical image of the substrate. In addition to visualizing small features with dimensions down to the size of atoms and molecules, SPM technology is also utilized to characterize many surface-specific properties at the nanoscale such as magnetism, friction, thermal conductivity, etc [5]. Another important area of nanotechnology enabled by emergence of SPMs is that of nanomanipulation. In one such technique, commonly known as scanning probe lithography (SPL), a microscopic probe is moved across the substrate to create nanoscale features by selective deposition or removal of nanoparticles [6], while the setup remains similar to that shown in Fig. 1.2.

In each of the aforementioned applications, the nanometric motion quality remains a prerequisite. Specifically, the spatial resolution of the image or the pattern will depend, in part, on the resolution of the nanopositioning system. Also, the lack of precision or accuracy of the nanopositioner will manifest itself as the distortion of the image or the pattern. In addition to this, the substrate size and the process throughput are directly dependent on the motion range and the scanning speed of the underlying nanopositioning system, respectively.

1.3 Motivation for Large Motion Range

Over the years there has been a tremendous growth in the field on precision positioning systems. The prediction by Professor Norio Taniguchi in 1974 [7], that "*the ultra-precision machines would be capable of achieving 1 nm machine accuracies by the year 2000*", has been proven to be true. A comparison of various precision positioning system is provided in Fig. 1.3 [8], in which they are plotted with motion range and motion quality along X and Y axes respectively. From this figure, the trade-off between the motion range and motion quality across the spectrum is clearly evident.

The limited motion range of the currently available nanopositioning system can be attributed to the use of flexure-based bearings and piezoelectric actuators for motion guidance and actuation, respectively. While these components are inherently capable of producing high motion quality due to lack of friction and backlash, their motion range is limited to a few hundred microns [3, 4, 9, 10]. On the other hand, traditional motion systems, based on roller or slider bearings, that can provide large motion range from millimeter to meter have their motion quality limited to hundreds of nanometers [11–13]. This trade-off is also apparent from a comparison of various off-

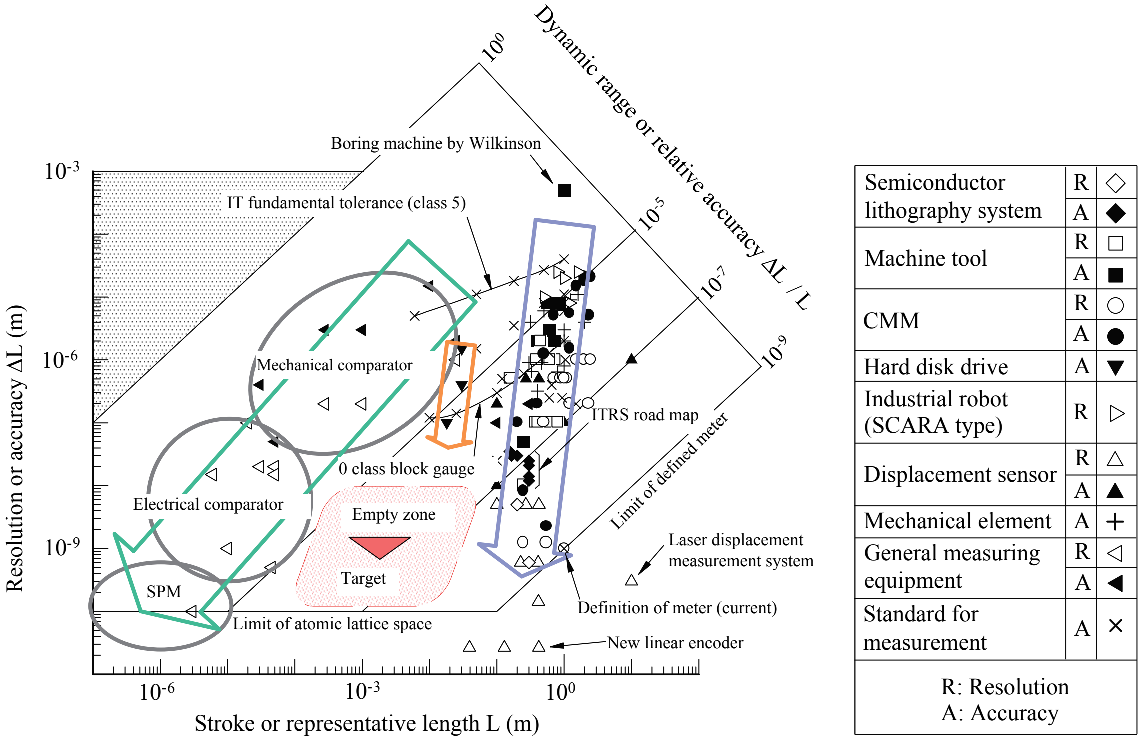

Fig. 1.3: Broad classification of precision positioning systems based on their range and resolution [8]

the-shelf commercially available nanopositioning systems [14–21] shown in Table 1.1. The comparison is also shown in a graphical form, in Fig. 1.4, where it can be easily seen that the *dynamic range* of all listed nanopositioning systems is around 10^5. Here, dynamic range refers to the ratio of motion range over motion quality. The limited dynamic range of nanopositioning systems has restricted the scope of applications of various technologies, of which nanopositioning systems are a key component. There has been a long-standing need for nanopositioning systems which can achieve large motion range ($\sim$ 10 mm) and high motion quality ($<$ 10 nm) simultaneously. This corresponds to a dynamic range greater than 10^6, also shown as target specification in Fig. 1.4.

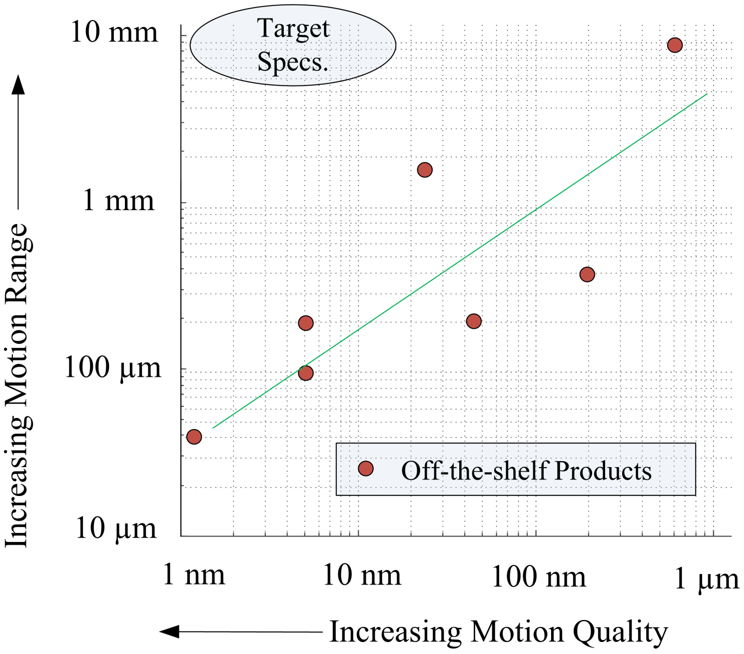

Fig. 1.4: Comparison of various commercially available off-the-shelf nanopositioning systems based on data provided in Table 1.1

1.4 Applications of Large Range Nanopositioning Systems

Limited motion range of nanopositioning systems have in turn restricted the scope of scanning probe microscopy and scanning probe lithography techniques to substrate sizes on the order of 200 µm × 200 µm. In the absence of nanopositioning systems with adequate motion range, a common approach to cover large area substrates has been to use an array of parallel probes both for imaging and surface modification [22–24]. One such effort is shown in Fig. 1.5(d), in which an array of 10 parallel probes were installed on a typical AFM to image a 2 mm × 2 mm integrated circuit chip [22]. But there are still significant practical challenges that lie ahead in terms of sensing and control of individual tips to achieve uniform tip-surface interaction, tip-tip spacing, sensitivity calibration of the individual tips, etc. [23, 24]. Another popular approach has been to merge multiple localized scan images to form a large image [25, 26]. This is commonly known as *stitching* of images. However, stitching generally leads to image distortion at the interfaces of merged images due to lack of

Table 1.1: Comparison of various commercially available off-the-shelf nanopositioning systems

Vendor, Product No.	**Range** µm × µm	**Resolution** nm	**Precision** nm	**Accuracy** nm
PhysikInstrumente, P-542.2 [14]	200 × 200	0.7	5	60
Queensgate, NPS-XY-100A [19]	100 × 100	0.5	5	10
Mad City Labs, NanoBio200 [18]	200 × 200	0.4	NA	NA
Piezosystem Jena, Nano PXY200 [15]	200 × 200	4	45	180
nPoint, NPXY400A [17]	400 × 400	1.5	120	200
PhysikInstrumente, P-629.2 [21]	1,800 × 1,800	3.5	28	540
Discovery Tech., NTS10 [16]	10,000 × 10,000	50	500	3,000
Aerotech, ANT95-25-XY-PLUS [20]	25,000 × 25,000	1	150	500

'NA' implies information was not provided by the vendor

precision and accuracy in the positioning stages used for moving the substrate from one localized area to another [25–28]. Increasing the instrument range to several millimeters will enable the use of large-sized substrates in several applications, some of which are briefly described below:

1. Inspection of optical components, e.g., automotive reflectors, for nanoscale surface quality and defects [29]. In this case, the use of optical and mechanical profilometers is limited as reflector material is generally soft and transparent (Fig. 1.5 (a))
2. Large area 3D measurement of micro-structured surfaces such as holograms, anti-reflective films, measurement standards etc. (Fig. 1.5(b)) [30], quality control of LCD panels (Fig. 1.5(c)) [25].
3. Measurement of micro-roughness and flatness [31] with increased lateral resolution. This provides a clear advantage over stylus profilometers, which have a limited lateral resolution due to the large radius of the stylus tip.
4. High resolution imaging of integrated circuits over square centimeter areas (Fig. 1.5(d)) [22].
5. Characterization of millimeter sized 1D and 2D grating scales standards used for calibration purposes (Fig. 1.5(e)) [32, 33].
6. High resolution lithography in niche microelectronics, where integrated circuit chips typically have nanometer scale features over square centimeter areas (Fig. 1.5(f)) [22].
7. Deposition of molecules or other materials with nanometric feature size over large areas (Fig. 1.5(g)) [34].
8. Microscopic quality control of tablets in the pharmaceutical industry. Confocal Raman microscopy is used along with large area scanning to study the distribution

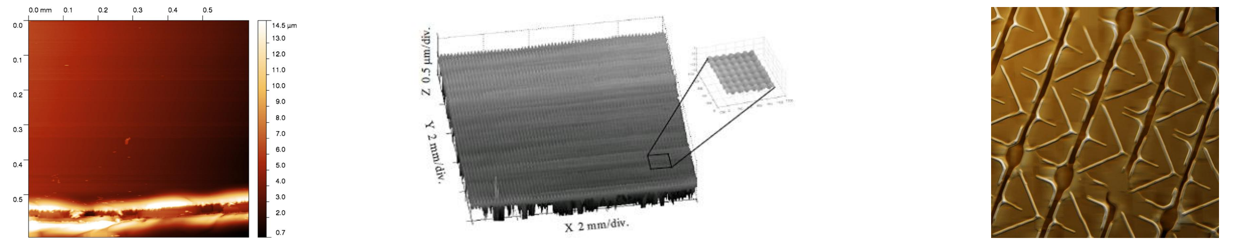

(a) 0.6 mm × 0.6 mm AFM image of an automotive reflector with a large scratch [29]

(b) 10 mm × 10 mm AFM image of a sinusoidal metrology standard [30]

(c) 0.56 mm × 0.57 mm stitched AFM image of an LCD panel [25]

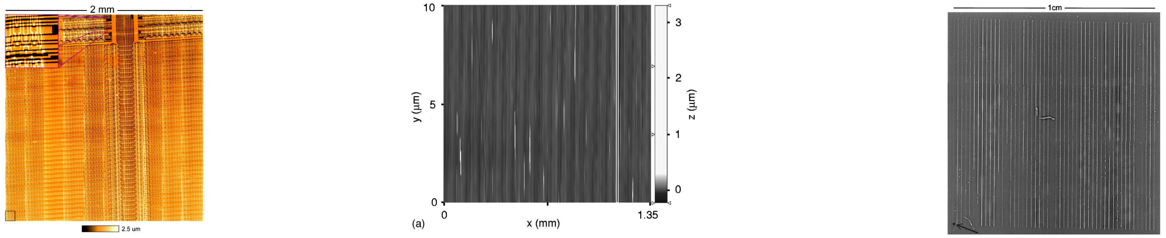

(d) 2 mm × 2 mm AFM image of an integrated circuit chip [22]

(e) 1.35 mm × 1.35 mm SPM measurement of a 1D grating scale [32]

(f) 10 mm × 10 mm Parallel probe AFM lithography [22]

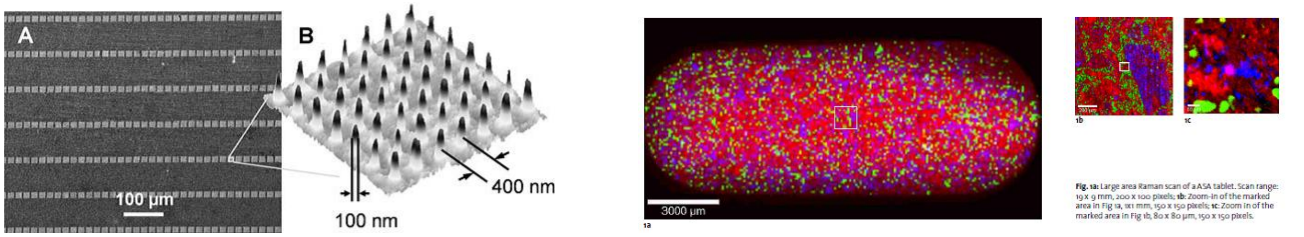

(g) 0.5 mm × 0.5 mm SEM image of part of 88,000,000 gold dot array deposited on an oxidized silicon substrate [34]

(h) 19 mm × 9 mm Large area Raman scan of a tablet with 80 µm × 80 µm inset images [35]

Fig. 1.5: Applications of large range nanopositioning systems

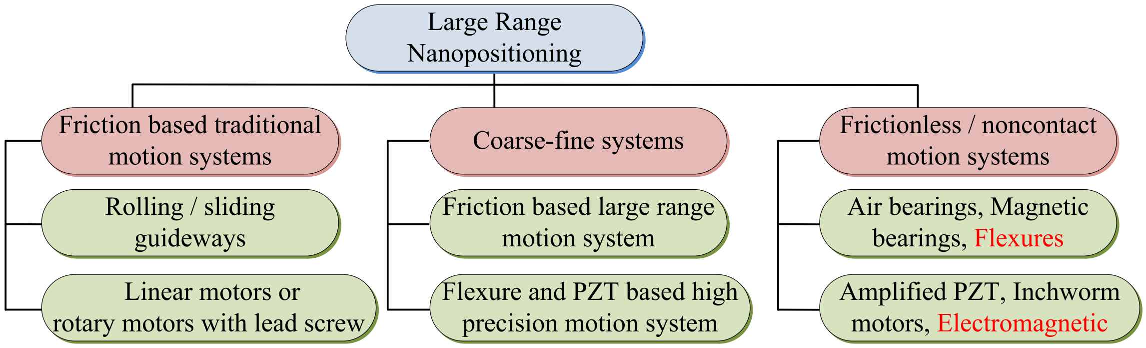

Fig. 1.6: Classification of large range nanopositioning systems

of chemicals along the entire tablet with resolutions down to 200 nm. (Fig. 1.5(h)) [35]

1.5 Prior Art[1]

The ongoing research efforts in the area of large range translational nanopositioning systems can be broadly classified into three categories, as shown in Fig. 1.6.

The first category is of positioning systems that have friction and backlash in one or more of their physical components, such as the bearing or transmission (e.g., see Fig. 1.7(a)). The motion stage in these cases is supported by rolling [36, 37] or sliding [38–40] guideways. Either direct-drive linear motors [39–41] or rotary motors coupled with lead-screw drives [36–38, 42] are used for actuation. The presence of friction limits the motion quality of these tradition motion systems to hundreds of nanometers [10–12, 43–46]. For these systems, linear feedback controllers do not offer adequate positioning performance due to the nonlinear and parameter-varying characteristics of friction, especially in the micro-dynamic regime [43]. Implementation of advanced controllers [36, 37, 40] has shown some performance improvements over linear feedback, especially for point-to-point positioning. However, achieving

---

[1] Further prior art is also mentioned in Sections 2.1, 3.1, 4.3, relevant to the corresponding chapters.

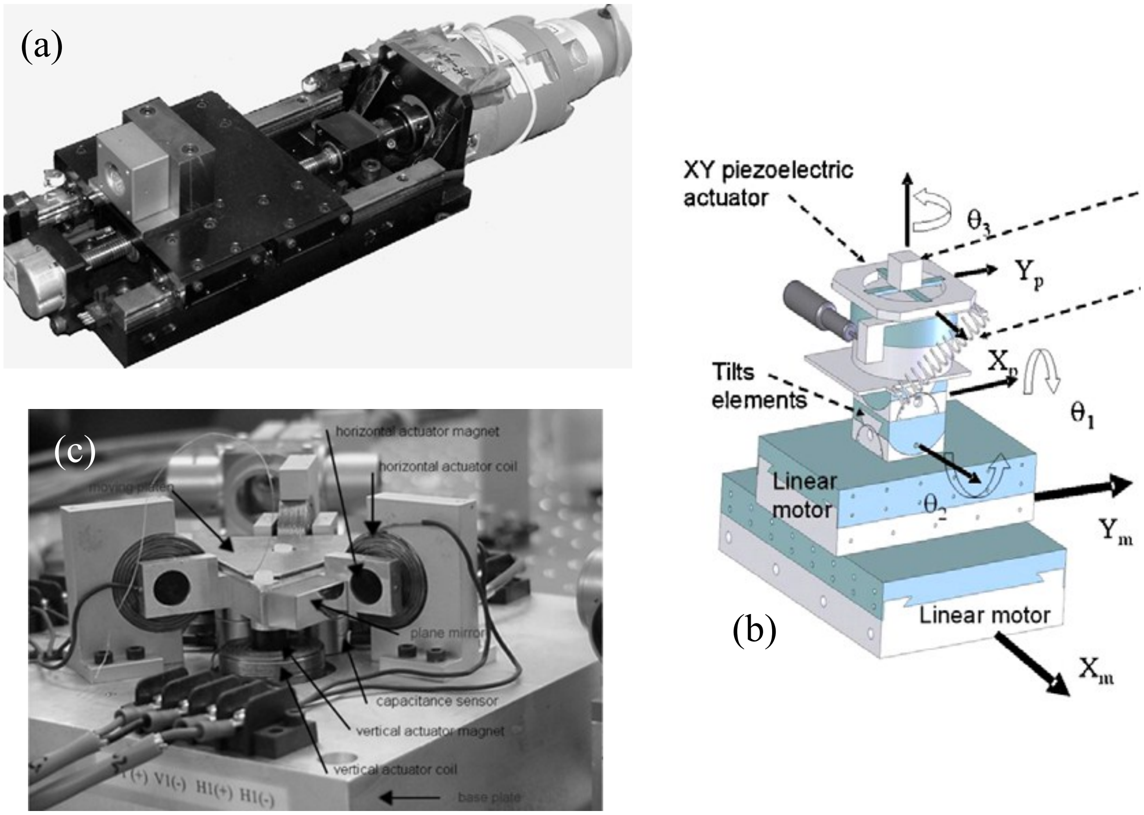

Fig. 1.7: Examples of large range nanopositioning systems. (a) Friction based traditional motion system: A DC motor coupled with lead screw with a linear ball guide [36]. (b) Coarse-fine motion system: Coarse stage consist of an electromagnetic motor driven crossed-roller stage, fine stage consist of a PZT driven flexure stage [41]. (c) Frictionless / non-contact motion system: Magnetically levitated stage with moving magnet actuators [47].

nanometric tracking performance for dynamic commands remains a challenge.

To overcome the performance limitations associated with friction, another approach has been to mount a small range, high motion quality positioning system (*fine stage*) on top of a large range, friction-based traditional motion system (*coarse stage*) [38, 39, 41, 42]. Fig. 1.7(b) shows one such example where the idea is to use the fine stage to compensate for the positioning errors of the coarse stage, thereby improving the overall positioning performance. The major challenge here lies in the control system design of the resulting multi-input multi-output (MIMO) system to ensure coordination between the coarse and fine motion systems [42].

Separately, there has been a considerable effort focused on positioning systems that are based on non-contact and frictionless operation (e.g., see Fig. 1.7(c)). These systems rely on magnetic [47–49], aerostatic [50–52], or flexure bearings [8, 53] for motion guidance, and generally employ direct-drive electromagnetic actuators. Each of these present unique control design challenges to achieve nanometric motion quality. For example, electromagnetic bearings as well as actuators suffer from force-stroke nonlinearities [47]. Also, the noise and distortion in the driver degrades the positioning performance [8]. Air bearings exhibit sustained vibrations due to both load-bearing as well as motion direction [54, 55]. Although aerostatic bearings and magnetic bearings are employed in lithographic steppers and scanners used for semiconductor manufacturing and inspection that require large range and nanometric motion quality at relatively higher speeds [56], these machines are not targeted towards niche low-cost desktop applications mentioned above. Such specifications in a cost-effective and desktop-sized setup is still a challenging problem, which is the targeted application of this work.

In contrast to magnetic and aerostatic bearings, flexure bearings offer unmatched simplicity in design and operation, and lower manufacturing and operating costs, and are therefore the most common bearing choice for desktop-size nanopositioning systems. Their monolithic construction entirely eliminates friction and backlash leading to sub-nanometric precision, zero maintenance, and potentially infinite life. The main limitation of flexure bearings has been their small range of motion, which in turn has restricted the range of flexure-based nanopositioning systems. However, recent advances [57–60] have shown up to 10 mm motion range in multi-axis flexure bearings, which is sufficient for intended applications. A few examples of such large range single-axis and parallel-kinematic, multi-axis flexure bearings with translational degrees of freedom (DoF) are shown in Fig. 1.8. Flexure mechanisms (a) and (c) shown in the figure are used in this work. It is important to note that although,

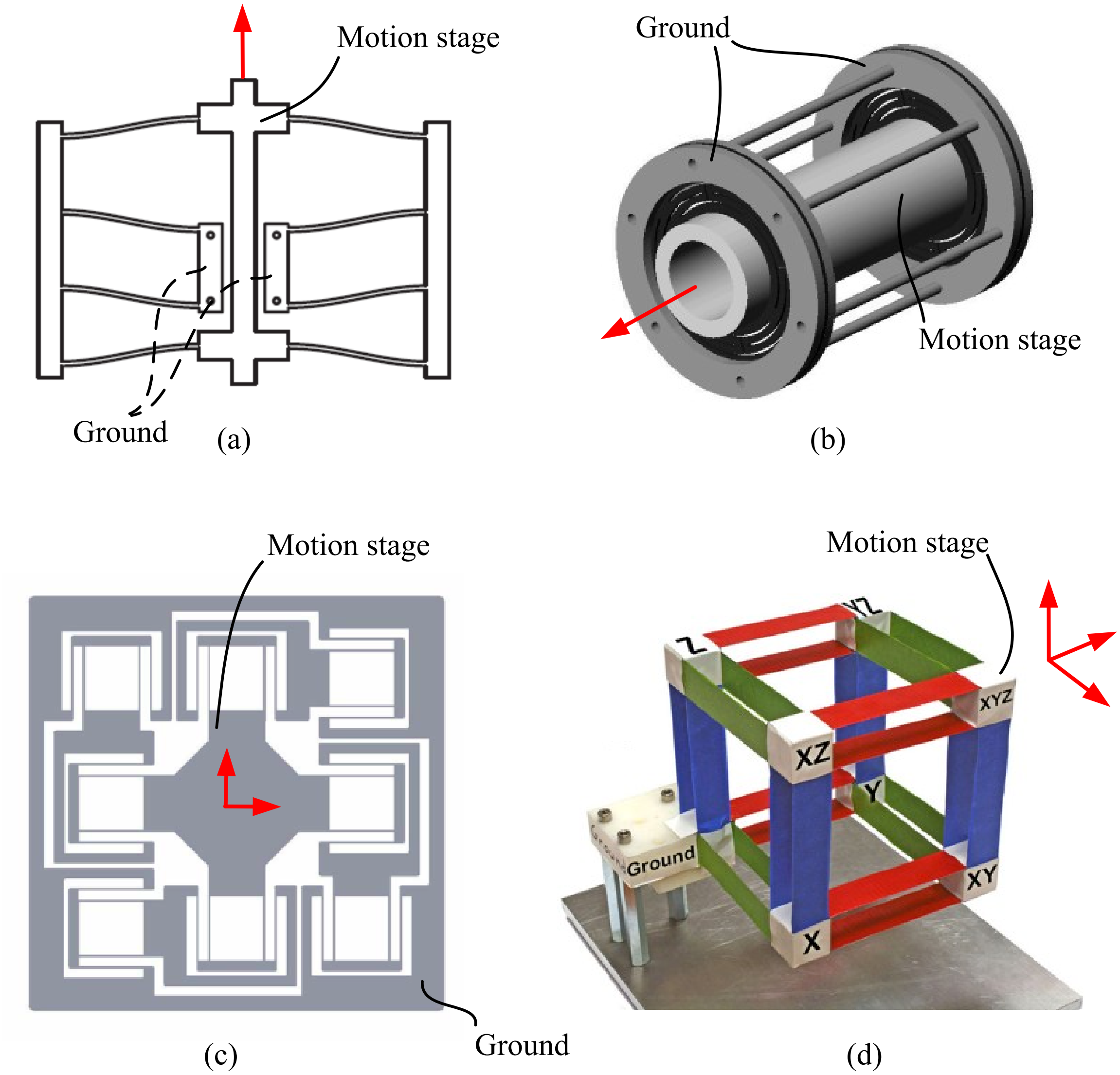

(a) (b) (c) (d)

Fig. 1.8: Examples of translational flexure mechanisms with large range of motion. (a) 1-DoF symmetric double parallelogram flexure bearing in a deformed configuration (also known as folded beam suspension) [60]. (b) 1-DoF symmetric diaphragm flexure [59]. (c) 2-DoF parallel-kinematic flexure mechanism comprised of double parallelogram flexure modules as a building block [57]. (d) 3-DoF parallel-kinematic flexure mechanism comprised of parallelogram flexure modules as a building block [58].

compared to the coarse-fine motion systems mentioned before, large-range nanopositioning systems comprising of flexure bearing involve equally challenging control problems, flexure-based motion systems are still preferable due to their low-cost and compact-size.

In addition to nanometric motion quality and large range, high scanning speed is also desirable to maximize process throughput. Furthermore, minimizing and expediently removing any heat generated from the motion system is also important because of the highly sensitive nature of these applications [33, 61].

1.6 Organization of the Thesis

In **Chapter I**, a typical nanopositioning system is described and some of its applications are mentioned. This is followed by a discussion on the limitations on currently available nanopositioning systems. A list of applications for large range nanopositioning systems is provided as a motivation to this work. Recent and ongoing research in the area of large range nanopositioning are described in the prior art. Finally, a summary of the chapters is provided, followed by suggestions for future work.

One of the major pending challenges in achieving large range high speed nanopositioning is that of actuation technology, which constitutes the focus of **Chapter II**. Several existing actuator options along with their limitations are discussed. The potential of moving magnet actuators (MMA) is highlighted in comparison to other actuators. Inherent tradeoffs in the specifications of an MMA and their impact on the performance of flexure-based nanopositioning systems are qualitatively discussed. A systematic model for the MMA is used to derive a figure of merit that captures the dynamic performance of the actuator. Next, performance tradeoffs at the motion system level are quantitatively identified in terms of the individual specifications of the actuator, actuator driver, flexure bearing, and thermal management system.

This understanding is employed in the optimal design and fabrication of a single-axis nanopositioning system comprising the aforementioned four components. Finally, preliminary testing results for the individual components, as well as the overall nanopositioning system, are reported.

In **Chapter III**, dynamic tracking performance in large range nanopositioning systems reported in the literature are compared. A classical feedback controller is implemented, and shown to achieve nanometric steady-state precision and resolution in point-to-point positioning experiments over the entire motion range in the single-axis nanopositioning system mentioned above. However, nonlinearities associated with the actuator as well as the driver result in inadequate tracking performance in response to dynamic commands. It is shown that a linear feedback and feedforward controller by itself offers inadequate performance. This is because of the limited sensitivity reduction that is possible by employing a feedback loop, given actuator saturation and low open-loop bandwidth of the system. For scanning-type applications, in which the command is a periodic signal, the deterministic part of the error arising due to nonlinearities also repeats every period. This provides the motivation to employ iterative learning control (ILC) to reduce the repeating portion of the tracking error. A brief introduction to ILC is presented followed by the design and implementation of a lead type ILC in conjunction with the existing feedback and feedforward controller. Experimental results are reported which demonstrate more than two orders of magnitude reduction in the tracking error while following dynamic commands, when compared to the performance obtained with a linear feedback and feedforward controller alone.

Chapter IV deals with the dynamic modeling of an XY flexure mechanism, comprised of double parallelogram flexure modules. A brief overview of different approaches undertaken to model the dynamics of flexure mechanisms are described first. Next, a lumped parameter model for a parallelogram flexure module, incorporating the nonlinear kinematic coupling that exists between its transverse and axial directions due to large deformations of its constituent beams, is presented. This is then extended to model the dynamics of two simpler, representative mechanisms. The nonlinear equations of motion are linearized about varying operating points and the effect of small structural asymmetry on the dynamics to produce nonminimum phase (NMP) zeros is studied. Finally, modeling and analysis of the entire XY flexure mechanism is presented. It is proposed that intentional asymmetry in the structural design can be employed to overcome the problem of NMP zeros.

A brief discussion about the control system design challenges and trade-offs for XY nanopositioning system is presented first in **Chapter V**. This is followed by design and implementation of independent and identical classical controllers along each axis and corresponding positioning performance. Similar to the approach adopted for the single-axis system, it is shown that implementation of independent iterative leaning controllers in conjunction with feedback along each axes reduces the tracking error in the XY plane by more than two orders of magnitude.

The following list highlights the specific contributions of this thesis:

1. Quantitative design trade-offs and performance limitations of moving magnet actuators as well as of the flexure-based motion systems employing these actuators.

2. Application of iterative learning control to overcome nonlinearities in the physical system, as well as limitations of linear feedback control, to achieve nanometric tracking performance for dynamic commands.

3. Modeling of the XY flexure mechanism to show that coupling between closely spaced resonances may conspire to produce complex-conjugate nonminimum phase zeros in mechanical structures.

4. Experimentally demonstrated nanometric tracking performance over several mil-

limeters of motion range for both single-axis and XY nanopositioning systems.

1.7 Future Work

In this thesis, some of the important challenges in simultaneously achieving large range and high motion quality in flexure-based nanopositioning systems have been highlighted and addressed. With the benefit of hindsight, some suggestions for further improving the positioning performance of the system, as well as a few interesting topics for future research are listed here:

1. Currently, a major limitation in the overall positioning performance comes from the existing hardware. In this regard, first, a better sensor in terms of speed and resolution as well as data acquisition hardware with higher speed and bit-size would greatly improve the achievable closed-loop resolution. Second, all the experiments were performed on a isolation table in a less-than-ideal laboratory environment. A real application would require the setup to be operated in a space with a stringent vibration isolation criterion such as VC–E or NIST–A [62]. Third, although a linear current driver is used to power the actuator, the power supply for the current driver is still a switching-type. Instead, a low-noise linear power supply is recommended. Also, the servoamplifier could not be operated over the desired power range due to the problem of excessive temperature rise with increasing power. A fan-based thermal management system should be employed with the servoamplifier to minimize its temperature rise.

2. For the XY nanopositioning system, the use of “XY Flexure Mechanism Design 1”, proposed in [63], should be explored. This design, due to its asymmetry, is not prone to suffer from low frequency non-minimum phase zeros. Secondly, the stiffness and hence the power requirement for this design will reduce by a factor of 2, compared to its symmetrical extension used in this thesis, without sacrificing

the open-loop bandwidth along both the axes. However, some of the disadvantages of this design include increased rotations of the rigid stages as well as unwanted out-of-plane vibration of the motion stage, over the desired range of motion [63].

3. Irrespective of the design of the flexure mechanism, any design would benefit from the incorporation of passive damping. It is shown in Section 4.6 that foam-based damping could be employed to overcome the problem of nonminimum phase zeros in flexure mechanisms. An additional advantage of damping the high-frequency resonances is the improvement in the closed-loop bandwidth and the low-frequency disturbance rejection. However, a systematic study, that will lead to a more deterministic approach to incorporate damping, is needed.

4. Further improvement in the controller design is suggested in Sections 3.6 and 5.5. With regards to the ILC, averaging of the ILC input and optimizing the ILC code to reduce the computation time should lead to further reduction in the tracking error and faster convergence, respectively. Also, MIMO feedback controller along with cross-coupled ILC should be investigated for their effectiveness in improving the tracking performance, while following more demanding command trajectories such as those having sharp turns.

5. The identification of a figure of merit for the moving magnet actuator raises some interesting questions. For example, what is the maximum theoretical value of the dynamic actuator constant that is achievable in these actuators across various architectures with and without manufacturing constraints? Novel MMA architectures, such as the one proposed in Section 2.5, should be further explored in this regard.

6. One of the interesting but unanswered aspects remains the physical explanation of complex-conjugate nonminimum phase zeros in mechanical structures. The symmetric double parallelogram flexure mechanism, described in Section 4.4.3, is

found to be one of the simplest structures exhibiting this phenomenon. A study of the energy transfer between modes at the nonminimum phase zero frequency in this mechanism could be a starting point.

CHAPTER II

Moving Magnet Actuation[1]

A moving magnet actuator (MMA) is a direct-drive, single-phase, linear electromagnetic actuator. The traditional MMA architecture is shown in Fig. 2.1, where an axially-oriented cylindrical permanent magnet sandwiched between two iron pole-pieces forms the mover. The stator consists of a back iron along with two oppositely wound coils connected in series. The permanent magnet field produces a Lorentz force on the static coils, proportional to the coil current, which in turn creates an equal and opposite reaction force on the mover. The fact that MMAs provide non-contact, frictionless, and cog-free actuation over several millimeters range of motion makes them useful in a wide range of precision motion applications [65], disk drives [66], and automotive valves [67]. The goal of this chapter is to systematically investigate the feasibility of MMAs in enabling large range ($\sim$ 10 mm) and high scanning speed ($>$ 10 Hz or 300 mm/s) in flexure-based nanopositioning systems.

2.1 Actuators Used in Nanopositioning

The performance of an actuator is usually specified via its motion range, resolution capability, output force, speed of response, size, power consumption, efficiency, etc.

---

[1] This work was done in collaboration with David Hiemstra in the Precision Systems Design Laboratory at the University of Michigan. A part of this work has been published in a journal paper in IEEE/ASME Transactions on Mechatronics [64].

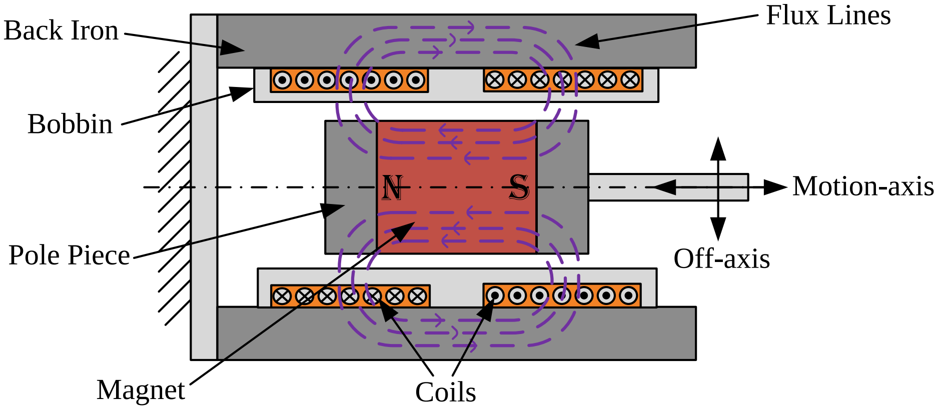

Fig. 2.1: Moving magnet actuator schematic

[9, 68]. In general, it is difficult to simultaneously achieve desirable values of all these specifications due to limitations and trade-offs arising from the construction and underlying physics of the actuator [69].

2.1.1 Piezoelectric Stack Actuators

Given their high resolution, force, operating bandwidth, and lack of friction and backlash, piezoelectric actuators based on Lead Zirconate Titanate (PZT) are the standard actuation method used in most existing nanopositioning systems. The primary limitation of these actuators is their inherently small stroke ($\sim$ 10–200 μm) [3]. In an attempt to overcome this, PZT actuators may be integrated with suitable flexure-based motion transmissions that amplify their range [70–72]. However, amplifying the motion by N times reduces the actuator's effective stiffness by N^2 times and force by N times, at the output of the transmission. This also leads to a smaller than expected stroke when the actuator and amplifier are integrated with a flexure bearing because of the blocking force that the latter generates. In many instances, the transmission may be cleverly designed such that it also serves as the flexure bearing and provides motion guidance for the motion system [71]. In these cases, the stroke of the motion system is indeed amplified to be N times that of the actuator, but the natural frequency of the motion system still scales inversely with N due to reduction in stiffness. Furthermore, to achieve high transmission ratios and yet maintain an overall compact motion system footprint, these designs exploit kinematic nonlinearities in the transmission mechanism. But this produces a transmission ratio that changes considerably, especially over a large motion range, as well as the possibility of over-constraint [72]. Moreover, the elastic deviation of a flexure-based transmission from true kinematic characteristics leads to *lost motion* between the actuator and motion stage [70].

2.1.2 Quasi-static and Ultrasonic Piezomotors

These motors employ a repetitive actuation pattern that converts the limited displacement of a piezo-ceramic element to theoretically infinite displacement. The actuation pattern relies on friction to produce relative motion between the piezo-ceramic element and the mover. Quasi-static piezomotors, which implement this repetition at frequencies lower than the resonant frequency of their piezo-ceramic elements, operate on either the *clamping principle* or the *inertial principle.* In the former case, motion is generated through a succession of quasi-static coordinated clamp/unclamp and extension/contraction *step cycles.* These so-called inchworm motors typically have a step size in the range of 10 nm to 1 μm and operating speed less than 10 mm/s [3, 9, 45]. In the inertial style quasi-static piezomotors, inertia and the difference in dynamic and static friction are exploited to produce discrete *slipping* steps, which may be repeated indefinitely [73]. While these quasi-static piezomotors provide good performance in large-range point-to-point positioning with nanometric precision, they are not suitable for high-speed scanning where precision has to be maintained along the entire motion profile. This is because of the impact-induced axial vibrations during steps, often termed as *glitch*, which is typically of the order of 50 nm [3]. These glitches become even more prominent at higher speeds.

Ultrasonic piezomotors excite resonant bending modes of a piezo-ceramic element in the ultrasonic frequency range which combine to produce a repeating elliptical stepping motion. These actuators provide higher speeds (100–500 mm/s) but much lower force capability (< 10 N) [9, 74]. Another potential drawback of ultrasonic actuators is heat generation [74]. Furthermore, a major drawback of all quasi-static and ultrasonic piezomotors, especially for large range nanopositioning, is their low fatigue life [3].

2.1.3 Linear Electromagnetic Actuators

Recognizing the limitations of piezoelectric actuators, several direct-drive, linear electromagnetic actuators have been designed and investigated for large-range, high-speed nanopositioning [8, 48, 75–79]. Although multi-phase electromagnetic linear motors provide non-contact operation over a large motion range (~ 100 mm), they sometimes suffer from cogging, thus limiting the achievable precision [61, 79]. While cogging may be eliminated via slot-less and iron-less constructions [80], the single-phase non-commuted voice coil actuator (VCA) and moving magnet actuator (MMA) offer unmatched simplicity in design and construction, along with non-contact and cog-free motion, low cost, and sufficiently large stroke [8, 76, 77].

A cross-section of a typical VCA configuration is shown in Fig. 2.2(a), where an axially-magnetized cylindrical permanent magnet and an integrated tubular back iron form the stator, and a coil wound on a bobbin forms the mover. The heavy permanent magnet and back iron are stationary, allowing the lightweight coil to achieve a fast mechanical response time [77, 78]. However, heat dissipation from the coil connected to the motion stage and non-deterministic disturbance due to the moving coil wires degrade the motion quality [81]. To overcome these problems, the voice coil is sometimes employed in an inverted configuration [8] (Fig. 2.2(b)). While this configuration eliminates disturbance from moving wires and improves thermal dissipation, it adds

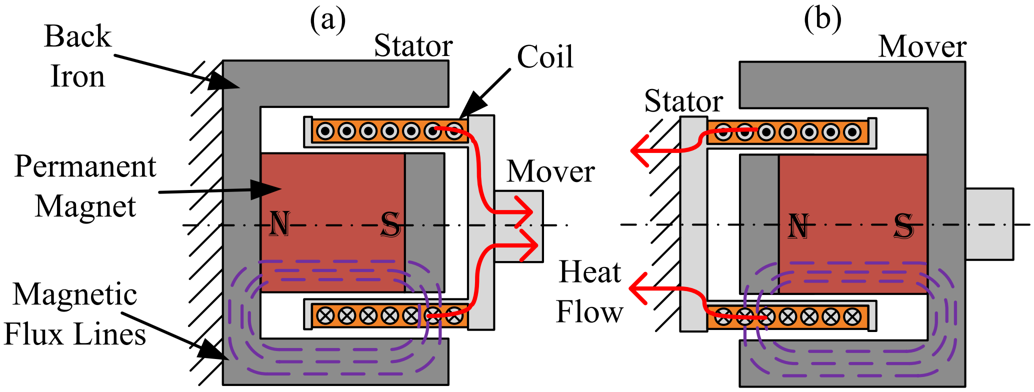

Fig. 2.2: Voice coil actuator schematic with (a) coil as mover and (b) magnet as mover

the large mass of the magnet and back iron to the motion stage. When employed with a flexure bearing, the resulting low natural frequency not only limits the open-loop and closed-loop bandwidth of the overall motion system but also compromises closed-loop disturbance rejection, which is necessary to achieve nanometric motion quality [82].

The MMA shown in Fig. 2.1 embodies all the benefits of the inverted voice coil and also has a significantly lower moving mass since the relatively heavy back-iron remains static along with the coil. Additionally, the non-deterministic disturbance due to the moving coil leads is eliminated. The static back iron also allows for improved heat dissipation and keeps the heat generated due to resistive losses in the coils further away from the motion stage. While these advantages make MMAs a promising candidate for actuation in nanopositioning, several design challenges and performance trade-offs remain, as discussed next. Also, while other variations exist [78, 83], the traditional MMA architecture of Fig. 2.1 is most commonly used because of its simple construction and practical viability, and is therefore the focus of this work.

2.2 MMA Performance Tradeoffs and Design Challenges

The requirements placed by the desired nanopositioning performance on the MMA specifications are qualitatively discussed below.

1. In the absence of friction and backlash, the motion quality of the nanopositioning system is determined by its closed-loop tracking performance, which is partly limited by noise and harmonic distortion in the electrical driver that supplies current to the actuator. Higher open-loop bandwidth helps attenuate the effect of this noise/distortion in closed-loop operation [82], enabling higher motion quality. The open-loop bandwidth, which correlates with the first natural frequency of the motion system, can be increased by increasing the flexure stiffness and decreasing the overall moving mass. The noise and distortion in the electrical driver can also be reduced at the source by lowering the actuator power input.

2. A large stroke and high flexure bearing stiffness demands a large actuation force. For high scanning speed and large stroke, the actuator also has to overcome inertial loads, which place further demands on the actuation force. For the scanning applications described earlier in Chapter I, external forces on the motion stage are negligible in comparison to the spring and inertial forces.

3. Non-uniformity in the MMA's force output over its stroke, for a fixed current input, also leads to non-linearities that produce higher order harmonics in open-loop as well as closed-loop operation [61]. While the adverse effect of these harmonics on the motion quality may be mitigated by a high closed-loop bandwidth, which ensures better disturbance rejection, the actuator can also be designed to provide greater force-stroke uniformity.

4. Temperature rise due to power dissipated as heat is detrimental to the components as well as to the assembly of the motion system. The feedback sensor can

lose accuracy and the mechanical assembly can develop undesired stresses and distortion. Minimizing these effects requires minimizing the power consumption of the actuator and effectively removing the generated heat from the system, even though the heat source in an MMA is located further away from the motion stage as compared to a VCA.

5. Separation of the back-iron from the permanent magnet in an MMA introduces the risk of snap-in instability in the direction perpendicular to the motion axis [84]. This instability gets worse with increasing actuator force, and can be mitigated by a flexure bearing that provides a much higher positive off-axis stiffness compared to the negative off-axis stiffness associated with the actuator.

This discussion reveals several conflicting requirements placed on the MMA specifications – force capability, force-stroke uniformity, moving mass, power consumed, heat generated etc. For example, the force output of an MMA can be raised by increasing either the moving magnet mass or the input power, but both are undesirable for reasons explained above. Reducing the flexure stiffness in the motion direction allows a larger portion of the actuation force to be devoted to inertial loads, leading to higher operating speeds; but lower stiffness also reduces the open-loop bandwidth and compromises disturbance rejection capability. While greater force-stroke uniformity reduces the reliance on large open-loop bandwidth to provide the desired motion quality, it typically requires an axially longer coil, which in turn implies greater power consumption and heat generation. Furthermore, any design features that increase the actuation force also increase the negative off-axis stiffness associated with the MMA. Clearly, these design challenges and performance trade-offs cut across the multiple components and physical domains of the overall motion system.

Although such trade-offs associated with MMAs have been previously identified, the discussion has been largely component-level and qualitative [78, 83, 85]. This work attempts to systematically capture these design limitations and performance trade-offs in a model-based quantitative manner, so as to identify the key bottlenecks to better system-level performance. For the MMA, it is important to identify good figures of merit that capture the above specifications and trade-offs quantitatively. Figures of merit help compare MMAs from different vendors, determine the suitability of an MMA for a given application, and set the objective in the conception and optimization of new MMA designs. It is also important to recognize if there exist fundamental limits on these figures of merit, arising from the inherent construction and underlying physics of the actuator. One such figure of merit that has been traditionally used is the *actuator constant*, which is defined as the actuator output force per unit square root of power consumed. It captures an important actuator-level trade-off, i.e., the output force of an MMA cannot be indefinitely increased without increasing the power input and heat generated. However, this actuator constant only captures the quasi-static performance of the MMA since it does not incorporate the actuator's moving mass. As a result, it does not reflect on the dynamic performance of the MMA when used in a flexure-based nanopositioning system. Other figures of merit for MMAs that do capture some degree of dynamic performance include the *electrical time constant* and the *mechanical time constant*. The electrical time constant (τ_e) is defined as the rise time of the current for a step voltage change and depends on the inductance to resistance ratio of the coil. While it does represent a trade-off between the current rise-time and heat generation, this trade-off is readily overcome via the use of a current driver. The mechanical time constant (τ_m) is defined as the rise-time of the velocity for a step voltage change and depends on the actuator constant as well as the moving mass. However, it does not reveal any inherent trade-off or design insights associated with the construction and physics of the MMA.

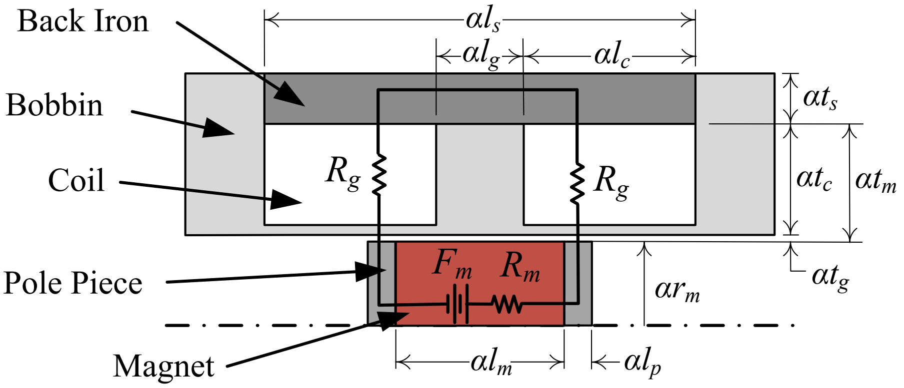

Fig. 2.3: MMA geometry and simplified lumped parameter model

2.2.1 MMA Figure of Merit to Capture Dynamic Performance

In order to capture dynamic performance, an MMA figure of merit is needed that not only includes the continuous output force and the power consumption, but also the actuator's moving mass. To quantitatively investigate the existence of such a figure of merit, the effect of geometric scaling on the actuator output force, power consumption, and moving mass is considered. Fig. 2.3 shows a lumped parameter model of an MMA with a traditional architecture. The dimensions l_m, l_p, r_m, and t_m denote the nominal magnet axial length, pole piece length, magnet radius, and magnetic air gap radial thickness, respectively. α is the geometric scaling factor. The following assumptions are made to simplify the analysis:

1. Any fringing and leakage flux is neglected.

2. The permeability of the back-iron and the pole pieces are much larger than that of a vacuum. Hence, the reluctance of the back iron and the pole pieces are neglected ($\mu_{iron} \gg \mu_0$).

3. The permeability of the magnet material, aluminum, and air is approximately equal to that of vacuum ($\mu_{air} \approx \mu_{Al} \approx \mu_{magnet} \approx \mu_0$).

4. All the radial space between the pole pieces and the back iron (t_m) is occupied

by coils. In other words, the mechanical air-gap (t_g) is negligible compared the thickness of coil (t_c).

Based on standard lumped parameter magnetostatic analysis [86], the magnetomotive force (F_m) and the lumped reluctances of the magnet and the air gap (R_m and R_g) are given by

$$F_m = \frac{\alpha B_r l_m}{\mu_m}; \quad R_m = \frac{l_m}{\pi \alpha \mu_m {r_m}^2}; \quad R_g = \frac{1}{2\pi\alpha\mu_0 l_p} \ln\left(1 + \frac{t_m}{r_m}\right) \tag{2.1}$$

where B_r denote the remanent flux density of the permanent magnet and μ_m and μ_0 are the permeability values for the permanent magnet material and vacuum, respectively. Next, the resultant flux (ϕ) and average magnetic flux density in the air gap (B_g) are then given by

$$\phi = \frac{F_m}{R_m + 2R_g}; \quad B_g = \frac{\phi}{2\pi\alpha^2 l_p (r_m + t_m/2)} \tag{2.2}$$

The force output (F), the power consumed, i.e., dissipated as heat (P), and the moving mass (m_a) can be determined to be

$$F = B_g i l_w = i\phi \frac{2\alpha t_m}{d^2} \tag{2.3}$$

$$P = i^2 R = i^2 \frac{\rho_c l_w}{A_w} = i^2 \rho_c \frac{16\alpha^3 l_p t_m (r_m + t_m/2)}{d^4} \tag{2.4}$$

$$m_a = \rho_m \pi \alpha^3 {r_m}^2 l_m \tag{2.5}$$

where i is the coil current, R is the coil resistance, ρ_c is the resistivity of the coil wire, d is the wire diameter, A_w is the cross-sectional area of the wire, l_w is the total length of the wire in the air gap, and ρ_m is the mass density of the magnet. It should be noted that the current (i), force (F), and power (P), are all dynamic variables. These three relations lead to

$$\frac{F}{\sqrt{P}\sqrt{m_a}} = \frac{B_r}{\frac{l_m l_p}{{r_m}^2} + \ln\left(1 + \frac{t_m}{r_m}\right)} \sqrt{\frac{\pi l_m l_p t_m}{4\rho_c \rho_m {r_m}^2 (r_m + t_m/2)}} \tag{2.6}$$

In the above relation, the scaling factor α, wire diameter d, and coil current i get canceled out, and the left-hand side term is only dependent on the physical constants and nominal dimensions, which are constant for a given MMA architecture. Thus, the force output (F) remains directly proportional to the square root of the actuator moving mass (m_a) and the square root of power consumed (P), irrespective of the scale of the actuator (α). Equation (2.6) may be restated as follows:

$$\frac{F}{\sqrt{P}\sqrt{m_a}} = \frac{K_t}{\sqrt{R}\sqrt{m_a}} \triangleq \beta \text{ (constant)} \tag{2.7}$$

where K_t is the force constant (force per unit current) of the MMA.

The constant β (units of $\sqrt{\text{Hz}}$), therefore, turns out be an important figure of merit in the design of an MMA, and is referred to, hereafter, as the *dynamic actuator constant.* While this constant is related to the previously known mechanical time constant ($\tau_m = 1/\beta^2$), it provides an important design insight that the latter does not. It reveals an inherent trade-off associated with the force, moving mass, and the power consumption of an MMA, which cannot be overcome by varying the actuator size. It should be noted, however, that β varies when the relative proportions between the actuator's dimensions are changed.

While several simplifying assumptions were made in the derivation of the MMA's dynamic actuator constant, Eq. (2.7) is found to be true even when these assumptions are removed in a finite element analysis (FEA) using Maxwell™. A snapshot of the analysis showing the flux path is shown in Fig. 2.4. The comparison of the closed-form model and the FEA is shown in Fig. 2.5. The ratio ($K_t/\sqrt{R}$), which is the actuator

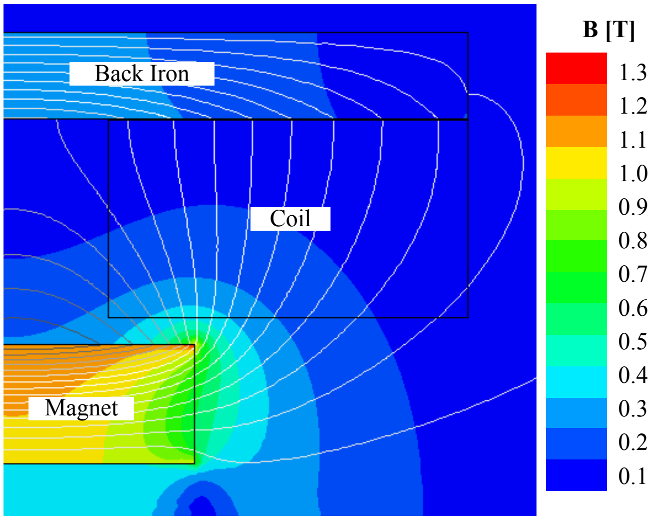

Fig. 2.4: Electromagnetic FEA using Maxwell™

constant, is plotted against the square root of the actuator moving mass ($\sqrt{m_a}$) for different values of the scaling factor (α). The slope of the curve represents the dynamic actuator constant (β=14 $\sqrt{\text{Hz}}$), for a particular choice of actuator dimension proportions.

In addition to the closed-form and finite element analysis, a survey of commercially available off-the-shelf MMAs [87–90] further validates the significance of Eq. (2.7). All

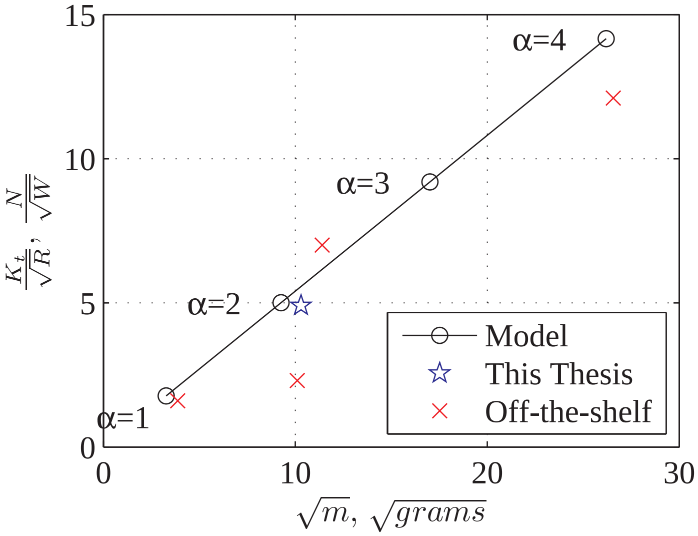

Fig. 2.5: Effect of geometric scaling on MMA performance

these MMAs are of the traditional architecture, offer a motion range of around 10 mm, and are of various sizes and proportions. However, as seen in Fig. 2.5, they all lie close to the straight line corresponding to β=14 $\sqrt{\text{Hz}}$. This suggests that the dynamic actuator constant, in addition to being independent of the actuator size, cannot be increased beyond a certain limit even by optimizing the dimensional proportions.

2.2.2 Impact of β on the Motion System Performance

When the MMA is employed in a flexure-based nanopositioning system, an important consequence of Eq. (2.7) is that it places a fundamental trade-off between the system's open-loop bandwidth (ω_n), desired scanning speed (ω), desired motion range ($\pm\Delta_0$), power consumed (P), and the moving masses (actuator: m_a, motion stage: m). Assuming a sinusoidal motion profile ($\Delta = \Delta_0 \cos \omega t$), this trade-off may be derived by equating the actuation force with the spring and inertial forces:

$$F = K_t i = (m + m_a)|{\omega_n}^2 - \omega^2|\Delta \tag{2.8}$$

where ${\omega_n}^2 = K_y/(m + m_a)$ and K_y is the flexure stiffness.

Equation (2.8) indicates that when the desired scanning speed is less than the natural frequency of the system ($\omega \ll \omega_n$), the required actuation force is dominated by the spring stiffness, and the actual scanning speed is less important. However, when the scanning speed is greater than the natural frequency ($\omega \gg \omega_n$), the required actuation force is dominated by inertial loads and depends on the square of the scanning speed. These two conditions represent the worst-case actuation force requirements. As expected, the actuation force becomes very small around resonance ($\omega \approx \omega_n$).

Substituting β from Eq. (2.7) and $P = i^2R$, Eq. (2.8) may be restated as:

$$\beta\frac{\sqrt{m_a}}{m+m_a} \geq \Delta|{\omega_n}^2 - \omega^2|\frac{1}{\sqrt{P}} \tag{2.9}$$

This expression quantitatively captures the performance trade-off that achieving large motion range, high resolution (enabled by good disturbance rejection due to high natural frequency), high scanning speed, and low power consumption (to minimize temperature rise and driver noise/distortion) are all at odds with respect to each other. The only way to simultaneously achieve these nanopositioning performance attributes is to use an MMA that provides a large β and minimize all moving masses in the system.

This represents a system level performance trade-off. If, for example, the flexure bearing is designed to be stiffer to increase the open-loop bandwidth and improve disturbance rejection of the driver noise/distortion and the actuator force-stroke non-uniformity, it would also require an increase in the actuation force in order to retain the same motion range. But, as per the MMA trade-off given by Eq. (2.7), this can only be achieved by increasing the magnet mass, for a given power consumption limit. Ultimately, using a stiffer bearing will not lead to the desired increase in the open-loop bandwidth. Trying to improve disturbance rejection via controller design hurts the closed-loop system stability robustness [82]. Therefore, it becomes important to employ an electrical driver with minimal noise and distortion, and design the MMA with maximal force-stroke uniformity. Furthermore, while increasing the current and therefore power into the system will improve its overall performance, it will also produce a temperature rise that is detrimental. Therefore, any increase in power has to be matched by a thermal management system that carries the heat out of the system to maintain its temperature.

2.3 Design and Fabrication of the Experimental Setup

In order to experimentally establish the validity of the dynamic actuator constant as an MMA figure of merit and to verify the performance limitations that it imposes on the overall motion system, a single-axis flexure-based nanopositioning system was designed, fabricated, and tested. This system comprises an MMA, an electrical driver, a symmetric double parallelogram flexure bearing, a novel thermal management system, a linear optical encoder, and feedback control hardware. The targeted positioning performance was set at: range ±5 mm, sinusoidal scanning speed 10 Hz, motion precision and resolution less than 5 nm, and temperature rise less than 0.5 °C. A high open-loop bandwidth was sought to reject disturbances and achieve the desired motion quality. At the same time, noise and harmonic distortion were minimized at the source in the electrical driver.

A custom-made driver was designed and tested to achieve high signal-to-noise-ratio (110 dB) and low total harmonic distortion (–90 dB). Details regarding the design of the driver and its characterization are provided in Appendix B. This driver was operated in the current mode with a gain of 1 A/V to provide direct control of the actuation force over a 1 kHz bandwidth. This driver is rated for 20 W power; higher power tends to further deteriorate the noise and harmonic distortion. Therefore 20 W was set as the upper limit of power input to the MMA. Since, in the worst case scenario of steady state operation, this input power is entirely converted to heat, the thermal management system was also designed to dissipate 20 W while maintaining the temperature of the motion stage within the targeted range.

2.3.1 Moving Magnet Actuator

The MMA dimensions and material were selected in a systematic manner to maximize β, while maintaining high force-stroke uniformity. In a minor deviation from the topology of Fig. 2.3, the designed MMA does not feature pole pieces. It can be separately shown that, although removing the pole pieces reduces the force constant (K_t), it leads to an overall higher value of β due to the reduced moving mass. All results presented in this section are based on FEA using Maxwell™.

1. The minimum magnet length (l_m) is governed by the stroke (Δ_0) and the coil separation (l_g), i.e.,

   $$l_m \geq 2\Delta_0 + l_g \tag{2.10}$$

   The coil separation (l_g) should be large enough so that the fringing flux from one face of the magnet does not pass through the opposite coil when the magnet is at the end of the stroke. Otherwise, this would lead to reduced force-stroke uniformity. For a desired stroke of ±5 mm and a chosen minimum coil separation of 10 mm, the magnet length was, therefore, selected to be 25.4 mm. The magnet dimension was also influenced by the standard available sizes.

2. While β is invariant with geometric scaling, it does vary with the dimensional proportions of the actuator. Therefore, once the magnet length is chosen, the magnet radius (r_m) and the coil thickness (t_c) can be selected to maximize β. Fig. 2.6 shows the effect of varying the magnet radius and coil thickness on β for a fixed coil length (l_c). Based on this plot, and taking manufacturing constraints and standard magnet sizes into account, r_m and t_c were chosen to be 12.7 mm and 15 mm, respectively. Assuming Neodymium-Iron-Boron (NdFeB) magnets, the actuator moving mass for these dimensions is 106 g. These selections lead to a β value of 14 $\sqrt{\text{Hz}}$ and an actuator constant of 4.5 $\text{N}/\sqrt{\text{W}}$, resulting in an achievable actuation force of 17 N for a power constraint of 20 W.

3. With the assumption that the flux path width is approximately equal to the radius of the magnet, the coil length (l_c) is dictated by the stroke and the magnet radius as

   $$l_c \geq 2\Delta + r_m \tag{2.11}$$

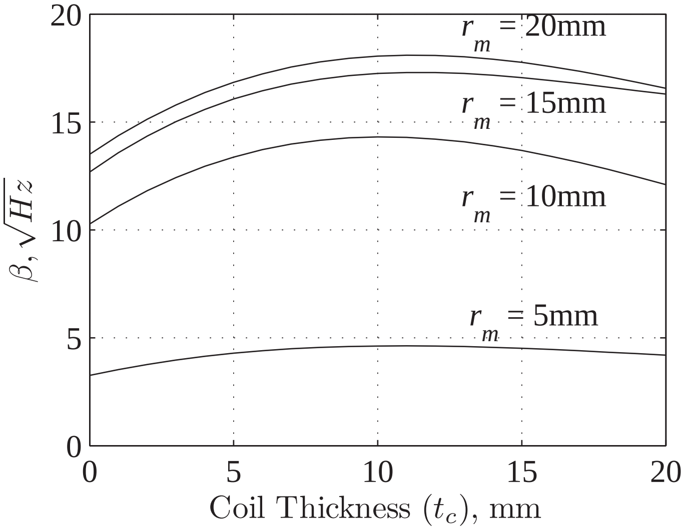

Fig. 2.6: Variation in the performance metric (β) with varying coil thickness and magnet radius

Increasing the length of the coil improves the force-stroke uniformity but only at the cost of an increase in the coil resistance, which reduces β. As shown in Fig. 2.7, the coil length was chosen to be 26 mm to limit the drop in force constant (K_t) at the ends of the stroke to be less than 10% without any appreciable loss in the dynamic actuator constant. The resultant force on the moving magnet is plotted against its axial position for 1 A coil current in Fig. 2.8 confirming this force-stroke non-uniformity.

4. As shown previously in Eq. (2.6), β is only dependent on the volume of the coil and is independent of the wire diameter (d). For example, although reducing d increases the coil resistance R, it also increases K_t due to greater number of turns, as per Eq. (2.4), thereby keeping β invariant. However, the choice of wire diameter presents a trade-off between voltage and current, for a fixed power level of 20 W, as shown in Fig. 2.9. Using this plot, 25 AWG wire with a diameter of 0.455 mm was chosen to keep the required voltage below 25 V, a limit imposed by the power supply used. This resulted in maximum continuous current of 0.56 A and coil resistance of 44.3 Ω.

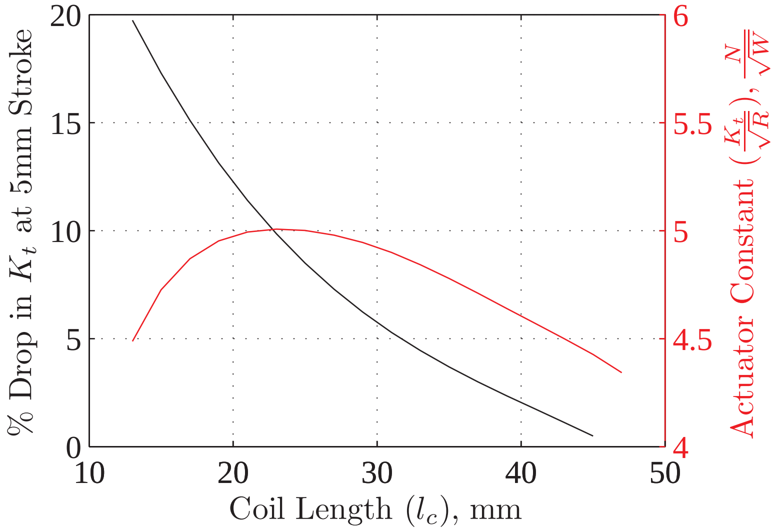

Fig. 2.7: Percentage drop in force constant at the ends of the stroke and actuator constant vs. coil length

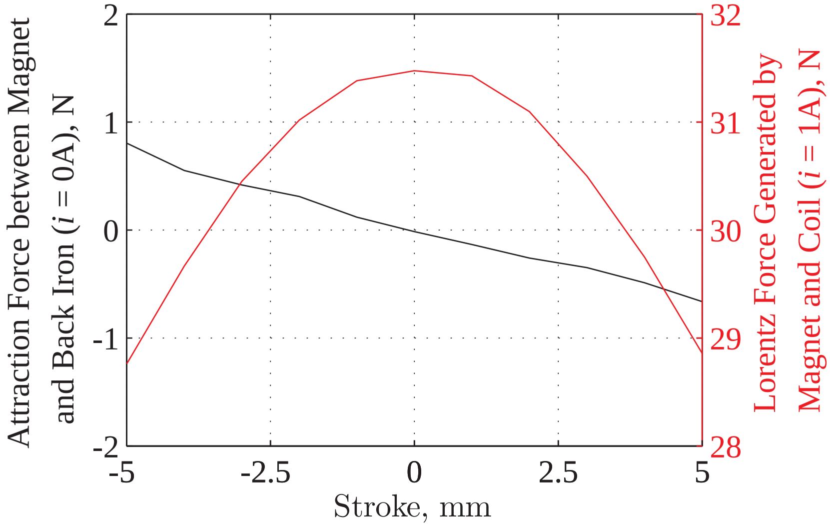

Fig. 2.8: Mover force vs. stroke for $i = 0$ A and $i = 1$ A coil current

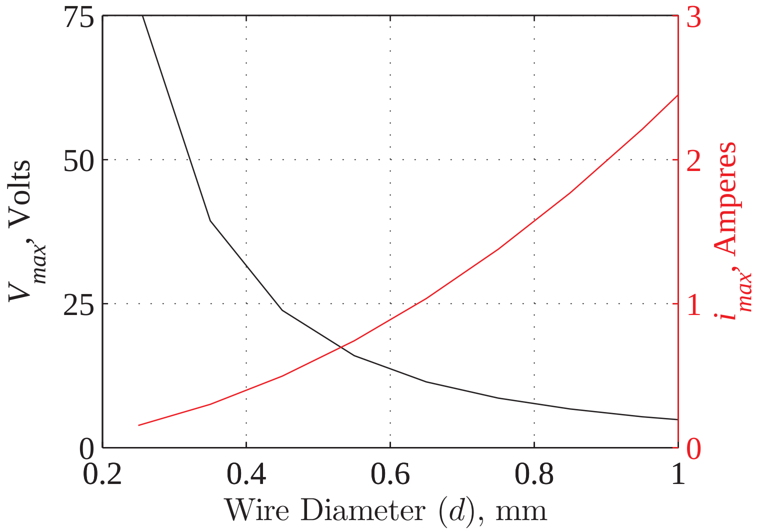

Fig. 2.9: Maximum continuous current and voltage requirement vs. wire diameter

5. The thickness of the back iron (t_s = 7.6 mm) is chosen such that the magnetic flux density in the iron remains below saturation for all values of coil current. Increasing the length of the back iron (l_s) reduces the axial magnetic force between the magnet and the back iron. This force, which acts in addition to the Lorentz force, tends to push the magnet towards the center of the stroke and is plotted explicitly in Fig. 2.8 for $i = 0$ A and $l_s = 65$ mm. It should be noted that while the Lorentz force component is symmetric with respect to zero stroke position, the overall force-stroke profile of the MMA turns out to be non-symmetric due to the force between the magnet and the back iron. This latter force component is unique to MMAs and does not exist in VCAs, in which the magnet and back-iron are rigidly attached.

Table 2.1 summarizes the MMA size and specifications. Based on this design, an MMA prototype was fabricated and assembled in-house, as shown in Fig. 2.10. The mover comprises a stack of four Grade 52 Neodymium-Iron-Boron (NdFeB) axial magnets (B_r = 1.45 T) mounted on a lightweight carbon fiber shaft and constrained using aluminum shaft collars. One drawback of this magnet is its low Curie tem-

Table 2.1: Key MMA dimensions

Parameter	**Value**	**Units**
Dynamic actuator constant	14	$\sqrt{\mathrm{Hz}}$
Stroke	10	mm
Moving mass	106	g
Actuator constant	4.5	$\mathrm{N}/\sqrt{\mathrm{W}}$
Force-stroke nonuniformity	9	%
Resistance	44.3	Ω
Inductance	133	mH
Radial/Axial size	36.8/85	mm
Air gap magnetic flux density	0.1–0.3	T

perature of 80 °C, but this risk is mitigated by the thermal management system described next. The coil bobbin was made of Aluminum 6061 because of its good machinability and high thermal conductivity. Also, it serves as a shorted turn which reduces the effective coil inductance [91]. However, one drawback of using aluminum as bobbin material is its susceptibility to eddy currents, because of its high electrical conductivity. These eddy currents give rise to phase lag [92], thereby degrading the dynamic performance of the feedback loop. The physical air gap between the mover

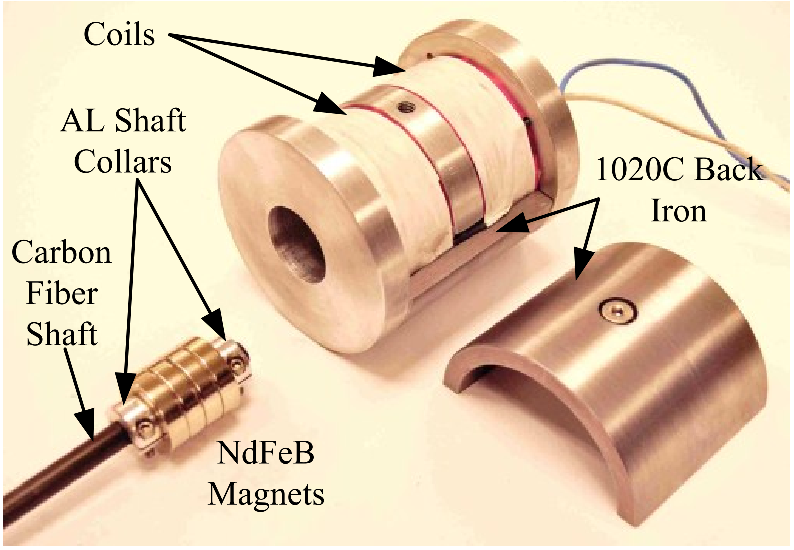

Fig. 2.10: MMA prototype

and bobbin was chosen to be 0.5 mm, primarily limited by manufacturing and assembly tolerances. The back iron was made from 1020C Steel with a saturation flux density of 1.6 T. In order to simplify the assembly process, the back iron was designed as two symmetric halves so that the magnet and the bobbin can be easily assembled *a priori* without the iron being in the vicinity of the strong magnetic force generated by the permanent magnet.

2.3.2 Thermal Management System

During steady-state operation, which represents the worst-case scenario of heat generation, most of the power sent to the actuator is converted to heat. As mentioned earlier, heat dissipated from the coils poses several potential problems. If 20 W heat is not drawn away from the actuator coils, FEA and experimental results show that the temperature rise at the motion stage is approximately 10 °C, and at the coil bobbin is more than 50 °C. Such a temperature rise, along with spatial thermal gradient, leads to significant internal stresses and distortion in the mechanical structure and assembly [61]. Furthermore, a temperature rise decreases the remanence of the permanent magnet, a process that is dramatically accelerated close to the magnet's Curie temperature [93]. This obviously reduces the actuation force. Also, a 10 °C rise causes the 10 mm long linear encoder scale to expand by 60 nm, as per encoder datasheet [94]. All these factors adversely affect the precision and accuracy of the nanopositioning system. Therefore, thermal management becomes a critical aspect of the overall system design.

Shown in Fig. 2.11, a novel passive thermal management system (TMS) was designed and integrated with the MMA [95]. While fan-based active heat dissipation systems can be designed to precisely control the temperature, they lead to air flow-induced vibrations that are detrimental to nanopositioning performance. Instead, a passive system was conceived that is based on latent heat transfer and therefore does

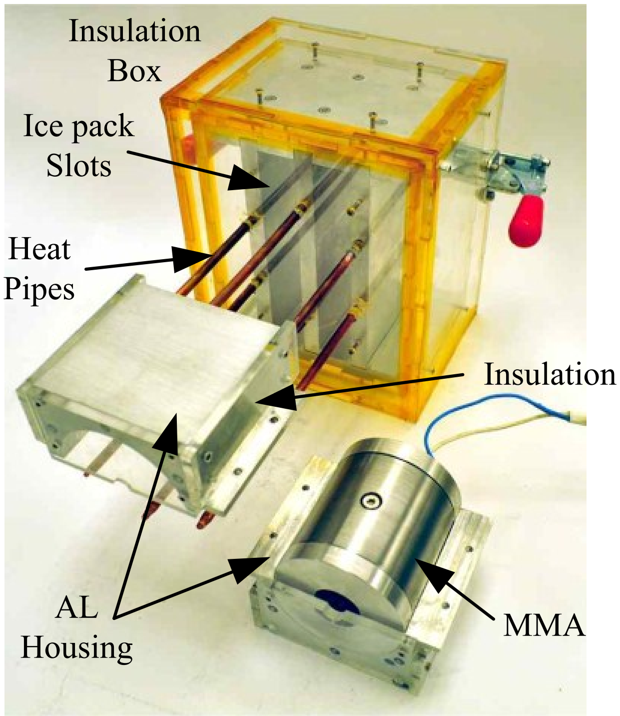

Fig. 2.11: Thermal management system prototype

not suffer from this disadvantage.

This TMS effectively transfers heat from the aluminum housing around the MMA coils to separately placed, water-sealed ice-packs using wick-type Copper heat pipes that serve as low thermal resistance paths. The heat generated at the coils is absorbed by ice as it converts to water, without any rise in its temperature. The aluminum housing and the racks containing ice-packs are thermally insulated via a double-layered acrylic box in order to minimize any thermal fluctuations of the surrounding environment. The critical components of the TMS (heat pipes, ice packs, and aluminum racks) were designed using a lumped-parameter thermal model in order to ensure that the steady-state coil bobbin temperature remains near room temperature for at least 4 hours of operation under constant 20 W power input to the actuator. Details of this model are provided in [95].

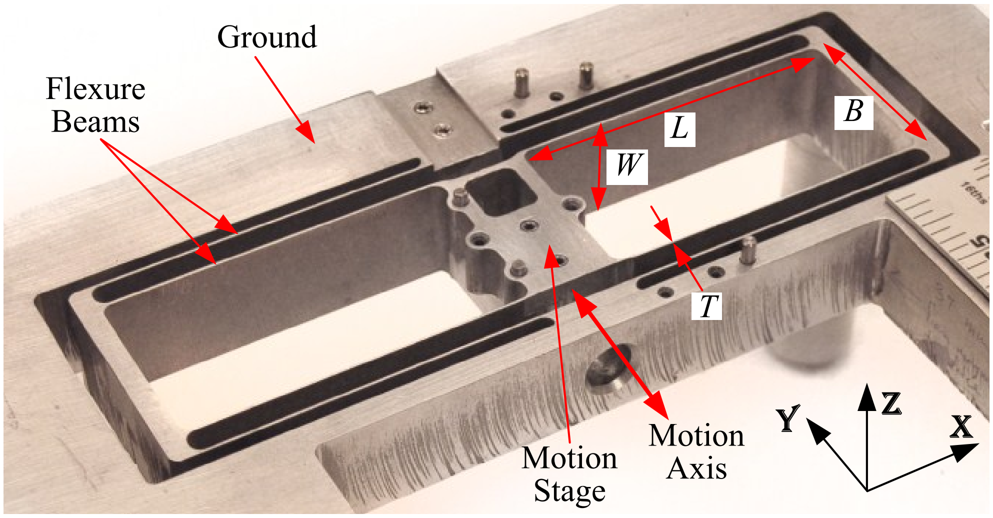

Fig. 2.12: Flexure bearing prototype

2.3.3 Flexure Bearing

A single-axis symmetric double-parallelogram flexure bearing was designed and fabricated (Fig. 2.12) to provide frictionless and backlash-free motion guidance over the entire range of motion. This design provides uniform motion direction stiffness over a relatively large stroke and high bearing stiffness in all other translation and rotation directions [96]. Aluminum 6061 was selected for the bearing material given its overall good flexure characteristics. As the first step, the size and mass of the motion stage were minimized ($m = 42$ g), while providing adequate space to interface the sensor and actuator. With the overall moving mass ($m + m_a$), dynamic actuator constant (β), power consumption limit (P), and desired stroke (Δ_0) and scanning speed (ω) all known, Eq. (2.9) predicts that the maximum achievable natural frequency (ω_n) is 27 Hz.

The beam thickness (T), width (W), length (L), and spacing (B) in the flexure bearing were set to be 0.75 mm, 25.4 mm, 80 mm, and 40 mm, respectively. The resulting geometry provides a motion direction stiffness of 3.43 N/mm, stroke of ±5 mm while maintaining a safety factor of 4 against yielding, and a natural frequency of 25 Hz.

The negative (destabilizing) stiffness of the off-axis force between the magnet and the back iron was calculated via electromagnetic FEA to be 1.3 N/mm at the nominal position. The stiffness values provided by the bearing in the X and Z directions are the lowest at the maximum motion stage displacement [96]. At the desired 5 mm displacement, these values are found to be 149.6 N/mm and 70.6 N/mm, respectively, thereby ensuring adequate off-axis stability of the magnet-back iron assembly.

2.3.4 Experimental Setup Assembly

In addition to the above subsystems, an off-the-shelf 5 nm, resolution linear optical encoder (RELM scale, Si-HN-4000 Read-head, and SiGNUM Interface from Renishaw) was used for position measurement of the motion stage. The assembly of the MMA, TMS, flexure bearing, and encoder is shown in Fig. 2.13. A removable back-plate simplifies the assembly of the MMA with the flexure bearing. Alignment between the MMA, back plate, and flexure bearing is achieved via dowel pins. As shown in Fig. 2.13 (inset), the motion stage was designed to hold the MMA mover shaft and optical encoder scale (A). The mover shaft is aligned and secured to the motion stage via a sleeve collar (B). Dowel pins (C) provide alignment of the encoder scale with respect to the motion stage. The optical encoder readhead (D) is mounted and aligned using three ground-mounted dowel pins (E). The final, fabricated single-axis nanopositioning system assembly is shown in Fig. 2.14.

2.4 Experimental Testing and Results

The performance of the MMA and TMS were measured first, followed by the characterization of the overall motion system.

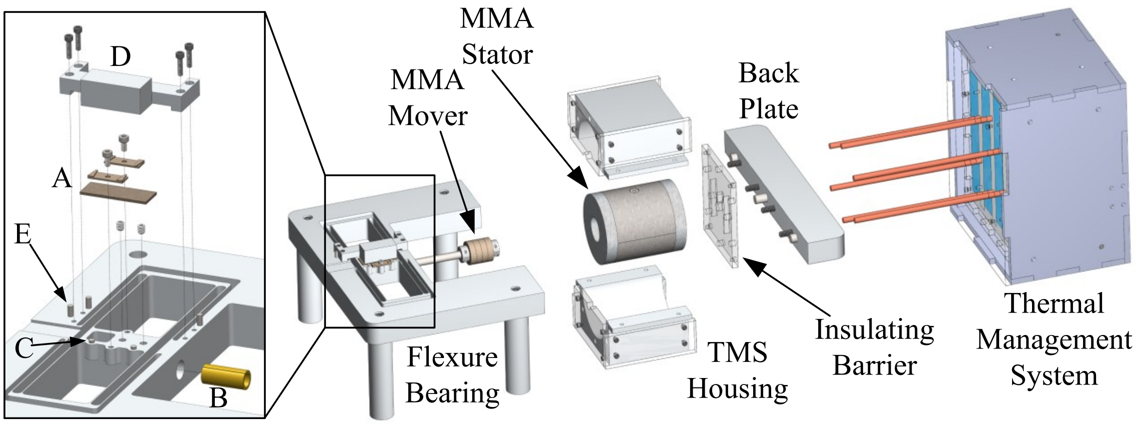

Fig. 2.13: Detailed CAD showing motion system assembly

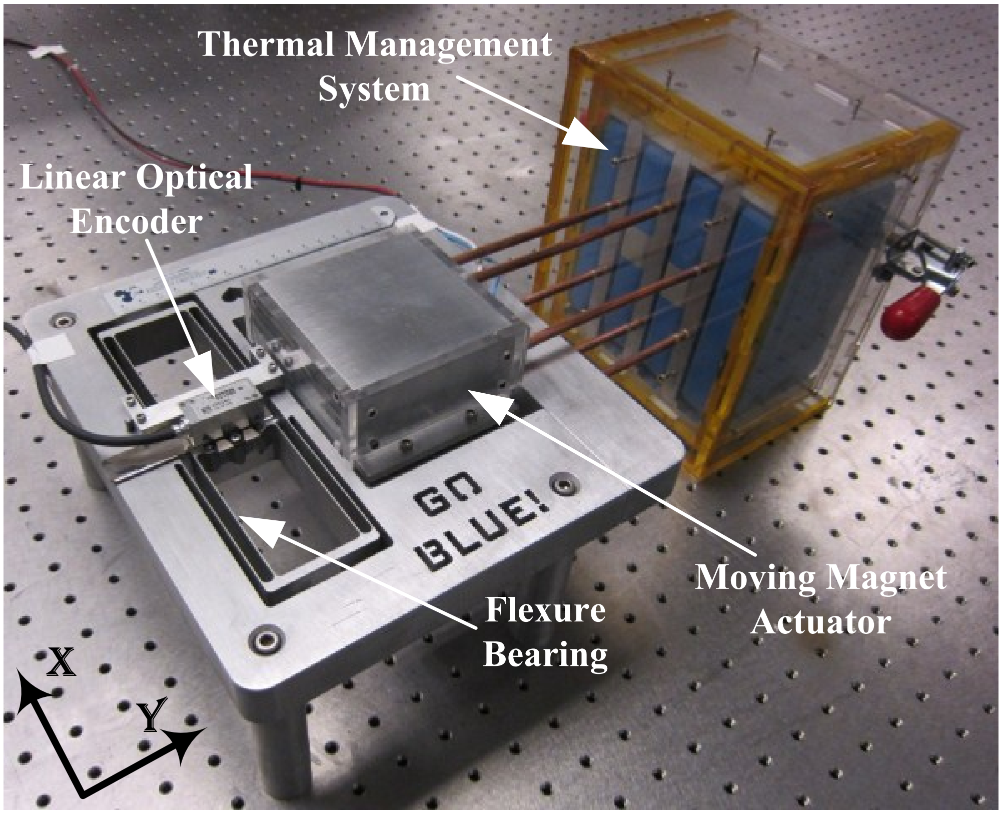

Fig. 2.14: Assembled single-axis nanopositioning system

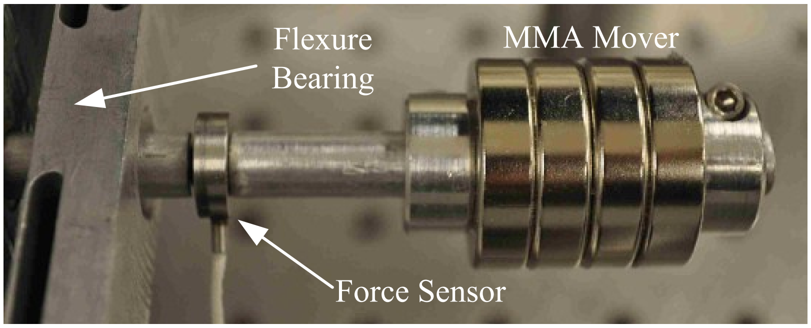

Fig. 2.15: Setup for MMA force measurement

2.4.1 Moving Magnet Actuator

The MMA force was measured using a load-cell (Model No. ELFF-T4E-20L from Measurement Specialties) in a temporary setup shown in Fig. 2.15. With the magnet held at the nominal position ($\Delta = 0$ mm), the MMA force is plotted with respect to the coil current in Fig. 2.16(a). The slope of this line provides the measured force constant K_t. This is within 3.5% of the value predicted by FEA; the difference is most likely due to a discrepancy between number of turns employed in the prototype coils and the FEA model. The measured Lorentz force-stroke non-uniformity, plotted in Fig. 2.16(b), is within 10% over the entire ± 5 mm stroke. The constant force offset in this plot is due to the abovementioned discrepancy in K_t.

The MMA coil resistance was measured to be 44.3 Ω. Assuming first order coil dynamics, the inductance of the coil was estimated by measuring the electrical time constant for a step change in applied voltage. From Fig. 2.17, the electrical time constant of the actuator is about 3 milliseconds, or 53 Hz. This corresponds to an inductance value of approximately 133 mH.

2.4.2 Thermal Management System

Fig. 2.18 shows the measured coil bobbin and motion stage temperatures for an MMA power input of 20 W, with and without the TMS. The motion stage, which is the most sensitive location in the motion system, remains within 0.5°C of room

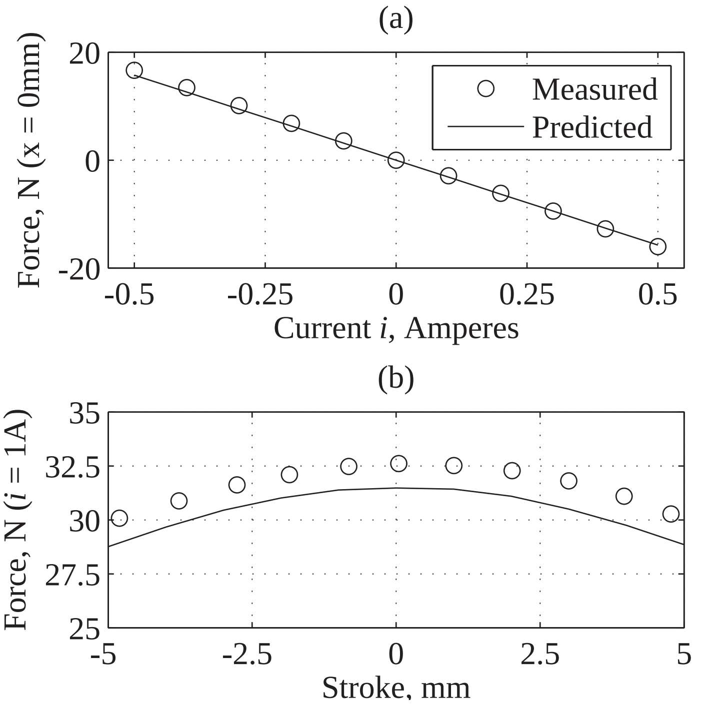

Fig. 2.16: MMA force measurement (a) Measured force constant (b) Measured force-stroke non-uniformity

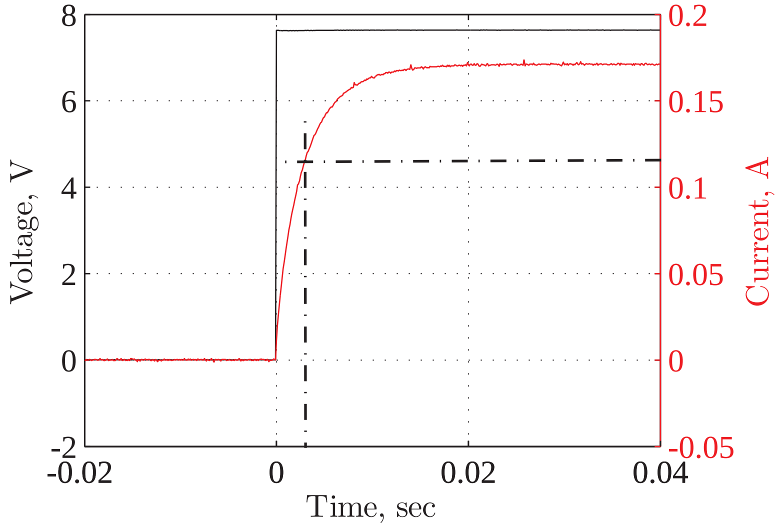

Fig. 2.17: Response of the MMA coil current to step voltage command

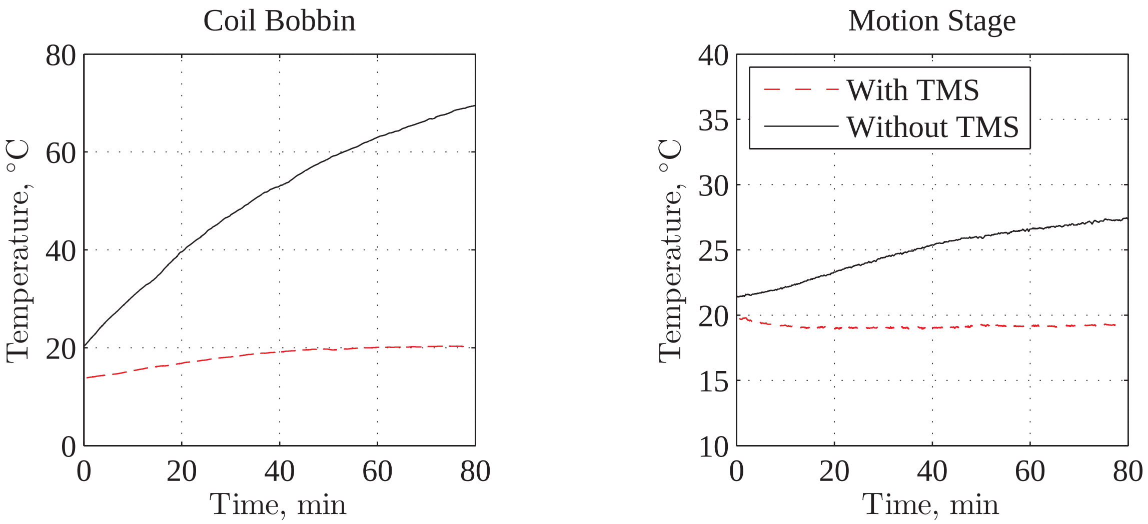

Fig. 2.18: Temperature rise of the coil bobbin and the motion stage with and without the thermal management system

temperature over the entire testing period, once steady-state is reached. This demonstrates the effectiveness of the proposed TMS in maintaining temperature stability.

2.4.3 Dynamic Response

Next, the open-loop frequency response of the overall nanopositioning system. Fig. 2.19 shows the resulting experimentally obtained transfer function between the command to the current driver (in volt) and the motion stage displacement (in µm). As expected, the first natural frequency of the system is found to be approximately 25 Hz. Damping seen at this resonance peak primarily comes from eddy currents in the aluminum bobbin.

A note on eddy current dynamics: Eddy currents are induced in the aluminum bobbin due to the changing magnetic field of the moving magnet. In order to experimentally study the possible effects of eddy currents on the dynamic performance of the actuator, an identical plastic (nylon) bobbin was manufactured. Fig. 2.20 shows the comparison of the open-loop frequency response of the motion system with aluminum

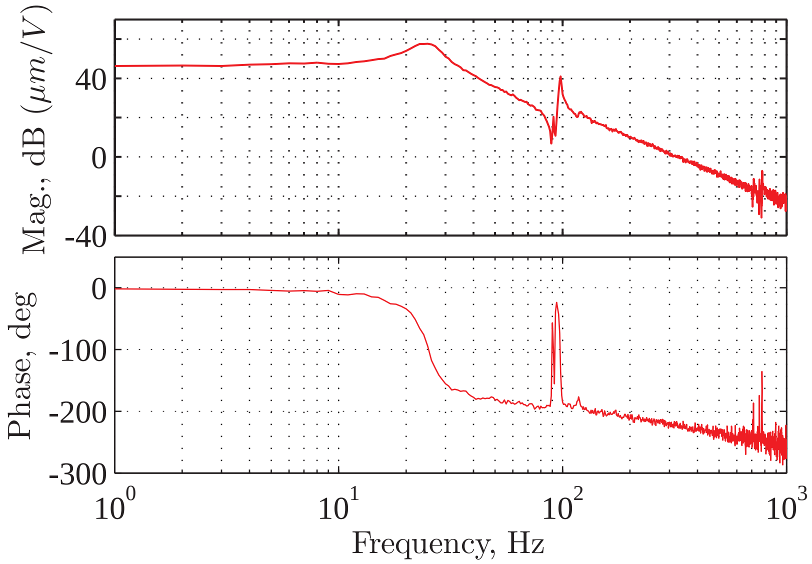

Fig. 2.19: Open-loop frequency response of the single-axis nanopositioning system

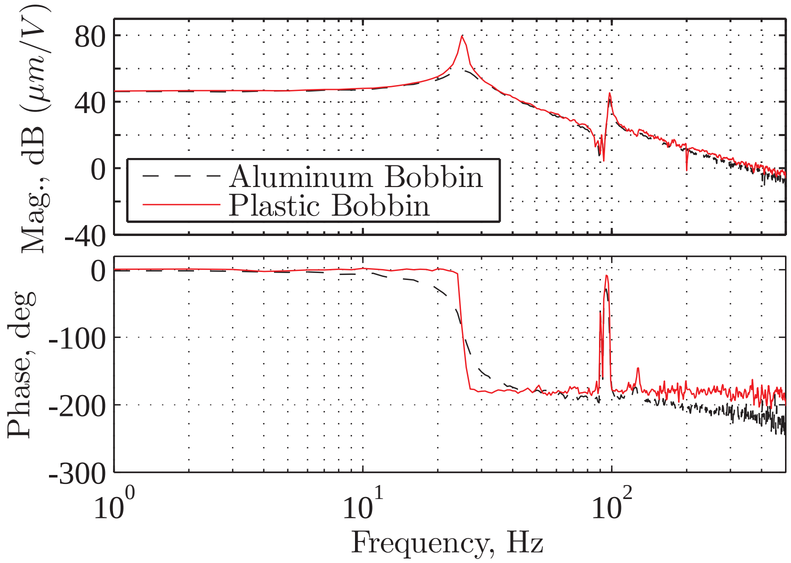

Fig. 2.20: Effect of bobbin material on system response

and plastic bobbin respectively. It can be seen that eddy currents in the aluminum bobbin leads to additional damping in the first resonance mode of the system as well as additional phase-lag at higher frequencies. The damping at the first resonance mode is inconsequential because the crossover frequency of the feedback loop lies much above the first resonance frequency. However, the additional phase-lag near crossover frequency (about 20° at 240 Hz) degrades the dynamic performance by reducing the phase margin in the closed-loop operation. On the other hand, the use of aluminum bobbin is beneficial from the point of view of heat dissipation, given its high thermal conductivity. Thermal management being a significant concern, aluminum bobbin was used finally. Alternately, a lamination of conductive but non-magnetic material, or a combination of plastic and aluminum, could be used for the coil bobbin to reduce the effect of eddy currents, while maintaining high thermal conductivity. A more detailed discussion about the effects of eddy currents on the electromagnetic actuator dynamics can be found in [92, 97].

2.5 Closure

In this chapter, the limits of motion performance allowed by MMAs in flexure-based nanopositioning systems have been established analytically and experimentally. It quantitatively elucidates the various design challenges and trade-offs that exist in simultaneously achieving range, speed, motion quality, and temperature stability. The key engineering specifications of the single-axis nanopositioning system are summarized in Table 2.2.

A figure of merit for the MMA, referred to as the dynamic actuator constant, is introduced. This figure of merit captures the inherent trade-offs between the actuator specifications, as well as the limitations on the performance of the nanopositioning system. It is important to note, however, that these trade-offs and performance limitations, associated with the dynamic actuator constant, holds only for moving

Table 2.2: Motion system specifications

Specification	Value	Units
Motion Range	10	mm
Open-loop natural frequency	25	Hz
Max. continuous power	20	W
Temperature stability	0.5	°C

magnet actuators and flexure-based motion systems employing these actuators.

Moving forward, this finding provides motivation to look into improved MMA architectures that offer greater values of the dynamic actuator constant while maintaining low force-stroke non-uniformity. One such proposed MMA architecture [98] is shown in Fig. 2.21, via a schematic cross-sectional view and a CAD rendition. From an electromagnetic standpoint, a major improvement in this design lies in the use of a radial permanent magnet (3) as opposed to the axial permanent magnet used in conventional MMAs. This not only reduces the moving mass considerably but the magnetic flux is also naturally aligned perpendicular to the coils (4). This in turn

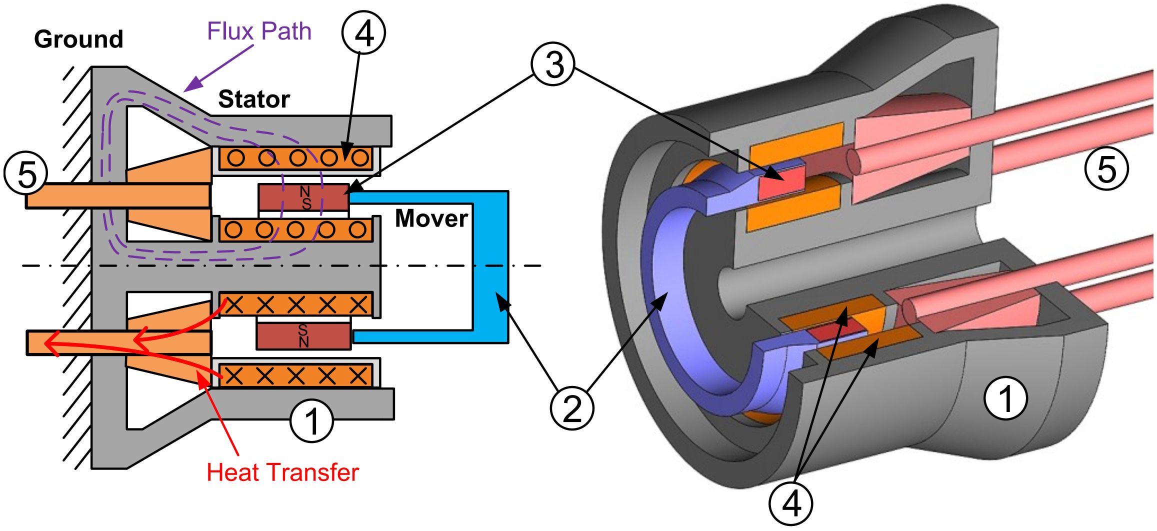

Fig. 2.21: Proposed MMA architecture [98]: 1. Back iron (stator) 2. Mover 3. Radial permanent magnet 4. Coils 5. Heat pipes to cooling system

decreases the fringing of the flux in the air-gap, thereby increasing the magnetic flux density between the moving permanent magnet and the static back-iron (1). In addition to these advantages, a low reluctance flux-return path through the back iron reduces the overall circuit reluctance, which further increases the flux density in the air-gap. These design modifications leads to an appreciable improvement in the continuous force output of the MMA. Initial FEA confirms that the reduction in the moving mass along with an increase in the force output increases the performance metric, β, by a factor of 2. This should provide greater open-loop bandwidth for better disturbance rejection as well as higher operating speeds for the overall positioning system.

CHAPTER III

Control System Design for Single-axis Nanopositioning System[1]

In Chapter II, the design, fabrication, and testing of a single-axis nanopositioning system employing a flexure bearing and moving magnet actuator was presented. In this chapter, design and implementation of a classical feedback controller along with an iterative learning controller is presented to overcome these nonlinearities in order to achieve nanometric tracking performance for dynamic commands over a large motion range. First, a brief comparison of single-axis large range nanopositioning systems in literature, in terms of their dynamic positioning performance, is presented. Next, it is shown that a linear feedback and feedforward controller by itself offers inadequate performance. This is because of the limited sensitivity reduction that is possible by employing a feedback loop, given actuator saturation and low open-loop bandwidth of the system. For scanning-type applications, in which the command is a periodic signal, the deterministic part of the error arising due to nonlinearities also repeats every period. This provides the motivation to employ iterative learning control (ILC) to reduce the repeating portion of the tracking error. Since its inception in early eighties, ILC has seen tremendous applications in the fields of robotics [100] and motion systems [101, 102]. Some of the advantages of ILC include its linear for-

---

[1] A part of this work has been published in a journal paper in Precision Engineering [99].

mulation, minimal knowledge of plant dynamics, simple design and implementation, and the fact that it can be applied to any existing feedback control system [100]. A brief introduction to ILC is then presented followed by the design and implementation of a phase-lead type ILC in conjunction with the existing feedback and feedforward controller. Experimental results demonstrate more than two orders of magnitude reduction in the tracking error while following dynamic commands, when compared to the performance obtained with a linear feedback and feedforward controller only.

3.1 Prior Art

The motion quality of nanopositioning systems is dictated by the tracking error, which is the difference between the commanded and the measured position. Tracking error may be evaluated for either point-to-point positioning commands or for path-following commands. Point-to-point positioning is concerned with moving the motion stage from one point to another and staying there for some finite period of time. Only the final position is relevant and the path taken to reach that position is not. Even after the commanded point is reached, the position output would still exhibit some random variation with time. This variation is referred to as the positioning noise, and is a measure of the motion system's resolution. While precision and accuracy of the nanopositioning system can be estimated for point-to-point positioning, these should be ideally measured in a more general case of path-following, such as raster scanning. In such cases, the motion stage is moved along a pre-defined trajectory in time and space, and position at each point along this trajectory is important [2]. Tracking error in the path-following experiments directly contribute to the lack of accuracy. However, it should be noted that the overall accuracy and precision for the nanopositioning systems, presented in this thesis, are not measured explicitly.

Obtaining nanometric tracking performance for such dynamic commands is relatively challenging because a linear controller may not provide adequate command

Table 3.1: Comparison of dynamic tracking performance in large range nanopositioning systems

Reference	**Motion Range (mm)**	**Bearing**	**Actuator / Transmission**	**Reference Command**	**Tracking Error (nm)**
Buice et al. [38]	50	Linear guide (coarse), flexure (fine)	DC motor with leadscrew (coarse), PZT (fine)	2.5 mm sine @ 0.01 Hz	45
Choi et al. [39]	–	Linear guide (coarse), air bearing (fine)	linear motor (coarse), voice coil (fine)	20 mm/s constant velocity, 300 mm motion range	150
Michellod et al. [42]	70	Flexure (coarse and fine)	Stepper motor with leadscrew (coarse), PZT (fine)	10 µm, 200 Hz Kolmogorov signal	8 (RMS)
Fujita et al. [103]	200	Linear guide (coarse), flexure (fine)	DC motor with leadscrew (coarse), PZT (fine)	100 µm sine @ 0.2 Hz	200
Maeda et al. [36]	10	Air bearing	Voice coil	3 mm bandlimited triangular profile @ 5 Hz	5
Zschaeck et al. [40]	200	Linear guide	Linear motor	1 mm/s constant velocity, 10 mm motion range	15 (RMS)
Fukada et al. [8]	1	Flexure	Moving magnet actuator	0.125 mm/s constant velocity, 0.5 mm motion range	50
Kim et al. [47]	5	Electromagnetic	Electromagnetic	2.5 mm/s constant velocity, 5 mm motion range	25

following and disturbance rejection over a desired finite frequency range. While a number of authors [8, 36, 37, 41, 47–49, 51–53] have reported large range (> 1 mm) and high resolution (< 10 nm *Root Mean Square* or RMS) for point-to-point positioning commands, only a few have shown nanometric positioning performance for dynamic commands over a large motion range (see Table 3.1 for a comparison). It should be noted that due to differences in the range, frequency content, and type of command trajectory used, it is not possible to compare the tracking performances of these systems in a consistent manner. However, it can be observed that the nanometric tracking performance is reported either over a small motion range or for slower or quasi-static commands.

Although lithographic steppers and scanners used for semiconductor manufacturing and inspection do provide large range and nanometric motion quality at relatively higher speeds [56], these machines are not targeted towards niche low-cost desktop applications. Achieving such specifications in a cost-effective and desktop-size setup is still a challenging problem.

3.2 Experimental Setup

The single-axis nanopositioning system, shown in Fig. 2.14, consists of a symmetric double parallelogram flexure bearing and a moving magnet actuator (MMA). The detailed design and fabrication of the experimental setup can be found in Chapter II. A linear optical encoder with 5 nm quantization steps is used for position measurement and feedback. The encoder read-head is mounted on the local ground of the flexure bearing and the scale is mounted on the motion stage. Hence, the sensor output is the relative displacement of the motion stage with respect to the local flexure ground. A custom-made driver, operating in the voltage mode, with a gain of 5 V/V and a bandwidth of 10 kHz is used to drive the MMA. Details regarding the design of the driver and its characterization are provided in Appendix B. The control system is implemented on a real-time hardware (DS1103 from DSpace) equipped with 16-bit digital-to-analog converter. While the sampling frequency and the loop rate are fixed at 10 kHz, all the measurements shown in this chapter are taken at a bandwidth of 1 kHz.

3.2.1 System Identification

In order to design a linear feedback controller, a linearized frequency domain model of the system is needed. Although, as mentioned in the next section, there are known sources of nonlinearities in the system, they can be neglected for the purpose of obtaining a linearized plant model. The open-loop frequency response of the nanopositioning system was found experimentally via broadband FFT-based system identification technique. For this purpose, a chirp signal with a frequency content of 1–1000 Hz was sent as the input to the amplifier. The amplitude of the chirp signal was chosen to restrict the maximum displacement of the stage to be less than 10 μm. Next, the Matlab™ function *invfreqs* was used to fit a continuous-time stable transfer function, $P(s)$, to the open-loop frequency response, obtained using Fourier analysis of the collected input and output signals [104]. The resulting 5th order transfer function is given by

$$P(s) = \frac{1.28 \times 10^{10}(s^2 + 5.63s + 3.34 \times 10^5)}{(s + 333.1)(s^2 + 150.50s + 3.31 \times 10^4)(s^2 + 12.43s + 3.87 \times 10^5)} \tag{3.1}$$

Fig. 3.1 shows the experimentally obtained frequency response along with the frequency response of the estimated transfer function from the amplifier command to the measured position. The pole at 53 Hz corresponds to the electrical time constant of the actuator (44.3 Ω coil resistance and 133 mH coil inductance). The damping seen in the rigid body mode is contributed by the eddy currents in the MMA Aluminum coil bobbin as well as by the back-electromotive force dynamics. The open-loop

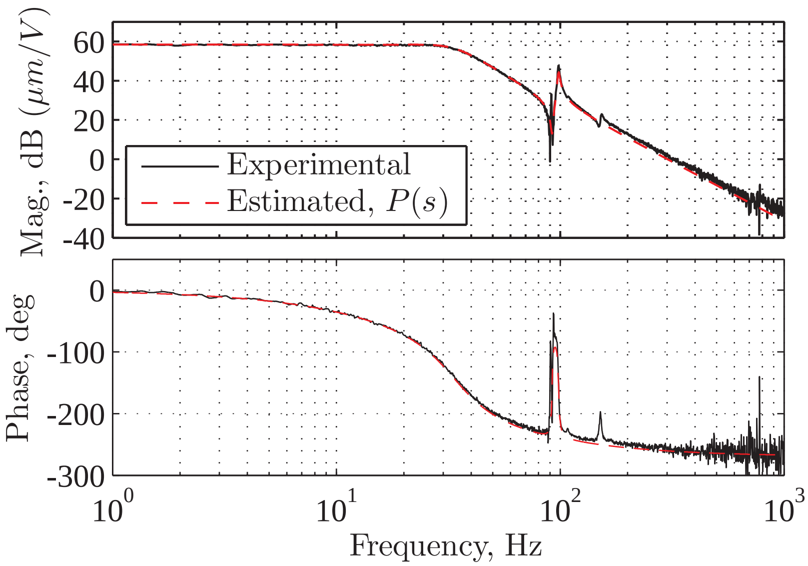

Fig. 3.1: Open-loop frequency response of the single-axis nanopositioning system

bandwidth, defined as the frequency where the plant gain drops down by –3 dB, is approximately 35 Hz. The low open-loop bandwidth of the motion system is a consequence of the fundamental limitations arising from the physical design of MMA in flexure based motion systems, mentioned earlier in Section 2.2.2.

3.2.2 Modal Analysis

Structural modal analysis was carried out to predict the natural frequencies and associated mode shapes of the overall mechanical structure, which includes the flexure bearing as well as the MMA magnet. As seen in Fig. 3.2, the first natural frequency around 25 Hz corresponds to the fundamental mode of vibration. At this mode, the motion stage as well as the secondary stages move in-phase with each other. The next two higher-order modes are related to the in-phase and out-of-phase vibration of the secondary stages. At these modes, the motion stage moves with a relatively small magnitude. The two zero-pole pairs at approximately 85-90 Hz are due to a combination of these two modes. The next higher-order mode, although not seen clearly in the frequency response, is an out-of-plane mode which occurs due to the

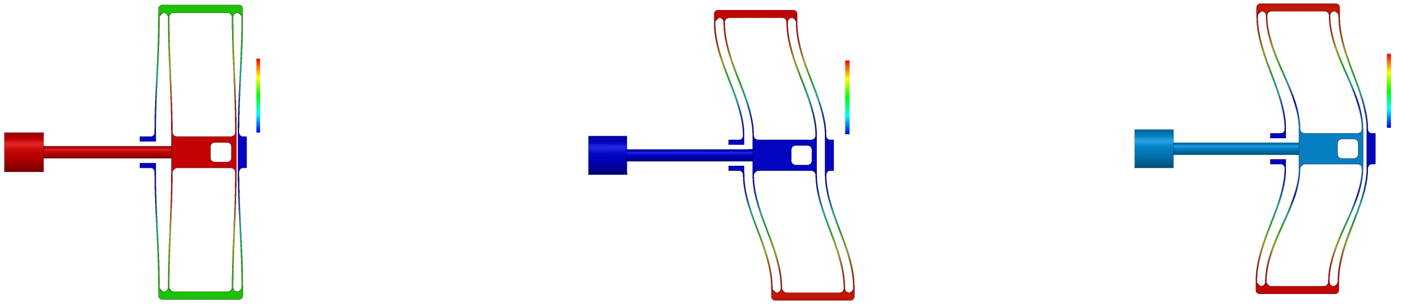

(a) 1st Mode: 22.4 Hz (FEA), 25 Hz (Experiment)

(b) 2nd Mode: 82.0 Hz (FEA), 91 Hz (Experiment)

(c) 3rd Mode, 86.3 Hz (FEA), 98 Hz (Experiment)

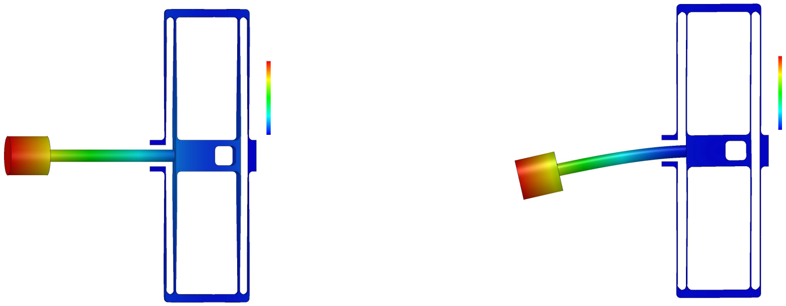

(d) 4th Mode, 109.4 Hz (FEA), 110 Hz (Experiment)

(e) 5th Mode, 152.8 Hz (FEA), 153 Hz (Experiment)

Fig. 3.2: Modal analysis of the single-axis nanopositioning system

twisting of the beams. The final mode shown is an out-of-plane mode due to the bending of the connecting rod. The pole-zero pair due around 150 Hz happens due to this mode. It is important to note that, because all these four closely spaced zero-pole pairs occur such that the poles are preceded by the associated zeros, there is no loss of phase in the open-loop system. At each zero, the phase starts to rise, and then, due to the pole, falls back to the nominal value. Thus, the controller design and closed-loop system performance are not affected much by the high frequency dynamics.

3.3 Linear Feedback Design and Limitations

Although the physical system described above is free of friction and backlash, the achievable positioning performance in the closed-loop setup, shown in Fig. 3.3, is still limited by the following factors:

1. Several sources of noise and disturbance that exist in the system limit the positioning resolution. This includes position sensor noise, actuator driver noise, electronic noise and quantization in the real-time control hardware, and mechanical floor vibrations.

2. As shown in Fig. 2.16(b), the force constant of the MMA is dependent on the position of the moving magnet with respect to the stator (coils and back-iron). This force-stroke non-uniformity degrades the tracking performance.

3. The non-linearity in the actuator driver also contributes to the tracking error. This nonlinearity shows up as harmonic distortion at multiples of the fundamental excitation frequency of the command signal. Fig. 3.4 shows one such measurement of the power spectral density (PSD) of the driver output, when the desired output is a 15 V, 2 Hz sinusoid. The signal-to-noise ratio, which is a measure of the broadband noise, is approximately 110 dB. However, the total harmonic distortion, defined as the ratio of power in the harmonics with respect to the power at the

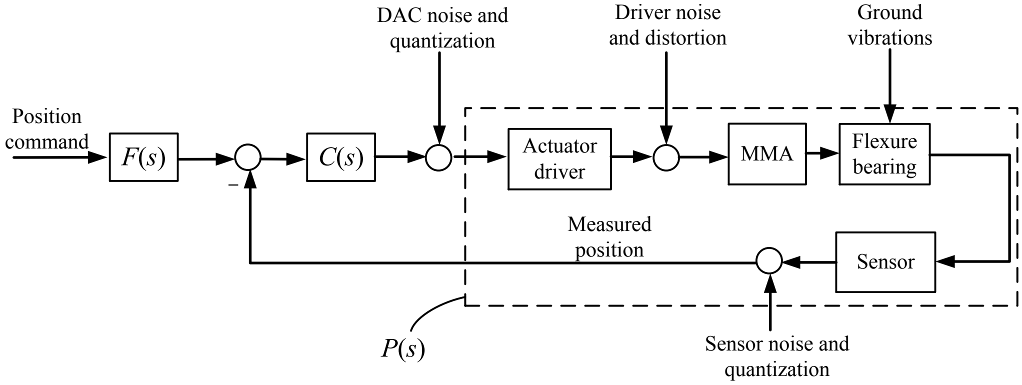

Fig. 3.3: Feedback architecture

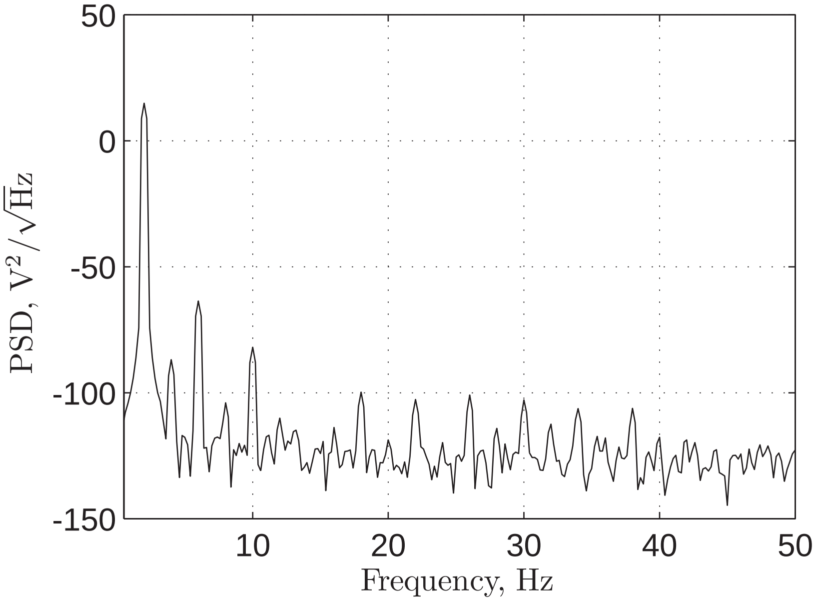

Fig. 3.4: Harmonic distortion in the actuator driver

fundamental signal frequency, is about –90 dB. Since this nonlinearity is less than 0.01%, it is generally very difficult to model it accurately or further reduce it via circuit design.

A linear feedback controller is first implemented to achieve good command tracking as well as noise and disturbance rejection to overcome the abovementioned sources of errors. The estimated open-loop transfer function, $P(s)$ in Eq. (3.1), is used to design an internal-model type linear feedback controller $C(s)$ using loop-shaping technique. The controller consists of zeros to cancel the coil dynamics as well as the first

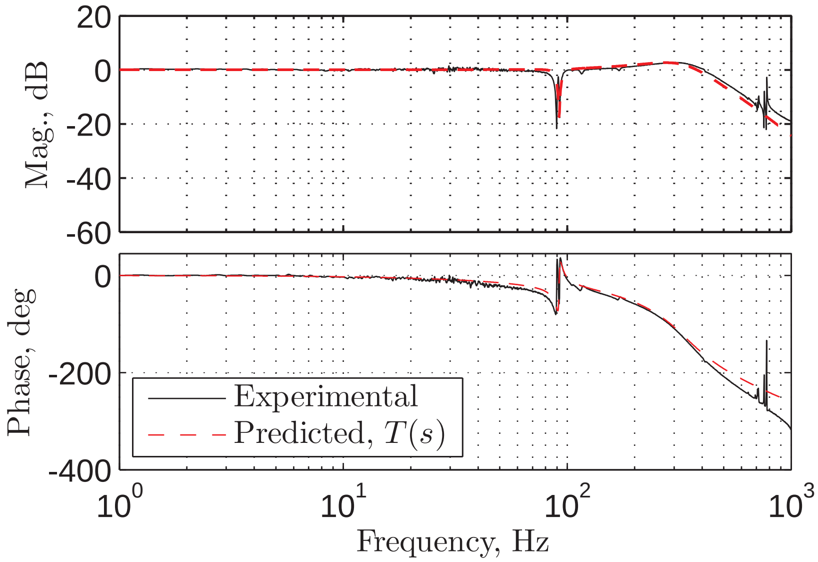

Fig. 3.5: Closed-loop frequency response

resonance poles of the flexure. An integrator is added to ensure zero steady-state error and low frequency disturbance rejection. This is followed by high frequency damped poles to make the controller structure strictly proper in order to attenuate sensor noise amplification. The following compensator was implemented:

$$C(s) = \frac{1.57 \times 10^4 (s + 141.5)(s^2 + 159.50s + 5.01 \times 10^4)}{s(s + 4000)(s^2 + 6700s + 1.92 \times 10^7)} \tag{3.2}$$

The resulting closed-loop transfer function is given by

$$T(s) = \frac{P(s)C(s)}{1 + P(s)C(s)} \tag{3.3}$$

The frequency response of the analytical closed-loop transfer function, $T(s)$, along with the experimentally obtained closed-loop frequency response is shown in Fig. 3.5. The phase margin and gain margin of the loop transfer function are 43° and 9 dB, respectively. The effective bandwidth of the feedback loop, defined as the frequency where the sensitivity transfer function first crosses –3 dB from below, is approximately 85 Hz. Because the controller is implemented digitally with a loop-rate of 10 kHz,

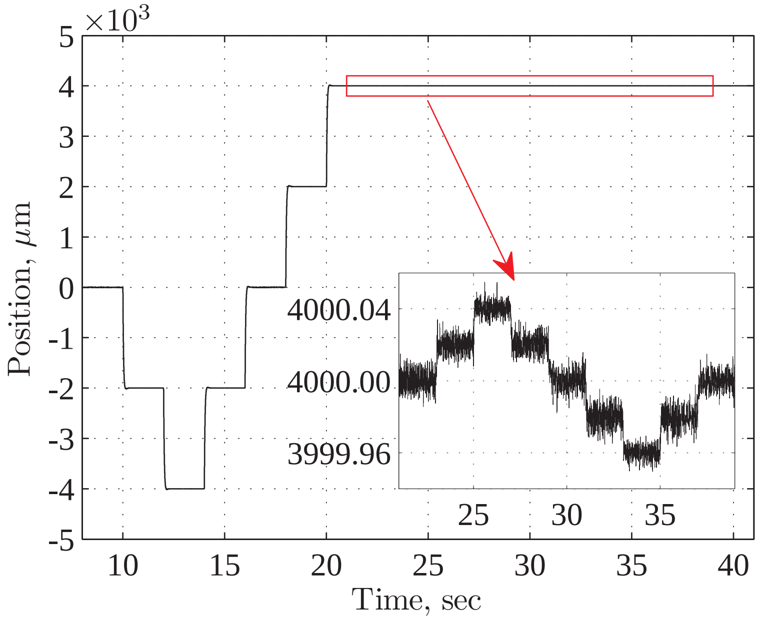

Fig. 3.6: Point-to-point positioning response

the phase loss due to sampling is estimated to be only 3° near the gain crossover frequency of around 240 Hz. For higher closed-loop bandwidth, it would be beneficial to design the feedback controller in the digital domain in order to account for the phase loss due to the finite loop-rate.

The nanopositioning system was tested for its point-to-point positioning performance with step commands of 2 mm and 20 nm, and the measured position response is shown in Fig. 3.6. The steady-state positioning error, which is a measure of the positioning resolution, is approximately 20–25 nm peak-to-peak or 4 nm RMS. Although the quantization step size of the linear optical encoder is 5 nm, the steady state peak-to-peak position variation of the encoder output is 20–25 nm. Thus, it can be seen that the closed-loop positioning noise is reduced to the sensor noise.

A note on the sensor noise: The quantization step of the position measurements obtained via the linear optical encoder is 5 nm. However, the position stability of the

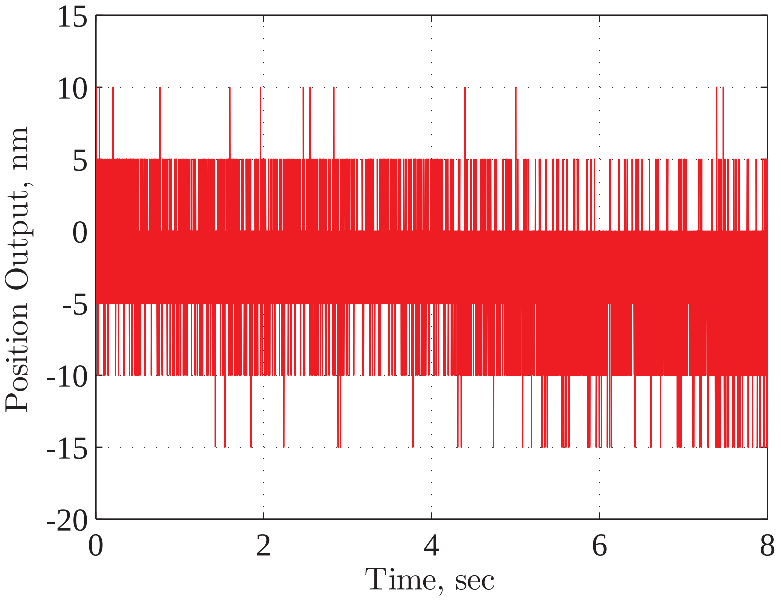

Fig. 3.7: Resolution of the linear optical encoder

encoder is 20–25 nm (peak-to-peak). This means that even if the motion stage (on which the encoder scale is mounted) is physically clamped to the ground (on which the encoder read-head is mounted), the position variation in the encoder output is of the order of 20–25 nm. One such measurement is shown in Fig. 3.7. This position variation is sometimes referred to as the *jitter* in the encoder and is mainly caused due to the electronic noise in the interpolation hardware. The RMS value of the position variation is 4 nm, which is referred to as the resolution of the sensor.

In order to evaluate the tracking performance with the linear feedback controller, a 4 mm (i.e., 8 mm peak-to-peak), 2 Hz sinusoidal signal is applied as the command. The resulting tracking error was observed to be within ±46μm, which is quite high for nanopositioning. A part of the tracking error comes from the phase error in the closed-loop transfer function at 2 Hz, which is approximately 0.6°. A lead-lag type feedforward compensator $F(s)$ is added to correct for the phase error in the frequency range below 10 Hz. $F(s)$ is given by:

$$F(s) = \frac{3.807s + 3350}{s + 3350} \tag{3.4}$$

Fig. 3.8(C) shows the power spectrum of the tracking error with 0 dB corresponding to 1 $\mu m^2/Hz$. It is evident that the tracking error consists of broadband noise along with a component at the command signal frequency, as well as its higher harmonics. While the component at 2 Hz can be attributed to inadequate command following, the higher-frequency harmonics are a consequence of the nonlinearities in the actuator and the driver, as mentioned earlier. With the addition of the feedforward compensator, the tracking error is reduced to ±2.5 μm (see Fig. 3.8(A)). This corresponds to a reduction of about 18 times compared to performance obtained with feedback alone. This improvement comes only due to reduction of the tracking error at 2 Hz (see Fig. 3.8(C)). The fact that the error component is not fully eliminated can be attributed to the uncertainty in the closed loop transfer function model used to design the feedforward compensator. The higher frequency harmonics which originate due to the nonlinearities remain unaffected.

The feedback part of the linear controller does provide some reduction in the harmonic content as compared to tracking in an open-loop setting (see Fig. 3.8(D)). This reduction in the magnitude of the harmonics is a result of sensitivity reduction achieved due to feedback, and can be predicted by plotting the sensitivity transfer function, $S(s)$, which is given by

$$S(s) = \frac{1}{1 + P(s)C(s)} \tag{3.5}$$

Fig. 3.8(B) shows the Bode magnitude plot of the sensitivity transfer function of the feedback loop. The harmonic component at 10 Hz, for example, is suppressed by 25 dB in closed-loop, corresponding to the –25 dB magnitude of the sensitivity trans-

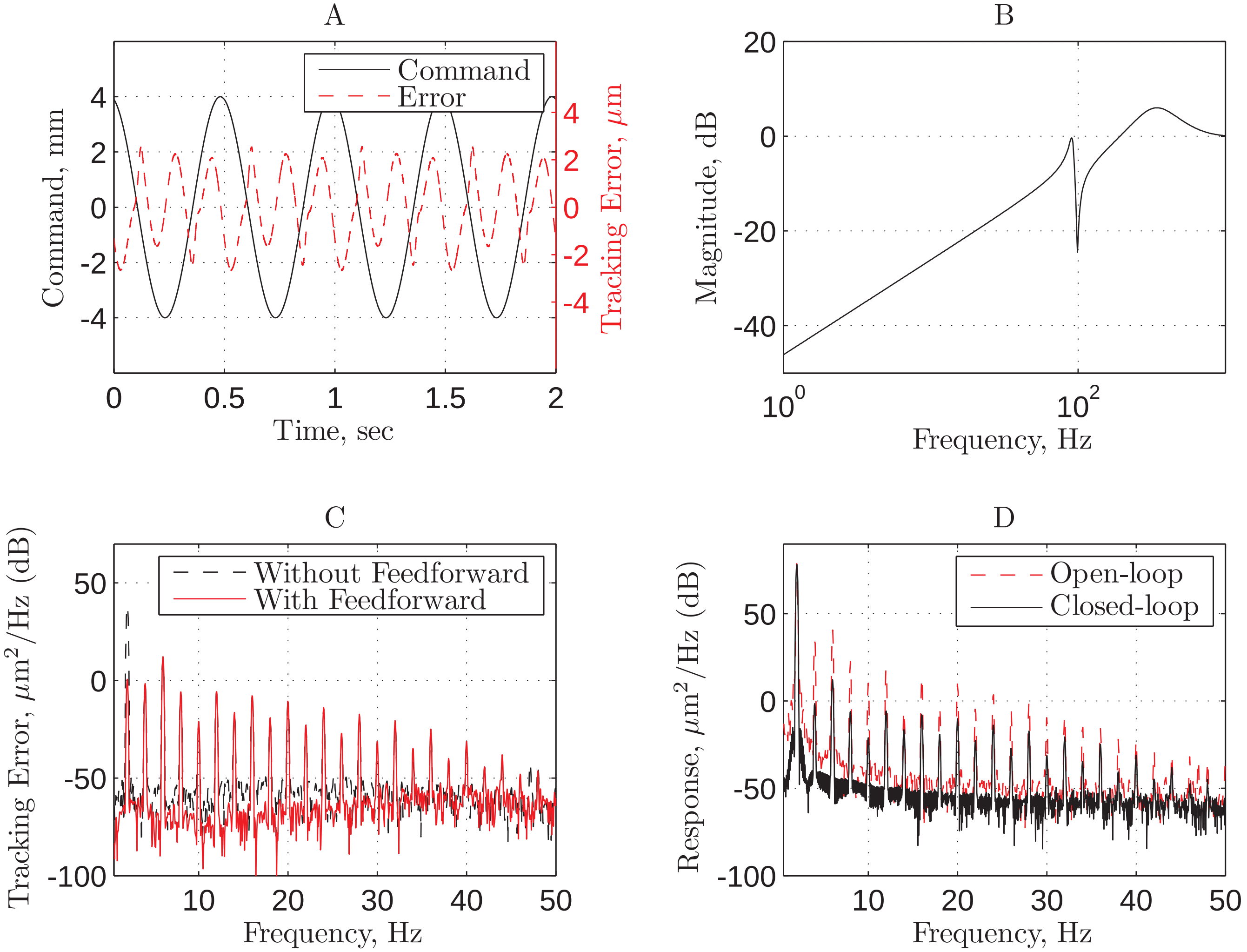

Fig. 3.8: Tracking performance with linear feedback controller. (A) Position command and tracking error. (B) Sensitivity transfer function of the feedback loop. (C) Power spectrum of the tracking error. (D) Power spectrum of position response.

fer function. To achieve greater reduction of the harmonics, the sensitivity transfer function would have to be reduced further in the low frequency range. However, this can be done only at the cost of decreasing the stability robustness, given the actuator saturation concerns due to low open-loop bandwidth of the plant. This is a direct consequence of the analytic design tradeoff associated with the feedback loop, known as the *Bode waterbed effect* [82]. To explain this further, consider the following bounds on the sensitivity and the complementary sensitivity transfer functions:

$$|S(j\omega)| \leq \alpha < 1, \quad \forall \quad \omega \leq \omega_1 \tag{3.6}$$

$$|T(j\omega)| < \varepsilon \left(\frac{\omega_c}{\omega}\right)^{1+k}, \quad \forall \quad \omega > \omega_c \tag{3.7}$$

where α demotes the upper bound of the sensitivity transfer function in the low frequency range up to ω_1 rad/s; $\varepsilon < 1/2$ and $k > 0$ constrain the roll-off rate and the gain of the closed-loop transfer function, respectively, after the corner frequency denoted by ω_c. Then, it can be shown that [82]

$$\sup_{\omega \in (\omega_1, \omega c)} \log |S(jw)| \geq \frac{1}{\omega_c - \omega_1} \left\{ \omega_1 \log \left(\frac{1}{\alpha}\right) - \frac{3\varepsilon\omega_c}{2k} \right\} \tag{3.8}$$

Equation (3.6) conveys the low-frequency sensitivity reduction requirement associated with the feedback loop for improving the tracking performance. The closed-loop bandwidth constraint in Eq. (3.7) results from actuator saturation, given the low open-loop plant bandwidth. Also, such constraint is necessary to increase robustness against unmodeled high frequency plant dynamics. However, from Eq. (3.8), sensitivity reduction at low frequencies can only be achieved by increasing the lower bound on the peak of sensitivity function at intermediate frequencies, which results in loss of stability robustness. This trade-off is also shown graphically in Fig. 3.9. This implies that there is a limit to improving the tracking performance of the system by employing a feedback loop because of its low open-loop bandwidth. In other words,

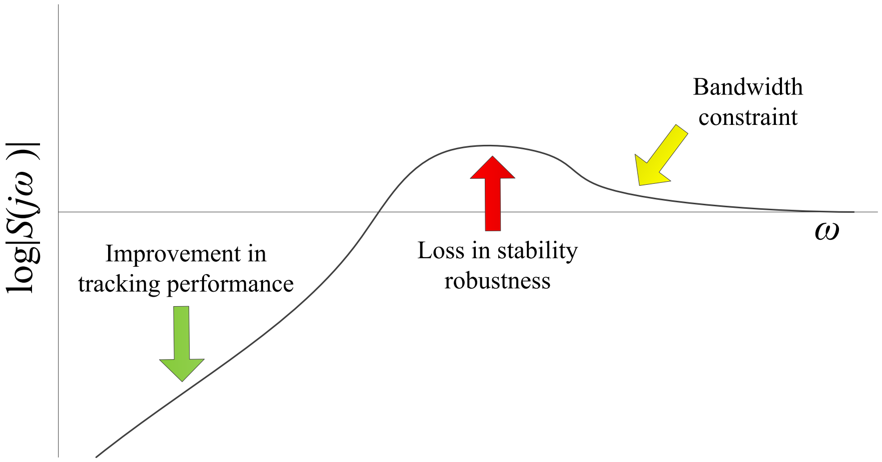

Fig. 3.9: Trade-offs arising from the Bode waterbed effect

sensitivity reduction at low frequencies can only be achieved by increasing the lower bound on the peak of sensitivity function at intermediate frequencies, which results in loss of stability robustness.

From Fig. 3.8(C), it can be seen that the deterministic part of the tracking error due to the nonlinearities as well as due to lack of command following is relatively large compared to the stochastic part due to various sources of noise and disturbance mentioned earlier. Moreover, if the command signal is periodic, then the deterministic part of the error also repeats every period. Therefore, in such cases, iterative learning control could be applied in conjunction with feedback in order to reduce the deterministic or the repeating portion of the tracking error [100, 105]. As explained in the next section, this is done by modifying the control signal based on learning from the error histories obtained during previous iterations.

3.4 Iterative Learning Control: Design and Implementation

3.4.1 Overview of ILC

The iterative learning control (ILC) block diagram incorporated with the feedback loop in shown in Fig. 3.10. Here, P, C, and F denote the plant, the feedback

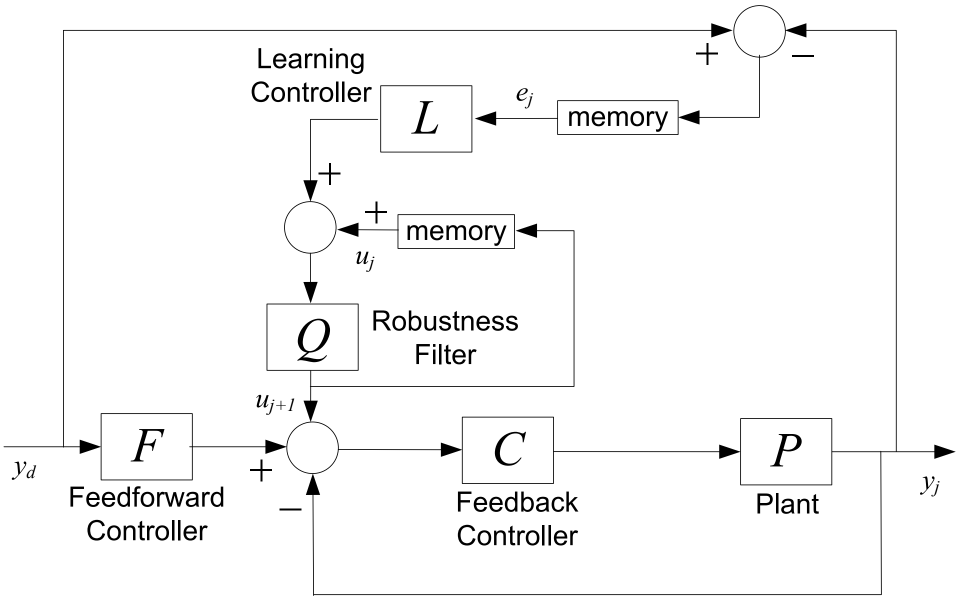

Fig. 3.10: Iterative learning control architecture

compensator, and the feedforward compensator, respectively. $y_d(k)$ is a periodic command signal and $y(k)$ is the measured response. The objective of ILC is to generate a feedfoward command $u(k)$ in order to reduce the tracking error $e(k) = y_d(k) - y(k)$. The tracking error $e_j(k)$ and the ILC input $u_j(k)$ are stored in a memory for every iteration j and time instant k. The ILC algorithm then evaluates the new input signal, $u_{j+1}(k)$, in an offline manner, to be applied during the next iteration. The iteration period can be chosen as the command period or any multiple of the command period. The arrangement shown is also known as the serial ILC architecture because the ILC input is added to the command before the feedback loop. Although a serial architecture is chosen here, a similar analysis and design procedure could be followed to implement an equivalent parallel ILC architecture [105]. Since the implementation of ILC (storing, processing, and retrieving, of error signals) is usually performed using a digital computer, it is beneficial to start with a discrete-time formulation [100].

A first-order classical ILC update law is given as follows [100]:

$$u_{j+1}(k) = Q(z)[u_j(k) + L(z)e_j(k)] \tag{3.9}$$

where $L(z)$ and $Q(z)$ are known as the learning filter and the robustness filter, respectively. The design of these filters determines the performance and the robustness of the ILC algorithm as described next [105, 106].

With the assumption that the feedback loop is stable and linear time-invariant, a sufficient condition guaranteeing stability and monotonic convergence of the tracking error in successive iterations is given by the following standard frequency-domain result:

$$|Q(z)[1 - L(z)T(z)]| < 1, \; z = e^{i\omega T} \; \forall\omega \tag{3.10}$$

where $T(z)$ represents the z-transform of the closed-loop transfer function, and $|.|$ refers to H_2 norm. The error dynamics is given by the following relation:

$$(e_\infty(k) - e_{j+1}(k)) = Q(z)(1 - L(z)T(z))(e_\infty(k) - e_j(k)) \tag{3.11}$$

Additionally, it can be shown that given the initial tracking error, $e_0(t)$, the tracking error finally converges to

$$e_\infty(k) = \frac{1 - Q(z)}{1 - Q(z)(1 - L(z)T(z))} e_0(k) \tag{3.12}$$

One of the inherent assumptions in the derivation of Eq. (3.10)–(3.12) is that the system returns to the same initial state at the start of every iteration. However, this assumption is too restrictive and, in general, the final converged error can be shown to be bounded in the presence of bounded initial conditions [107]. In case of the motion system following a continuous sinusoidal or triangular command, while operating under a closed-loop feedback, the initial conditions would be bounded by some finite error, which may consist of a bias as well as random variations.

3.4.2 ILC Design

From Eq. (3.11), it can be deduced that the learning filter determines the rate of convergence of tracking error in successive iterations. Specifically, the magnitude of $(1 - L(z)T(z))$ should be small for fast convergence. Since the closed-loop transfer function $T(z)$ is designed to have unity magnitude up to a frequency range of approximately 400 Hz (see Fig. 3.5), $L(z)$ can be simply chosen as $L(z) = \lambda z^{\gamma}$ with $\lambda \leq 1$ as a constant gain and $\gamma > 0$ representing the linear phase lead, resulting in a linear phase lead type iterative learning controller [100]. While higher values of λ leads to aggressive learning, smaller gains makes the learning process less sensitive to noise and lead to lower final errors. Also, because λ is a constant gain, it can be easily tuned online while performing experiments. Secondly, $\gamma > 0$, which helps compensate for the phase loss in $T(z)$, is chosen to satisfy the stability criterion, resulting in a non-causal transfer function. Non-causal implementation is not an issue because the ILC computation is performed retrospectively, in an offline manner, once per trajectory repetition.

The robustness filter $Q(z)$ is usually chosen to be a low pass filter with the bandwidth, ω_n, of $Q(z)$ presenting a trade-off between performance and robustness. As seen from Eq. (3.12), choosing $Q(z)$ as unity ensures convergence to zero tracking error. The Nyquist plot of $Q(z)(1 - L(z)T(z))$ for $\lambda = 0.5$, $\gamma = 0$ and $Q(z) = 1$ is shown in Fig. 3.11. The plot goes outside the unit circle at the frequency of about 280 Hz, thereby violating the monotonic convergence criterion given in Eq. (3.10). The phase lead z^{γ} can be used to increase the bandwidth of the Q filter. Also plotted in Fig. 3.11 is the Nyquist plot of $Q(z)(1 - L(z)T(z))$ for $\lambda = 0.5$, $\omega_n = 500$ Hz, and $\gamma = 6$. The curve remains within the unit circle over the entire frequency range with the maximum value of $|Q(z)(1 - L(z)T(z))|$ being 0.93. Simulations showed that the overall system remains stable for plant gain variations up to 45%. The Q filter is designed as a 5th order Butterworth filter to obtain a sharp cut-off. Moreover, since

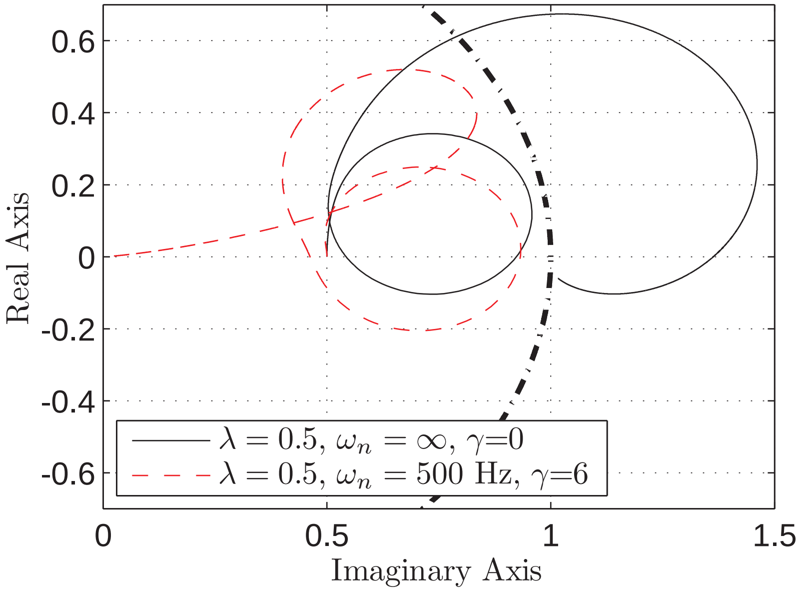

Fig. 3.11: Nyquist plot for monotonic convergence criterion

the filtering is done in an offline manner, $Q(z)$ is designed to be non-causal, using the *filtfilt* function [104] in Matlab™. This function performs signal filtering in both the forward and the reverse directions, resulting in zero-phase error in the filtered signal.

3.4.3 ILC Implementation

Figure 3.12 shows the scheme adopted for the implementation of the ILC. The error signal $e_{j-1}(k)$ and the ILC input signal $u_{j-1}(k)$ are stored in a memory buffer during the $(j-1)^{th}$ iteration. The buffers already contain signal values from the previous two iterations. During iteration j, these buffers are then used to compute the ILC control signal for $(j+1)^{th}$ iteration according to the following modified ILC law:

$$u_{j+1}(k) = Q(z)[u_{j-2}(k) + L(z)e_{j-2}(k)] \tag{3.13}$$

The resultant ILC control input $u_{j+1}(k)$ is then unbuffered and applied to the feedback loop during the $(j+1)^{th}$ iteration. Although Eq. (3.13) differs from the standard ILC law, given in Eq. (3.9), it provides an advantage from the point of view

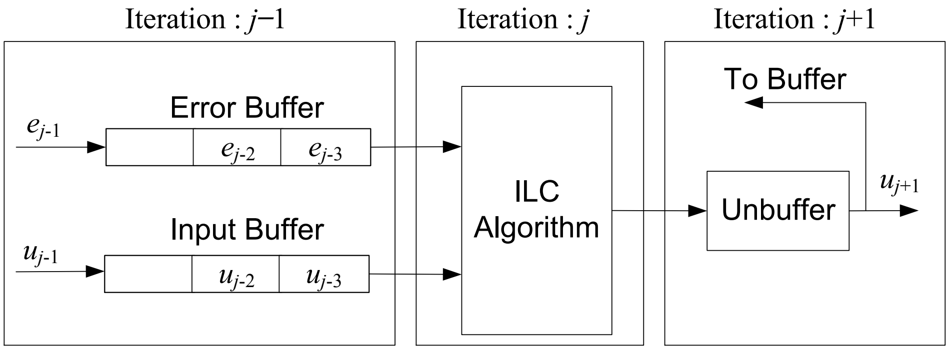

Fig. 3.12: ILC offline implementation

of non-causal implementation. As shown in Fig. 3.12, the memory buffers contain signal values for three iterations. In order to facilitate an error-free non-causal filtering of middle stack ($e_{j-2}(k)$ and $u_{j-2}(k)$), the knowledge of data before and the after the $(j-2)^{th}$ iteration helps to set the filter initial conditions for both the forward and the reverse directions. Since the ILC computation takes more than 0.1 ms, corresponding to 10 kHz loop-rate, the updated ILC control signal is applied in the $(j+1)^{th}$ iteration instead of the j^{th} iteration. Therefore, while the feedback computations are done at the sampling rate, the ILC calculation is carried out only once per iteration.

The final code implemented on the dSPACE™ microcontroller is described in Appendix A.

3.5 Experimental Results

3.5.1 Sinusoidal Command Tracking

The combined feedback and ILC controller described above was applied to the single-axis nanopositioning system. Figure 3.13 shows the resulting tracking performance for a 4 mm amplitude (i.e., 8 mm peak-to-peak), 2 Hz sinusoidal command. Based on the ILC design described earlier, the learning gain (λ), phase lead parameter (γ), and Q filter bandwidth (ω_n) were set to 0.5, 6 and 500 Hz, respectively. Figure 3.13(A) shows the decrease in the tracking error as a function of the iteration

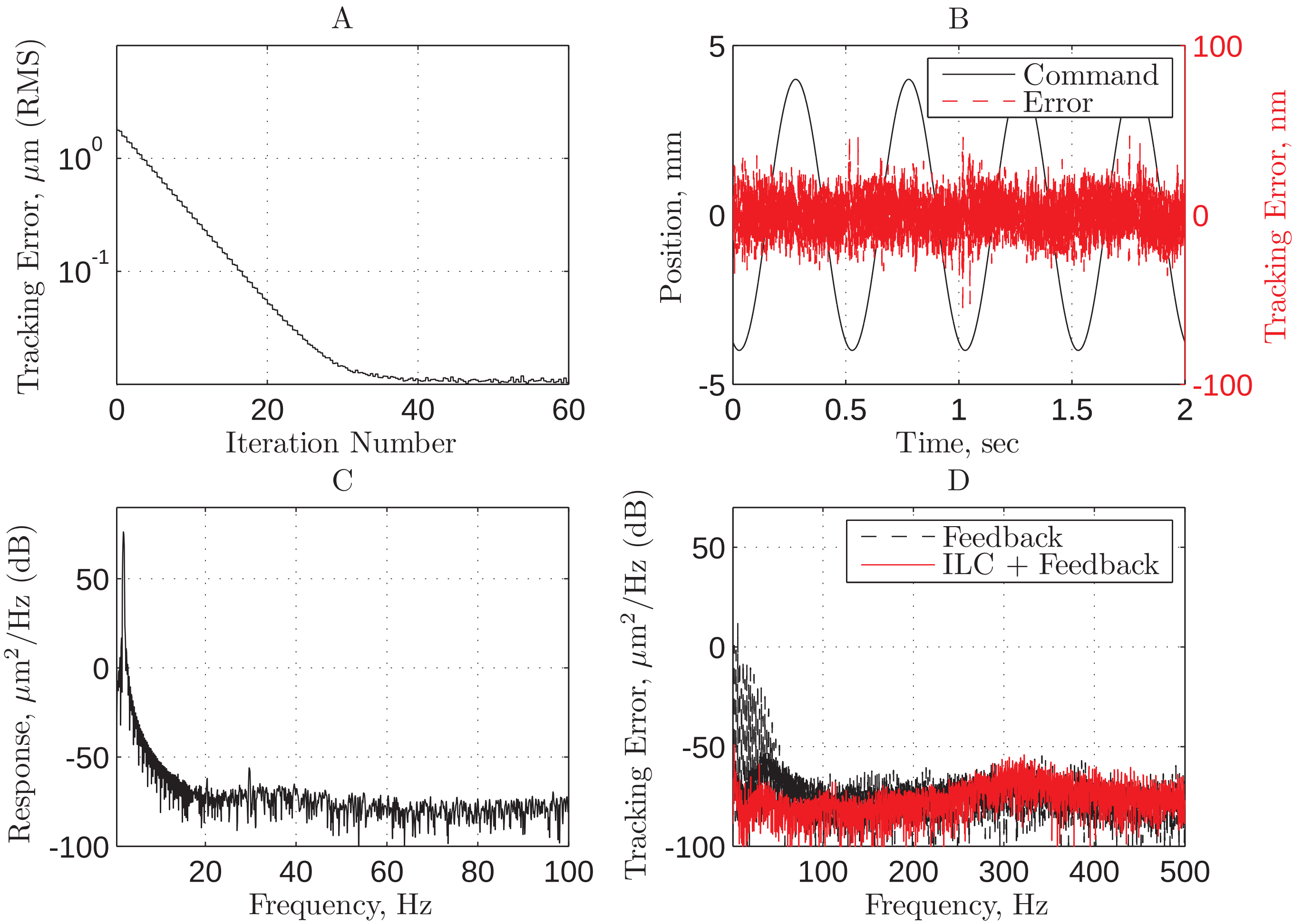

Fig. 3.13: Tracking performance with combined feedback and ILC. (A) Tracking error convergence. (B) Position command and tracking error after 40 iterations. (C) Power spectrum of position response. (D) Power spectrum of tracking error.

number. The RMS of the tracking error is reduced from about 1.8 μm to 10 nm in approximately 40 iterations. This corresponds to a reduction by a factor of about 180 in 20 seconds. The tracking error at the end of the 40th iteration is plotted in Fig. 3.13(B). The performance improvement, compared to linear controller by itself, comes from a reduction in the repeating portion of the tracking error at the command frequency and its harmonics (Fig. 3.13(D)). The ILC input follows a profile similar to the tracking error, because of the use of constant gain type learning controller. The dynamic range of the nanopositioning system, defined as the ratio of the RMS command (2.83 mm) to that of the RMS tracking error (10 nm), is equal to 2.83×10^5. The power spectrum of the converged position response, shown in Fig. 3.13(C), reflects the true dynamic range of the nanopositioning system.

3.5.2 Triangular Command Tracking

In a separate experiment, a 4 mm and 2 Hz band-limited triangular waveform was applied as the command. The signal was optimized to have a perfectly linear (constant velocity) region within ±2 mm while minimizing the power content beyond the first three harmonics [108]. The motion speed in the linear region is 32 mm/s. As compared to sinusoids, multi-tone command signals are more challenging to follow since they give rise to the intermodulation products in addition to the harmonics. Even in this case, the tracking error after 40 iterations (Fig. 3.14(A)) is reduced to 10 nm RMS. The power spectrum of the measured response and the tracking error are shown in Fig. 3.14(B).

3.6 Closure

In this chapter, application of ILC is shown to improve the tracking performance of a large range single-axis flexure-based nanopositioning system. The resultant tracking error is approximately two times larger than the sensor resolution, leaving some scope

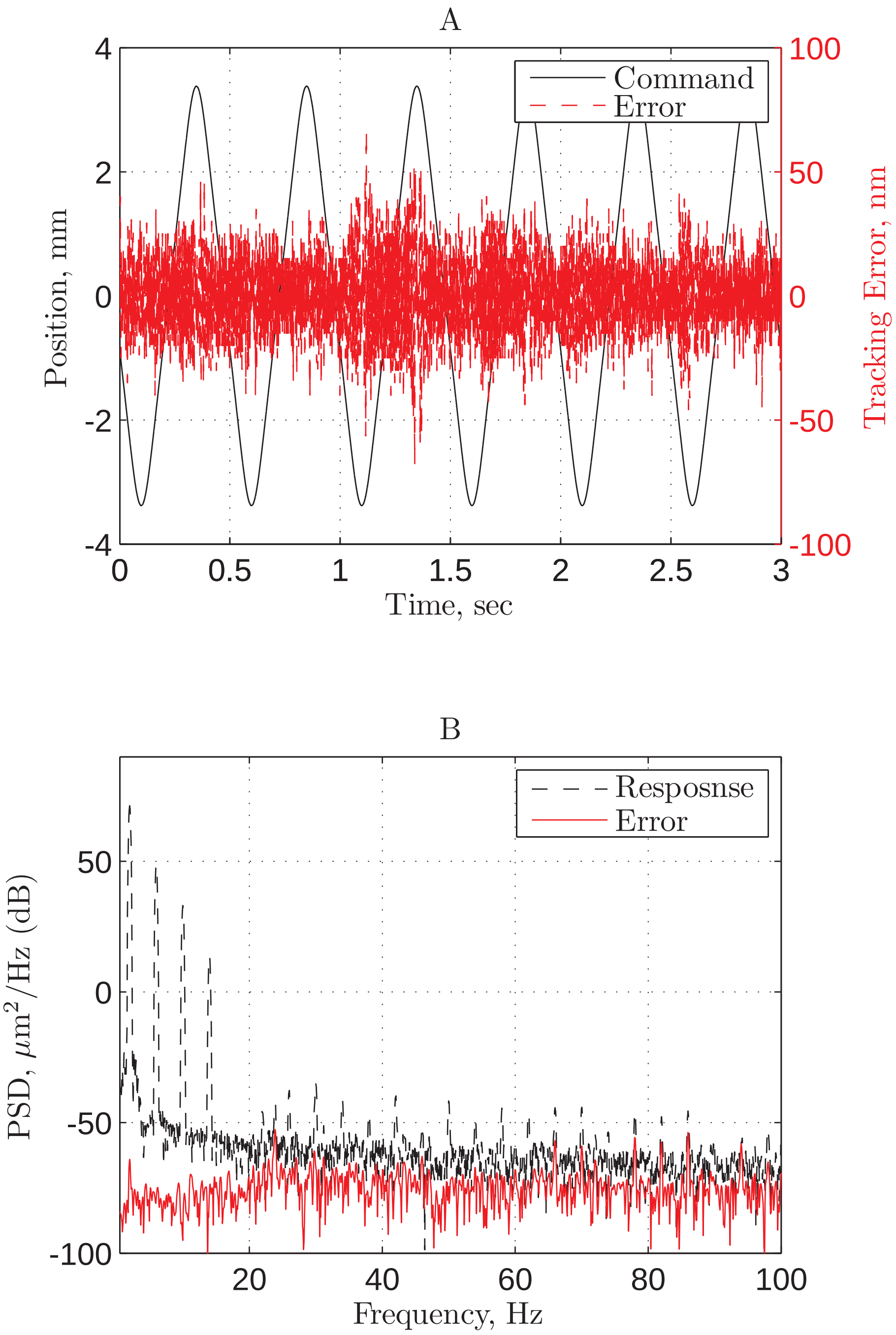

Fig. 3.14: Tracking performance for an optimized triangular command. (A) Time response. (B) Power spectrum.

for further improvement. It should be noted that the sensor noise contributes to the random component of the tracking error. In this regard, averaging of the ILC input [109] should be investigated to further reduce the tracking error.

One of the reasons for the slow error convergence rate (about 40 iterations) is the fact that two extra iterations are needed in the ILC implementation using Eq. 3.13, as compared to the classical update law given in Eq. 3.9. As discussed in Section 3.4.3, Eq. 3.13 enables error-free non-causal filtering as well as provides extra time for offline computation. If the non-causal filtering with zero initial conditions does not have an significant effect on the converged error, and the ILC implementation can be optimized to enable the computation time less that one sampling-period, then the classical update law could be used. This should ideally decrease the convergence time by a factor of two. Secondly, since a large component of the repeating error lies in a the frequency range less than 50 Hz, the learning filter could be redesigned to have high gain value in the low-frequency region and decreasing gains thereafter [100]. This will also lead to faster learning without sacrificing the ILC stability robustness.

Instead of using ILC, another possible approach could have been to apply a model inversion type feedforward controller based on a nonlinear model. Two known sources of nonlinearities in the physical system are the actuator and its driver. In this regard, an attempt was made to implement feedback linearization to cancel the force-displacement nonlinearity of the actuator. While this reduces the harmonics seen in the position output to some extent, it was still inadequate. With the final aim of achieving a high dynamic range of more than 10^5, this approach requires a highly accurate model or identification of the nonlinearities, obtaining which is not easy. One of the reason being that the sensors used to characterize these nonlinearities in various components themselves suffer from nonlinearities in their input-output behavior. Additionally, nonlinearities in the driver and the actuator vary with the power level and experimental setup assembly, respectively. In the presence of such nonlinearities that are variable and difficult to model accurately, ILC proves to be a much more pragmatic approach. This is because it does not require any knowledge of the nonlinearities. The only drawback of ILC is that it works only for repetitive or periodic commands, which is acceptable for the targeted scanning-type applications. However, compensation of nonlinearities would bring down the tracking error due to feedback alone, thereby reducing the convergence time for the ILC.

CHAPTER IV

Dynamic Modeling of XY Flexure Mechanism[1]

The objective of this chapter is to model the low frequency dynamics of XY flexure mechanism, comprising double parallelogram flexure modules, in order to understand the unexplained variation in the zero dynamics observed around 150 Hz. While it becomes important to consider geometric nonlinearities due to large beam deformation, several simplifying assumptions are made, without sacrificing its ability to capture relevant dynamics, to come up with the simplest competent model that provide significant insights. Using the derived model, it is shown that kinematic coupling, due to geometric nonlinearities in the beam mechanics and small dimensional asymmetry, may conspire to produce complex-conjugate NMP zeros at certain operating points in the mechanism's workspace. This finding is the main contribution of this chapter. In the future, such modeling effort would in turn pave the way for structural optimization or modification of mechanisms in the design phase itself to avoid the NMP phenomenon and thereby ensure improved control system performance. Even though this research is motivated by a specific mechanism, the modeling approach presented here is broadly applicable to flexure mechanism undergoing large beam deformations.

---

[1] This work was done in collaboration with Leqing Cui and Kai Wu in the Precision Systems Design Laboratory at the University of Michigan.

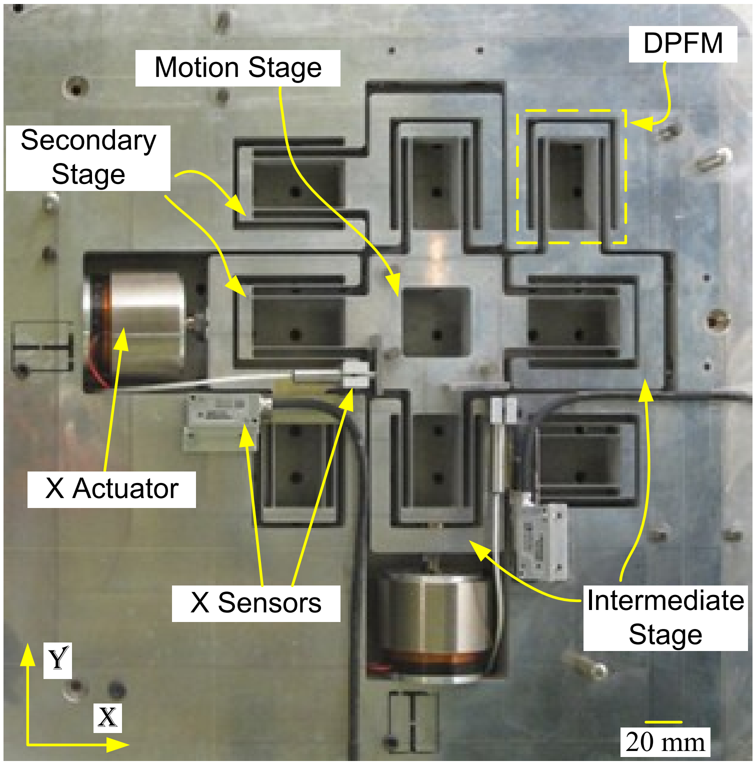

Fig. 4.1: Large range XY nanopositioning system

4.1 Physical System Description

Shown in Fig. 4.1 is the XY nanopositioning system that employs a parallel-kinematic flexure mechanism to achieve a motion range of 10 mm × 10 mm. This flexure mechanism [57] consists of eight symmetrically-placed, double parallelogram flexure modules (DPFMs). This unique layout provides a high degree of geometric decoupling between the two motion axes (X and Y) by avoiding geometric over-constraint, provides actuator isolation that allows the use of large-stroke single-axis actuators, and enables a complementary end-point sensing scheme using commonly available sensors [110]. The experimental setup is described below in further detail.

4.1.1 Flexure Bearing

The flexure bearing was designed [57] to minimize in-plane and out-of-plane parasitic error motions as well as cross-axis coupling between the X and Y directions over the motion range of interest. The critical dimensions are as follows: center-to-center distance between adjacent DPFMs is 46.25 mm; beam length is 47.5 mm; beam in-plane thickness is 0.63 mm, beam out-of-plane height is 25 mm; and, inner and outer beam spacing in each DPFM are 12.81 mm and 18.44 mm, respectively. The flexure bearing along with the ground frame that is used for mounting all sensors and actuators was created monolithically from a 25.4 mm thick AL6061-T651 plate, machined down to 25 mm, using wire- Electric Discharge Machining (EDM). The flexure bearing spans a 255 mm × 255 mm area in the center, while the outer dimensions of the ground frame, and therefore the overall system, are 385 mm × 385 mm.

4.1.2 Sensors

A linear optical encoder (RELM scale, Si–HN–4000 Read-head, and SIGNUM Interface from Renishaw, 5 nm resolution, 80 mm range) is employed as the first X sensor between ground and intermediate stage. The resolution of a linear encoder is limited by its line grating period and electronic interpolation, and its digital output makes it immune to electronic noise. The encoder scale is mounted on the intermediate stage while the encoder read-head is fixed to the ground, which allows easy routing of the read-head cable.

It was verified experimentally as well as analytically that the relative X displacement between the intermediate stage and the motion stage is of the order of tens of microns over the entire motion range of the system [57]. Accordingly, a capacitance probe (Model # C23–C, Driver # CPL290 Elite Series, from Lion Precision, 1 nm resolution, 50 µm range) is selected for the second X sensor. The probe is mounted on intermediate stage using a simple flexure-based clamp, while a high precision Starrett gauge block mounted on the motion stage served as the probe target.

The two sensor signals are fed to a real-time controller, where they are added in order to obtain the net X displacement of the motion stage with respect to the flexure ground. An analogous arrangement is repeated along the Y direction.

4.1.3 Actuators

An off-the-shelf voice coil actuator is used in an inverted configuration to provide actuation along both X and Y directions. Based on the flexure bearing stiffness characteristics, voice coil actuator from BEI Kimco Magnetics (model # LA24–20–000A) was selected. These actuators have a force constant of 11.12 N/A and are capable of 111.2 N bidirectional peak force. In the physical system layout (Fig. 4.1), since intermediate stage is constrained to move only along the X axis with respect to ground, the actuator mover may be directly attached to it. In fact, no additional bearing or decoupling is needed for the actuator, which provides considerable simplicity in the system integration. The permanent magnet of the voice coil actuator is connected to the intermediate stage as the mover, while the coil is attached to the ground frame as the stator. Similar to a moving magnet actuator, this offers two advantages: first, a static coil avoids moving wires, which can be a source of disturbance; and second, the coil, which is a heat source, is separated from the flexure bearing. The ground frame with its greater thermal mass and surface area is better able to channel and dissipate this heat generated in the coil due to actuation current. As mentioned in Chapter II, the only drawback of using a voice coil actuator in an inverted configuration is a large moving mass of the actuator. In the next generation prototype, this voice coil actuator is planned be replaced by a custom-made moving magnet actuator, thereby greatly reducing the actuator moving mass.

Although voice coil actuators offer sufficiently large-range, non-contact, and cog-free motion, the achievable motion resolution and accuracy is limited partly by the noise and distortion in its current driver (or servoamplifier). A current driver provides a direct control of the actuation force and offers a greater actuation bandwidth. A desired dynamic range of 10^7 or 140 dB is extremely difficult, if not impossible, to achieve in practical high-current drivers due to the presence of broad-band noise and harmonic distortions. However, the effect of amplifier noise on motion resolution could be mitigated to some extent via effective controller design. The detailed design and characterization of the servoamplifier is given in Appendix B.

4.1.4 Real-time Control Hardware

The control algorithm is developed in Simulink™ and deployed real-time via dSPACE DS1103 microcontroller. The controller is equipped with 16-bit ADCs and DACs with a SNR greater than 83 dB and 24–bit digital incremental encoder interfaces with a fourfold pulse count rate of 6.6 MHz.

4.2 System Identification

Achieving large motion range as well as nanometric precision and resolution in a nanopositioning system requires good command tracking, noise rejection and disturbance rejection, which in turn require effective feedback control. The design and implementation of a feedback controller requires an understanding of overall system dynamics, particularly the flexure dynamics, for optimal closed-loop performance.

As a first step to understand the dynamics of the XY nanopositioning system, the open-loop frequency response was obtained experimentally via broadband FFT-based system identification technique. Within the frequency range of less than 500 Hz, the actuator, current driver and the sensor can be described by constant gains, independent of any dynamics. Shown in Fig. 4.2, $G_{xx}(s)$ represents the non-collocated transfer function from the force provided by the X actuator to the position of the motion stage along the X axis. Large range of motion in the nanopositioning system implies large deformations in the individual flexure beams, which can make structural non-linearities relevant in the dynamic response. Since structural non-linearities are deformation dependent, the transfer function was measured at various operating

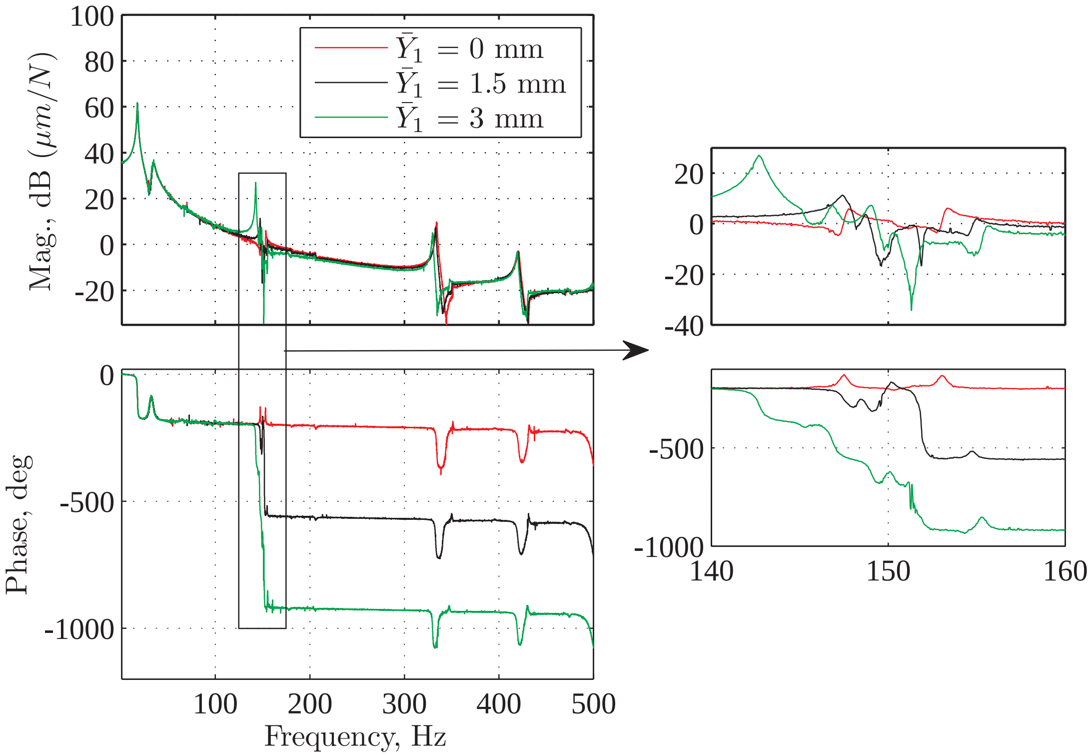

Fig. 4.2: System transfer function along X axis, $G_{xx}(s)$

points in the workspace along the Y axis. Each operating point was realized by sending constant DC offset force commands Y actuator, thereby *pre-distorting* the beams within four of the DPFMs. Shown in Fig. 4.2, the XY flexure mechanism has a first natural frequency at about 18 Hz. The mode shape for this resonance is shown in Fig. 4.3(a), which is the fundamental mode of vibration along the X direction. A similar mode exist along the Y direction as well by virtue of symmetry in the mechanism. However, at operating points (0,1.5) mm and (0,3) mm the transfer function encounters an additional phase drop of 360° or 720°, respectively, near 150 Hz, as compared to the (0,0) mm operating point. As the entire operating range along the Y axis was spanned, no particular trend in this phase drop was observed (only 3 datasets are shown for clarity). It is interesting to note that the transfer function magnitude at the frequencies before and after 150 Hz remains the same for all the operating points.

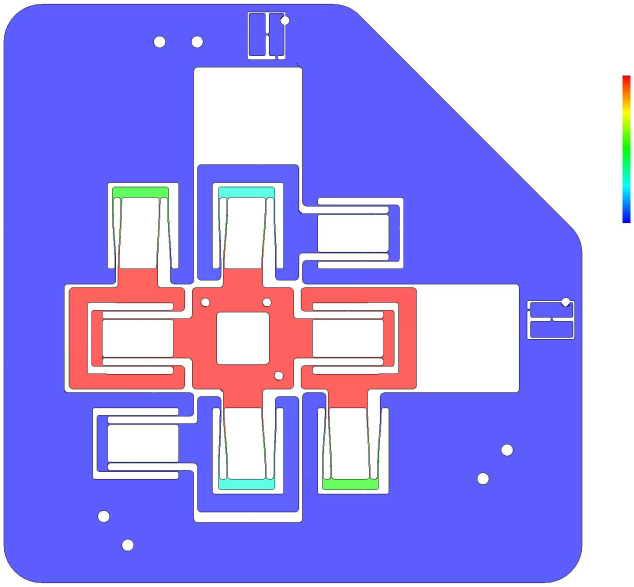

(a) 1st Mode

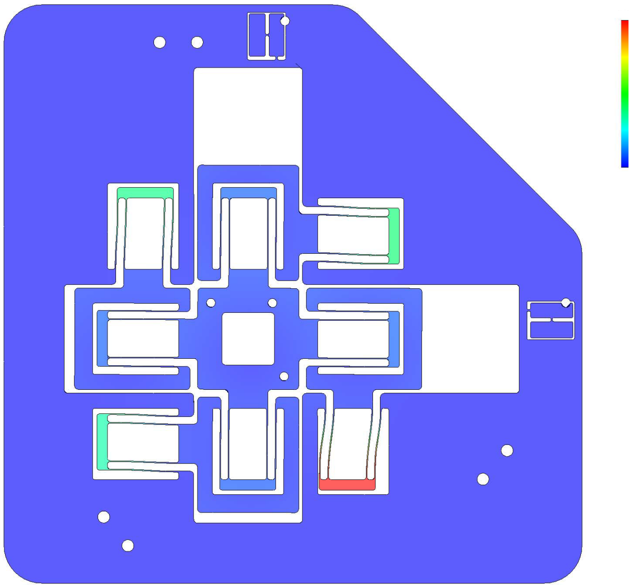

(b) 10th Mode

Fig. 4.3: Modal analysis of XY flexure bearing

This observation, which was found to be repeatable, leads to an inference that some of the complex-conjugate zero pairs migrate to the right-side of the imaginary axis on the *s-plane*, giving rise to the additional phase drop and nonminimum phase (NMP) behavior. A zoomed-in plot (inset) shows the presence of multiple closely-spaced complex-conjugate poles and zeros in the frequency range of 140-160 Hz. A linear modal analysis of the overall flexure mechanism, carried out separately using the finite element method, shows that these dynamics are related to the vibration of the intermediate stages within the DPFMs. There are eight such poles or natural frequencies corresponding to the number of DPFMs. The mode shape at one of these natural frequencies is shown in Fig. 4.3(c). However, these poles are not clearly distinguishable in the figure due to fact that some of the complex-conjugate poles and zeros happen to be very close to each other, leading to approximate pole-zero cancelations.

NMP zeros in the plant transfer function severely restrict the overall performance of the feedback control system. Specifically, the presence of NMP zeros decreases the stability robustness as well as puts hard constraints on the achievable closed-loop bandwidth [111, 112]. This is because as the feedback gain is increased, some of the closed-loop poles move towards right half plane open-loop zeros, leading to instability. Hence, stability margins cannot be arbitrarily increased, resulting in robustness limits. Secondly, complex NMP zeros contribute to additional phase lag, thereby necessitating the gain crossover frequency to be less than the corresponding zero frequency.

Before a low frequency dynamic model of XY flexure mechanism, which explains the variation in the zero dynamics observed around 150 Hz, is attempted, a literature review of the various approaches undertaken to model the dynamics of flexure mechanisms is presented.

4.3 Prior Art

Flexure mechanisms are often employed in precision motion applications due to their ability to produce frictionless and therefore highly repeatable motion. Examples include mirco- and nanopositioning systems used as scanners in scanning probe microscopy [113] and scanning probe lithography [114]. Flexure mechanisms are also used in various MEMS devices [115] because their monolithic construction and compact size is well-suited for micro-fabrication processes. Flexure mechanisms are also used in energy harvesting applications [116] due to their combined functionality of motion guidance and elastic spring behavior. In all these applications, it becomes important to understand the dynamic characteristics of the flexure mechanisms to achieve optimal system-level performance.

Dynamic modeling of rigid link mechanisms with inherent flexibilities, e.g., robotic manipulators, has been studied extensively in the past. An overview and classification of various modeling approaches can be found in the review paper by Dwivedy and Eberhard [117]. Most of the approaches outlined in this paper assume small link deformations to significantly reduce the model complexity. This assumption is justified considering the deformation is generally small relative to the link motion. In contrast to these flexible manipulators in which the majority of motion is achieved by virtue of joints, the motion in flexure mechanisms is entirely due to the large deformations of its constituent links or beams. Large deformations in beams in turn give rise to geometric nonlinearities, which may significantly affect its dynamics even at low frequencies [118]. Da Silva studied the effect of geometric nonlinearities on the dynamics of beams [119, 120] and later extended it to a class of multi-beam structures [118]. The resulting set of nonlinear equations was solved either using perturbation techniques or via numerical methods. However, it would be impractical to extend these modeling and analysis methods in an analytical closed-form manner to more complex flexure mechanisms such as the one presented in this paper.

Much of the research in the field of flexure mechanisms so far has been focused on its kinetostatic design and topology synthesis [96, 121, 122]. However, the dynamic analysis of flexure mechanisms has been increasingly getting more attention. Lan and Lee [123] presented a distributed-parameter dynamic modeling approach of flexure mechanism with large deformation incorporating shear and axial deformations. The resulting equations of motion were solved using numerical methods. Wang and Yu [124] and Akano and Fakinlede [125] used finite element based nonlinear analysis to predict the effect of design parameters on the dynamic performance of flexure mechanisms. Although accurate, these methods are computationally intensive and provide little physical insights. Alternately, lumped-parameters closed-form modeling approaches have been developed. Shilpiekandula and Youcef-Toumi [126] used a lumped-parameter model of a Timoshenko beam to come up with a linear dynamic model of a diaphragm flexure. The resulting model was used to predict the effect of asymmetry due to manufacturing errors on natural frequencies and modal coupling as well as to come up with quantitative performance trade-offs useful for design purpose. Yu et. al. [127] and Boyle et. al. [128] presented a modeling method based on pseudo-rigid-body model for analyzing the dynamics of flexure mechanisms. While this approach also leads to a simple lumped-parameter closed-form model, some of the model parameters still need to be computed using numerical methods. Also, the model parameters vary with the type of loading on the individual constituent beams.

In this chapter, a lumped parameter model of a XY flexure mechanism is derived keeping in mind the relevant geometric nonlinearities. The resulting nonlinear equations of motion are then linearized about varying operating points in the mechanism's workspace in order to predict the existence of complex-conjugate NMP zeros in the transfer function observed via experimental system identification. It should be noted that, while analytical perturbation methods [129] could be applied to solve the set of nonlinear equations, such analysis is not needed here.

The existence of NMP zeros that lie on the real axis, in the non-collocated transfer function of a flexible beam, is well known [130, 131]. Spector and Flashner [130] studied the sensitivities of beam cross-section, material properties, and sensor locations on the locations of poles and zeros via a distributed-parameter Euler-Bernoulli beam model. They showed that, as the sensor is displaced away from the actuator, the complex-conjugate zeros along the imaginary axis migrate towards infinity and reappear along the real axis. Miu [131] provided an physical explanation to these real NMP zeros stating that they are related to the non-propagation of energy within the structural subsystem confined by the actuator and the sensor. However, in the phenomenon reported in this chapter, a zero quartet migrate symmetrically away from the imaginary axis, with one of the pair moving to the right-side of the imaginary axis and the other pair moving to the left-side, the former giving rise to NMP complex-conjugate zeros. In the past, complex-conjugate NMP zeros has been reported in the context of an acoustical transfer function of a room [132], as well as in the non-collocated transfer function of a lumped parameter coupled spring-mass system [133]. However, effect of modal coupling and small structural asymmetry in producing complex NMP zeros in flexure mechanisms has not been shown before as per author's knowledge.

4.4 Dynamic Modeling

The XY flexure mechanism, shown in Fig. 4.1, is designed for a maximum translational displacement of ±5 mm along each axis, corresponding to a maximum individual beam deflection of 2.5 mm or about 5.3% of the beam length. Therefore, it becomes necessary to consider the effect of geometric nonlinearities in the formulation of its dynamics [96]. The XY mechanism consists of eight identical DPFMs, each of which is a serial combination of two parallelogram flexure modules (PFMs). In this section, the force-displacement relationship of a PFM, capturing the relevant geo-

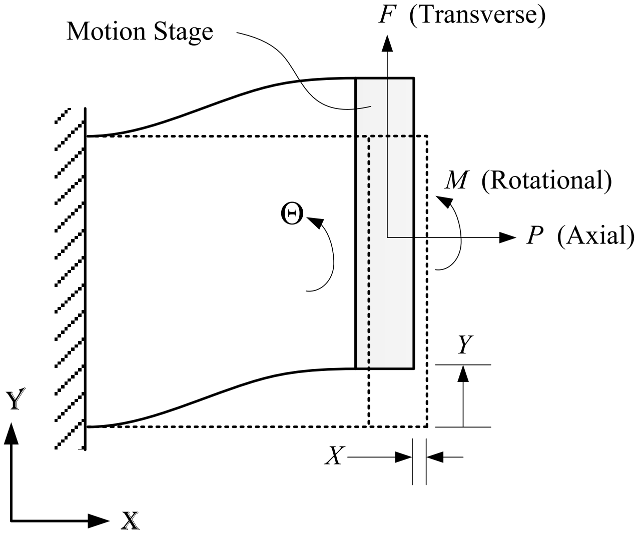

Fig. 4.4: Proposed large range XY nanopositioning system

metric nonlinearities, is used to derive its lumped parameter quasi-static model. This lumped-parameter model is then used as a starting point to derive a dynamic model of two representative, relatively simpler flexure mechanisms, termed as Mechanism I and Mechanism II, that are also constructed from DPFMs. The modeling of these two representative mechanisms provides valuable understanding of the dynamic behavior of flexure mechanisms when geometric nonlinearities are relevant. This modeling approach and associated understanding is then extended to the XY flexure mechanism of Fig. 4.1 in the subsequent section. In the modeling process, several simplifying assumptions are made to keep the resultant model manageable and insightful, without sacrificing its ability to capture relevant dynamics. These assumptions are listed, as they become relevant in the modeling process.

4.4.1 Parallelogram Flexure Module (PFM)

Fig. 4.4 shows a PFM comprising two identical beams connecting the mechanism ground to the motion stage. The PFM is one of the simplest single-axis translational flexure modules, with Y direction representing the degree-of-freedom (or DoF) direction of the motion stage, and X and Θ directions representing the degree-of-constraint (or DoC) directions. The quasi-static force-displacements relations for the PFM, shown to be accurate over a beam deformation within 10% of the beam length, are given below [96]. All the nonlinear terms in these equations arise as a consequence of arc-length conservation of the constituent beams.

$$\frac{Y}{L} = \underbrace{\left\{ \frac{1}{2\left(a - i\frac{P}{EI/L^2}\right)} \right\}}_{c_y} \frac{F}{EI/L^2} \tag{4.1}$$

$$\frac{X}{L} = \underbrace{\frac{1}{2}\left\{ \frac{1}{12}\left(\frac{T}{L}\right)^2 + r\left(\frac{Y}{L}\right)^2 \right\}}_{c_x} \frac{P}{EI/L^2} + \underbrace{i\left(\frac{Y}{L}\right)^2}_{e_x} \tag{4.2}$$

$$\Theta = \underbrace{\frac{1}{2}\left(\frac{L}{W}\right)^2 \left\{ \frac{1}{12}\left(\frac{T}{L}\right)^2 + r\left(\frac{Y}{L}\right)^2 \right\}}_{c_\theta} \left\{ \frac{M}{EI/L} - \frac{c}{a}\frac{F}{EI/L^2} - h\frac{Y}{L}\frac{P}{EI/L^2} \right\} \tag{4.3}$$

Here, F, P, and M represent the forces and moment applied on the motion stage, and Y, X, and Θ are the corresponding displacements and rotation. L and T are the length and in-plane thickness of the beams, respectively, W is the half-spacing between the beams, E is the Young's modulus, and I is the second moment of area of the individual beams about Z axis. The coefficients a, r, i, c, and h are non-dimensional numbers, and assume the values of 12, 1/700, -0.6, -6, and -0.1, respectively, for a uniform cross-section thin beam [96]. The values of all the physical variables used in this chapter are summarized in Table 4.1.

In Eq. (4.1)-(4.3), c_x, c_y and c_θ denote the non-dimensional compliance of the PFM in the X, Y, and Θ directions, respectively. The DoF compliance (c_y) is a function of the axial force on the motion stage and it increases when the axial force is tensile in

Table 4.1: Physical parameters and constants

Parameter	**Symbol**	**Value**	**Units**
Length of the beam	L	47.5	mm
Thickness of the beam	T	0.6	mm
Height of the beam	H	25	mm
Young's Modulus of Aluminum	E	6.9×10^{10}	N/m^2
Moment of inertia of the beam	I	5.1×10^{-4}	mm^3
Mass of the motion stage	m_1	0.284	Kg
Mass of the secondary stage	m	0.018	Kg
Mass of the moving stage	M	0.177	Kg
Mass of the actuator	M_a	0.570	Kg

nature. The DoC compliance (c_x and c_θ) is comprised of two components. The first component arises by virtue of purely elastic effects. The other, known as the elastokinematic component, also has a dependence on the DoF displacement in addition to elastics effects. The elastokinematic component leads to an overall increase in the DoC compliance with increasing DoF motion. Even after the considering the increase in compliance due to abovementioned elastokinematic effect, the compliance of the PFM in the DoC directions ($c_x = 9.2\times10^{-6}$ and $c_\theta = 5.4\times10^{-5}$) remain several orders of magnitude smaller than its compliance along the DoF direction ($c_y = 3.9 \times 10^{-2}$). Therefore, as a first step to simplify the modeling effort, the compliance of the PFM along its constraint directions is neglected. This assumption is justified given our objective of capturing NMP behavior that occurs in the frequency range less than 200 Hz. It was separately confirmed that the constraint directions compliance only affect the dynamics in the frequency range greater than 2000 Hz, for the dimensions given in Table 4.1.

The geometric nonlinearity arising due to beam arc-length conservation leads to the purely kinematic error motion along the X directions due to the DoF or Y direction displacement of PFM. Equation (4.2) also captures this error motion in the axial direction in the non-dimensionalised form, represented by e_x. For the dimensions

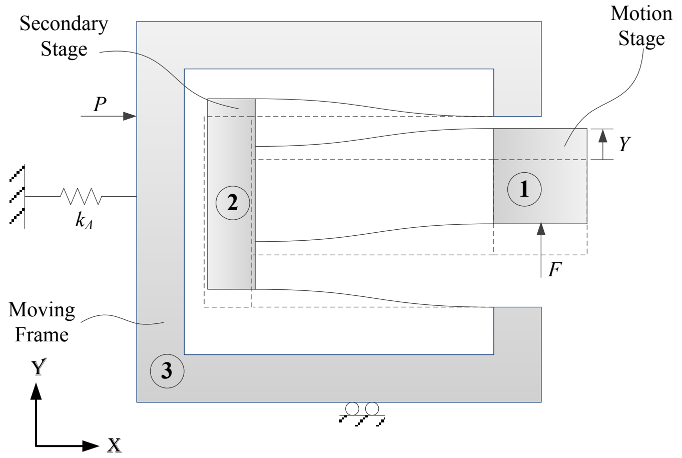

Fig. 4.5: Mechanism I

mentioned in in Table 4.1, the corresponding kinematic error motion in the X direction of the PFM is approximately equal to 0.08 mm, given for a maximum Y direction displacement of 2.5 mm.

Given the abovementioned assumptions, Eq. (4.2)-(4.3) can be simplified as follows:

$$\frac{X}{L} \approx i\left(\frac{Y}{L}\right)^2 \tag{4.4}$$

$$\Theta \approx 0 \tag{4.5}$$

4.4.2 Double parallelogram flexure module (Mechanism I)

In this section, the dynamic model of a representative flexure mechanism, comprising a DPFM, is presented. This model, shown in Fig. 4.5 and referred to as Mechanism I, consists of a motion stage (1) connected to a moving frame (3) via a DPFM, which includes a secondary stage (2). The moving frame is constrained to move only along the X direction. Additionally, the operating point is varied via application a constant force ($\bar{F}$) to the motion stage along the Y direction. The nominal position of the masses at this operating point can be derived using the quasi-static

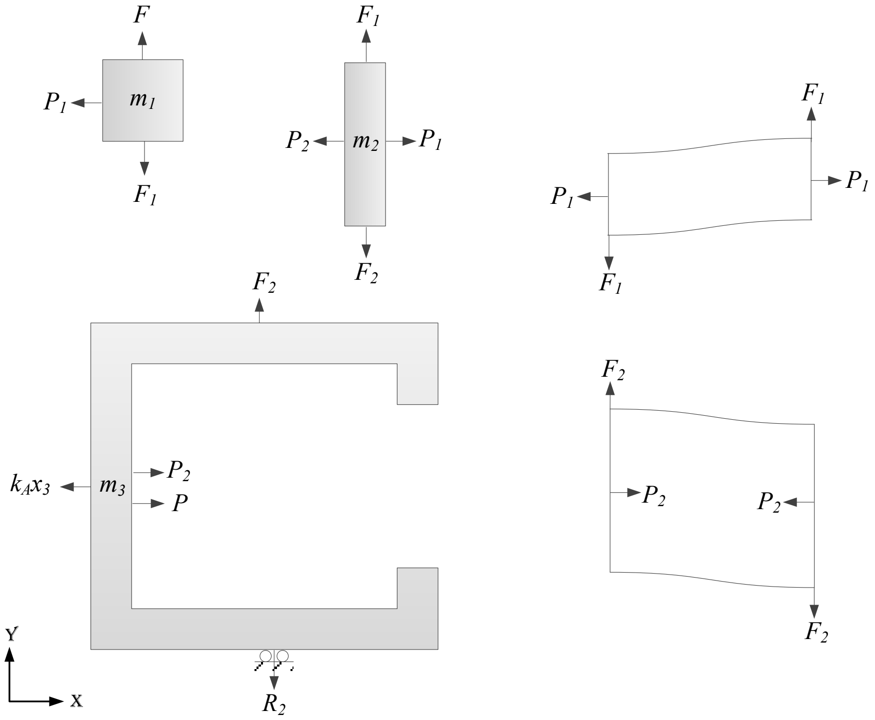

Fig. 4.6: Free body diagram for Mechanism I

force-displacement relations for PFM given in Eq. (4.1) and Eq. (4.4). They are given by:

$$\bar{Y}_1 = 2\bar{Y}_2 = \frac{1}{a}\frac{\bar{F}}{EI/L^3} \tag{4.6a}$$

$$\bar{X}_2 = -i\frac{\bar{Y}_2^{\,2}}{L} \tag{4.6b}$$

$$\bar{X}_1 = \bar{X}_3 = \bar{Y}_3 = 0 \tag{4.6c}$$

Here, the bars on the variables represent their corresponding values at the operating point. The inner and the outer PFMs in the DPFM are displaced equally in their transverse direction. The free-body diagram of the individual members is shown in Fig. 4.6. Here, the mass of the beams is neglected compared to the rigid masses.

Also, without loss of generality, the spring k_A is assumed to have a stiffness equal to that of the transverse stiffness of a DPFM, i.e.,

$$k_A = a\frac{EI}{L^3} \tag{4.7}$$

From the free-body diagram, the corresponding equations of motion can be derived using Eq. (4.1) and Eq. (4.4):

$$-P_1 = m_1\ddot{X}_1 \tag{4.8a}$$

$$F - F_1 = m_1\ddot{Y}_1 \tag{4.8b}$$

$$P_1 - P_2 = m_2\ddot{X}_2 \tag{4.8c}$$

$$F_1 - F_2 = m_2\ddot{Y}_2 \tag{4.8d}$$

$$P + P_2 - k_A X_3 = m_3\ddot{X}_3 \tag{4.8e}$$

$$F_1 L^3 = 2(aE - iP_1L^2)(Y_1 - Y_2) \tag{4.8f}$$

$$F_2 L^3 = 2(aE + iP_2L^2)(Y_2 - Y_3) \tag{4.8g}$$

$$X_1 - X_2 = i(Y_1 - Y_2)^2/L \tag{4.9a}$$

$$X_3 - X_2 = i(Y_2 - Y_3)^2/L \tag{4.9b}$$

$$Y_3 = 0 \tag{4.9c}$$

The above equations are nonlinear in force and displacement. In order to study the frequency response of the mechanism along the X direction, these equations of motion are linearized about a particular operating point using the following notation:

$$X_j = \bar{X}_j + \hat{X}_j \quad ; \quad \hat{X}_j \ll \bar{X}_j \tag{4.10a}$$

$$F_j = \bar{F}_j + \hat{F}_j \quad ; \quad \hat{F}_j \ll \bar{F}_j \text{ ... and so on.} \tag{4.10b}$$

Here, the hat on the variables denotes their perturbations about the operating point. Since there are three masses, each having two DoFs, and three geometrical constraints corresponding to Eq. (4.10), Mechanism I can only have 3 DoFs. The displacement coordinates $\hat{X}_1$, $\hat{Y}_1$ and $\hat{Y}_2$ are chosen arbitrarily to represent these DoFs. The resultant linearized equations of motion derived using Eqs. (4.6)–(4.10). are shown below:

$$\begin{bmatrix} m_1+m_2+m_3 & -\alpha(m_2+m_3) & \alpha(m_2+2m_3) \\ \alpha m_1 & m_1 & 0 \\ \alpha(2m_1+m_2) & -\alpha^2 m_2 & m_2(\alpha^2-1) \end{bmatrix} \begin{Bmatrix} \ddot{\hat{X}}_1 \\ \ddot{\hat{Y}}_1 \\ \ddot{\hat{Y}}_2 \end{Bmatrix}$$

$$+ \begin{bmatrix} k_A & -\alpha k_A & 2\alpha k_A \\ 0 & k & -k \\ 0 & k & -2k \end{bmatrix} \begin{Bmatrix} \hat{X}_1 \\ \hat{Y}_1 \\ \hat{Y}_2 \end{Bmatrix} = \begin{Bmatrix} \hat{P} \\ 0 \\ 0 \end{Bmatrix} \tag{4.11}$$

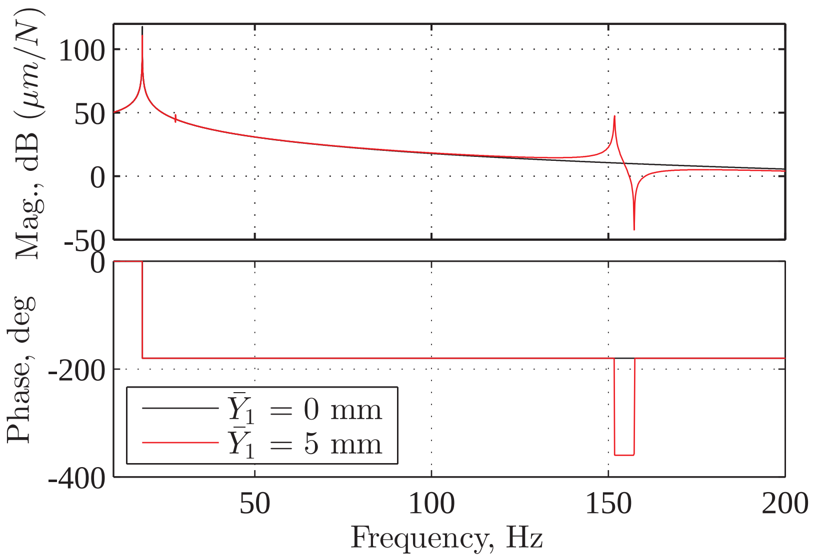

Fig. 4.7: Transfer function, $G_{xx}(s)$, for Mechanism I and Mechanism II

where,

$$\alpha = i\frac{\bar{Y}_1}{L} \quad ; \quad k = 2a\frac{EI}{L^2} \tag{4.12}$$

Here, α is termed as the coupling coefficient, representing the kinematic coupling that exists in the DPFM between its axial and transverse directions. α depends upon the operating point or the initial pre-distortion applied to the PFMs. The remaining two displacements $\hat{X}_2$ and $\hat{X}_3$, can be found out using the following linearized constraint relationship derived from Eq. (4.9) as follows:

$$\hat{X}_2 = \hat{X}_1 - \alpha(\hat{Y}_1 - \hat{Y}_2) \tag{4.13a}$$

$$\hat{X}_3 = \hat{X}_1 - \alpha(\hat{Y}_1 - 2\hat{Y}_2) \tag{4.13b}$$

The non-collocated transfer function, $G_{xx}(s)$, from the X actuation force ($\hat{P}$) to the displacement of the motion stage in the X direction ($\hat{X}_1$) can be derived using Eq. (4.11). $G_{xx}(s)$ is plotted in Fig. 4.7 for the operating point denoted by

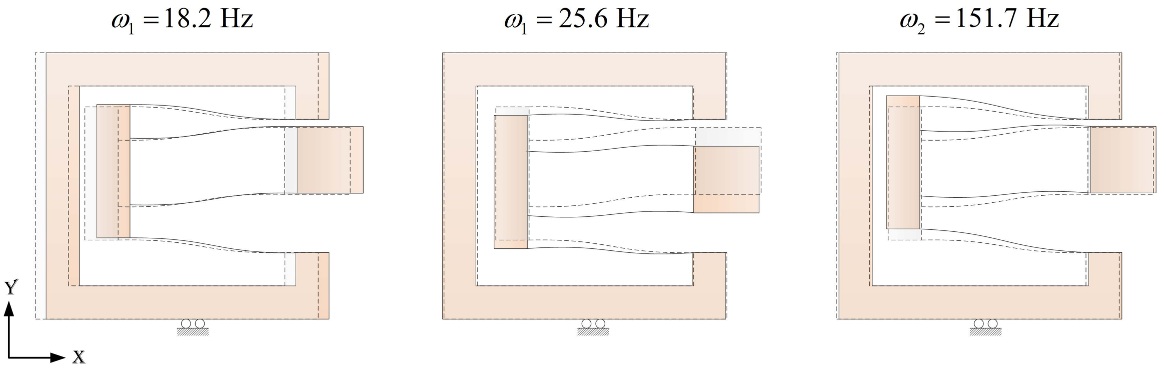

Fig. 4.8: Natural frequencies and mode shapes for Mechanism I

$(\bar{X}_1, \bar{Y}_1) = (0, 0)$ mm and $(0, 5)$ mm. An infinitesimal amount of proportional damping is incorporated in this model to keep the transfer function magnitude finite at resonances. The natural frequencies and the corresponding mode shapes for Mechanism I are shown pictorially in Fig. 4.8 for the latter operating point. Following observations can be made based on the above analysis:

1. In the first mode, corresponding to the natural frequency of 18.2 Hz, all the three masses move in-phase in the X direction with approximately equal amplitudes. This mode is related to the spring k_A. The transverse motion of masses m_1 and m_2 remains small in magnitude.

2. In the second mode, at a natural frequency of 25.6 Hz, masses $m1$ and m_2 move in-phase predominantly along the Y direction with m_1 having twice the amplitude of m_2. This mode occurs due to the transverse bending stiffness of the PFMs. At this mode, the X direction motion of the motion stage is negligible. Hence, this mode does not show up in the transfer function due to approximate pole-zero cancelation.

3. The third mode, corresponding to the natural frequency of 151.7 Hz, is also related to the transverse vibration of secondary stage inside the DPFM. The X direction motion of the masses remains small. Also, in this mode, m_1 (point of sensing)

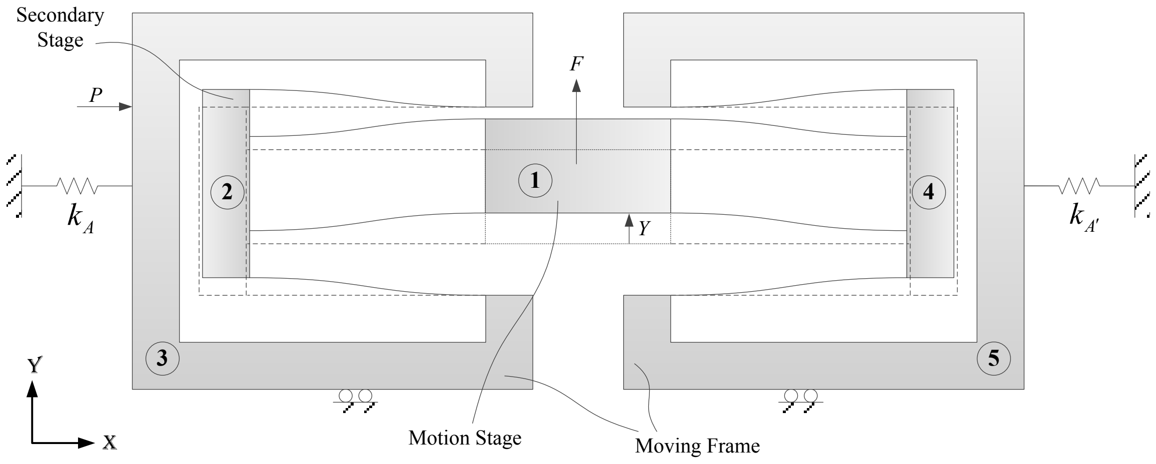

Fig. 4.9: Mechanism II

moves out-of-phase with m_2 and m_3 (point of actuation) in the X direction. In case of the nominal operating point $(\bar{X}_1, \bar{Y}_1) = (0, 0)$ mm, the value of coupling coefficient α is zero. Therefore, the transverse vibration of the secondary stage, in the third mode, has no effect on the motion stage, which acts act as a node. This leads to a pole-zero cancelation. Hence, this mode is not seen in Fig. 4.7 at this operation point. However, for other operating points, the coupling coefficient has a finite value. Therefore, the third mode shows up in the transfer function with the sensor located at mass m_1.

4. Furthermore, with the non-zero value of α, there is no pole-zero cancelation and the minimum-phase zero occurs at the frequency of 157.1 Hz for the operating point $(0, 5)$ mm.

4.4.3 Symmetric double parallelogram flexure module (Mechanism II)

In the next step, the dynamic modeling is extended to the XY flexure mechanism, referred as Mechanism II and shown in Fig. 4.9, which is a symmetrical extension of Mechanism I. All the assumptions from the previous sections are carried over to come up with a linearized set of equation of motion for Mechanism II about varying operating points. While the five masses together have 10 DoF, the two roller supports along with four PFMs provide six constraint equations. Hence, Mechanism II can be described by a 4 DoF model. The displacement coordinates $\hat{X}_1$, $\hat{Y}_1$ and $\hat{Y}_2$ and $\hat{Y}_4$ are arbitrarily chosen to represent these DoFs and the equation of motion for Mechanism II is derived in a similar manner as above. Here, only the finally linearized equations around the operating point $(0, \bar{Y}_1)$ are given by:

$$[M]\begin{Bmatrix} \ddot{\hat{X}}_1 \\ \ddot{\hat{Y}}_1 \\ \ddot{\hat{Y}}_2 \\ \ddot{\hat{Y}}_4 \end{Bmatrix} + [K]\begin{Bmatrix} \hat{X}_1 \\ \hat{Y}_1 \\ \hat{Y}_2 \\ \hat{Y}_4 \end{Bmatrix} = \begin{Bmatrix} 2\alpha \\ 0 \\ 1 \\ \alpha \end{Bmatrix}\hat{P} \tag{4.14}$$

where,

$$[M] = \left[\begin{matrix} \alpha(m_2+2m_3) & -\alpha^2(m_2+2m_3) \\ \alpha(m_4+2m_5) & -\alpha^2(m_4+2m_5) \\ m_1+m_2+m_3+m_4+m_5 & -\alpha(m_2+m_3-m_4-m_5) \\ \alpha(m_2+m_3-m_4-m_5) & -m_1-\alpha^2(m_2+m_3+m_4+m_5) \end{matrix}\right.$$

$$\left.\begin{matrix} (1+\alpha^2)m_2+4\alpha^2 m_3 & 0 \\ 0 & -(1+\alpha^2)m_4-4\alpha^2 m_5 \\ \alpha(m_2+2m_3) & -\alpha^2(m_4+2m_5) \\ \alpha(m_2+2m_3) & \alpha^2(m_4+2m_5) \end{matrix}\right] \tag{4.15}$$

and,

$$[K] = \begin{bmatrix} 2\alpha k_A & -(k+2\alpha^2 k_A) & -2(k+2\alpha^2 k_A) & 0 \\ 2\alpha k_{A'} & -(k+2\alpha^2 k_{A'}) & 0 & -2(k+2\alpha^2 k_{A'}) \\ k_A + k_{A'} & -\alpha(k_A - k_{A'}) & 2\alpha k_A & -2\alpha k_{A'} \\ \alpha(k_A - k_{A'}) & -2k-\alpha^2(k_A+k_{A'}) & -(k+2\alpha^2 k_A) & -(k+2\alpha^2 k_{A'}) \end{bmatrix} \tag{4.16}$$

Here, by virtue of symmetry in Mechanism II, the following equalities hold:

$$m_2 = m_4 \quad ; \quad m_3 = m_5 \quad ; \quad k_A = k_{A'} \tag{4.17}$$

Based on Eq. (4.14) and Eq. (4.17), the transfer function, $G_{xx}(s)$, from the X actuation force ($\hat{P}$) to the displacement of the motion stage in the X direction ($\hat{X}_1$) can be easily derived. $G_{xx}(s)$ turns out to be similar to the corresponding transfer function derived earlier for Mechanism I, shown earlier in Fig. 4.7. The natural frequencies and the corresponding mode shapes for Mechanism II are shown pictorially in Fig. 4.10. The following observations can be made based on this analysis:

1. The similarity in the transfer function, $G_{xx}(s)$, for Mechanism I and II can be attributed to fact that Mechanism II is a symmetrical extension of Mechanism I. Although Mechanism II is described by a 4 DoF model, the transfer function shows only two poles. At the other two natural frequencies, the motion stage behaves as a node in the X direction, leading to pole-zero cancelations in the transfer function at those frequencies.

2. Similar to Mechanism I, at the first mode of Mechanism II at 18.2 Hz, all the masses move approximately with equal amplitude along the X direction. This mode is related to the springs k_A and $k_{A'}$.

3. The second mode at 27.6 Hz is related to the transverse stiffness of PFMs within

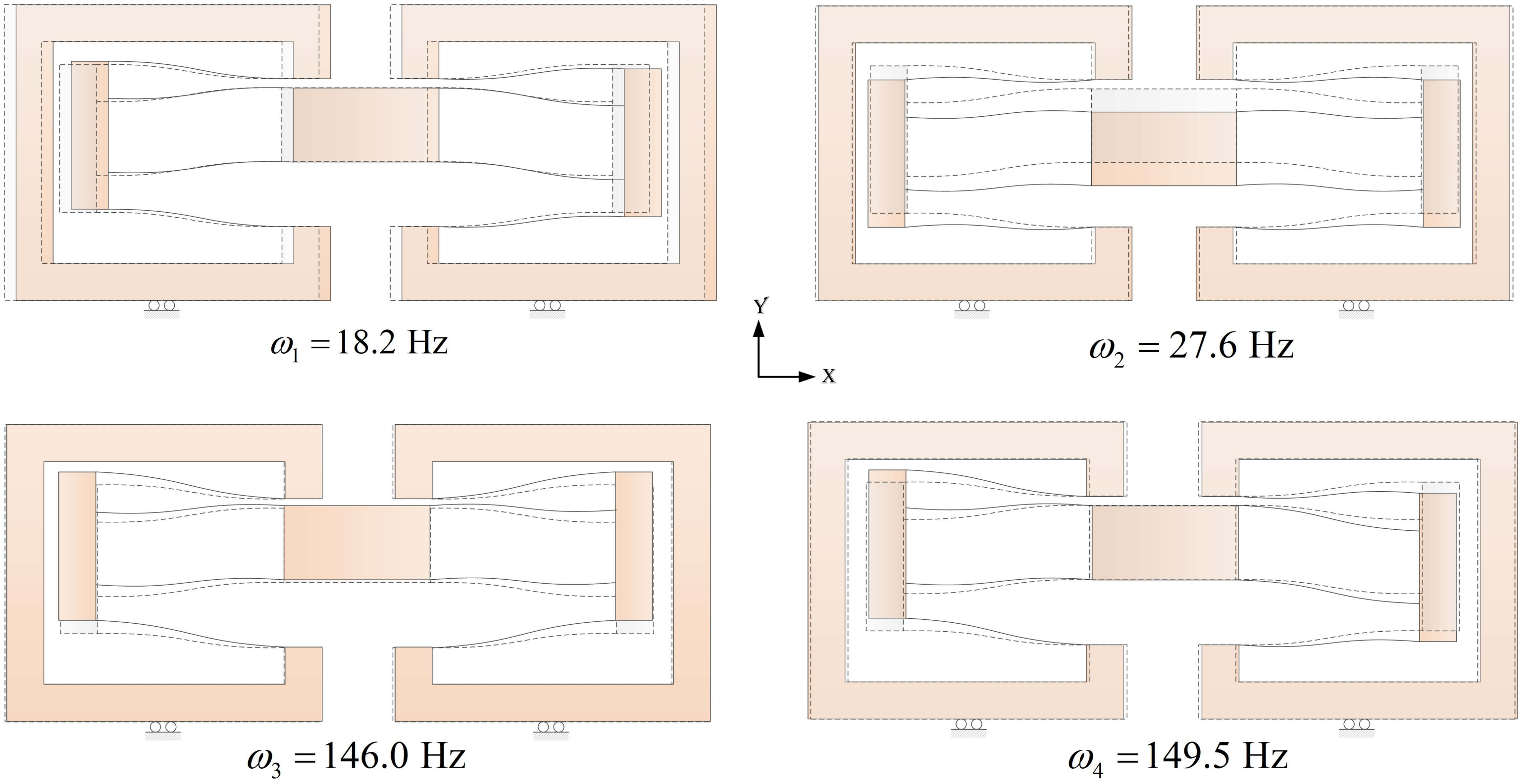

Fig. 4.10: Natural frequencies and mode shapes for Mechanism II

the two DPFMs with m_1 moving in-phase with approximately twice the amplitude compared to m_2 and m_4, in the Y direction. At this frequency, the motion stage has no motion in the X direction.

4. The two higher order modes, at 146.0 Hz and 149.5 Hz, are also related to transverse vibration of PFMs in DPFMs. In this mode, m_2 and m_4 move either in-phase or out-of-phase in the Y direction. When these two masses move in-phase, the motion stage acts as a node in the X direction, again a consequence of structural symmetry. The corresponding pole at 146.0 Hz is therefore not seen in a transfer function due to the pole-zero cancelation. At the other mode at 149.5 Hz, m_2 and m_4 move out-of-phase, leading to a non-zero displacement of the motion stage in the Y direction. Therefore, this mode appears in the $G_{xx}(s)$ transfer function.

5. The only minimum phase zero seen in the transfer function occurs at the frequency of 154.8 Hz.

4.4.4 Effect of Asymmetry

One of the consequences of the structural symmetry in Mechanism II is the pole-zero cancelations in the transfer function. However, some amount of structural asymmetry is always expected in reality due to the tolerances on the dimensions, depending upon the manufacturing processes used. This manufacturing tolerance may manifest itself as mass or stiffness variation in the model given in Eq. (4.17). To study the effect of structural asymmetry on the dynamics of Mechanism II, as an example, a parameter variation in the mass m_2 is introduced as follows:

$$m_2{}' = m_2 \left(1 + \frac{\delta}{100}\right) \tag{4.18}$$

where, $m_2{}'$ is the actual mass, m_2 is the nominal mass, and δ is the percentage deviation in m_2. Substituting Eq. (4.18) back in to Eq. (4.14), we can numerically

Table 4.2: Parameter variation in Mechanism II

Case	**% deviation in m_2**	**NMP zero pairs**
I	-10	0
II	10	1
III	30	0

predict the variation in the poles and zeros of the transfer function of Mechanism II due to variation in mass m_2.

Figure 4.11 shows the variation in the transfer function, $G_{xx}(s)$, for Mechanism II at the operating point of $(\bar{X}_1, \bar{Y}_1) = (0, 5)$ mm for three cases shown in Table 4.2. As opposed to the nominal case shown in Fig. 4.7, there is no pole-zero cancelation in case of mass asymmetry, and two pole pairs are seen around 150 Hz. While the natural frequencies or the pole locations changes with this parameter variation, a dramatic change in the nature of transfer function zeros is observed. If m_2 is lighter by 10% (*Case I*), there are two minimum phase zero pairs on the left of the imaginary axis. However, if m_2 is heavier by 10% (*Case II*), these zero pairs migrate symmetrically

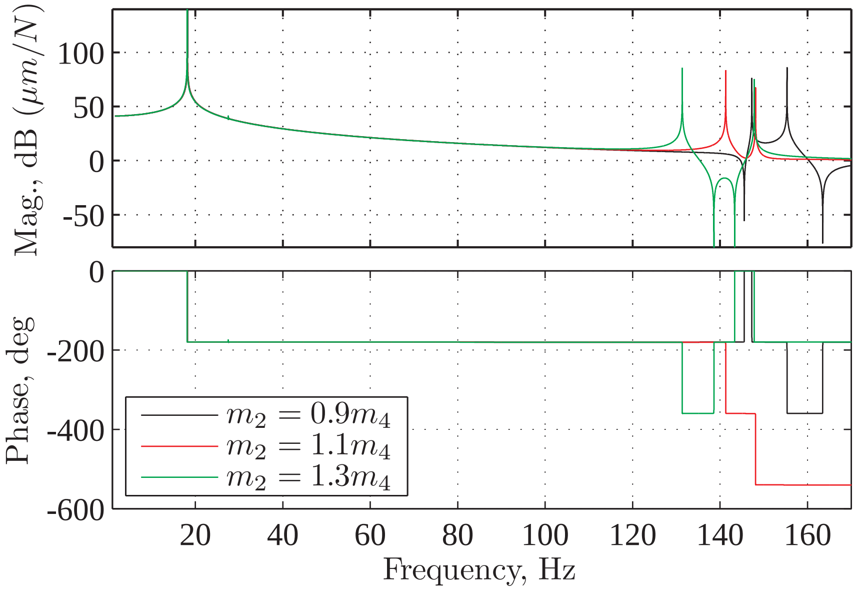

Fig. 4.11: Variation in the transfer function, $G_{xx}(s)$, with variation in mass m_2

on either side of the imaginary axis in the complex plane, giving rise to a pair of non-minimum phase complex-conjugate zeros. This unexpected change in zero behavior leads to an additional 360° drop in phase in the transfer function. Furthermore, as the mass asymmetry is increased to 30% (*Case III*), these zero pairs move back on the left side of the imaginary axis, thus becoming minimum phase again.

In Fig. 4.12, the locus of the zeros for $G_{xx}(s)$ is plotted for different operating points along the Y axis ($\bar{Y}_1$) as well as deviation in mass m_2 (δ). Figure 4.12(a) shows the zero map with varying m_2 for the operating point $(\bar{X}_1, \bar{Y}_1) = (0, 5)$ mm. As the mass asymmetry is increased, the two zero pairs on the left of the imaginary axis move towards each other before they diverge away, symmetrically, with respect to the imaginary axis, on the complex frequency plane. Figure 4.12(b) shows the pole-zero map with varying operating point for $\delta = 10$. The NMP zero behavior is observed for operating points described by $\bar{Y}_1 \geq 2$ mm. This is because with the increase in $\bar{Y}_1$, the coupling term α in Eq. (4.12) increases. This coupling term determines the contribution of the two resonances on the transfer function $G_{xx}(s)$.

In addition to the mass of the secondary stages (m_2 and m_4) and the pre-distortion ($\bar{Y}_1$), the existence of NMP zeros is also sensitive to transverse stiffness (k) of the PFMs in Mechanism II. However, the mass of the motion stage (m_1), the two moving frames (m_3 and m_5), and the springs (k_A and $k_{A'}$) do not affect the zero behavior as much. This is because the dynamics in the concerned frequency range around 150 Hz is dominated by the transverse vibration of the secondary stages.

The variation of transfer function zeros could be explained by considering the modal expansion of the transfer function, $G_{xx}(s)$, as follows:

$$G_{xx}(s) = \underbrace{\frac{r_1}{s^2 + {\omega_1}^2} + \frac{r_2}{s^2 + {\omega_2}^2}}_{\text{M1+M2}} + \underbrace{\frac{r_3}{s^2 + {\omega_3}^2}}_{\text{M3}} + \underbrace{\frac{r_4}{s^2 + {\omega_4}^2}}_{\text{M4}} \tag{4.19}$$

where ω_i are the natural frequencies and r_i are the corresponding residues, and any

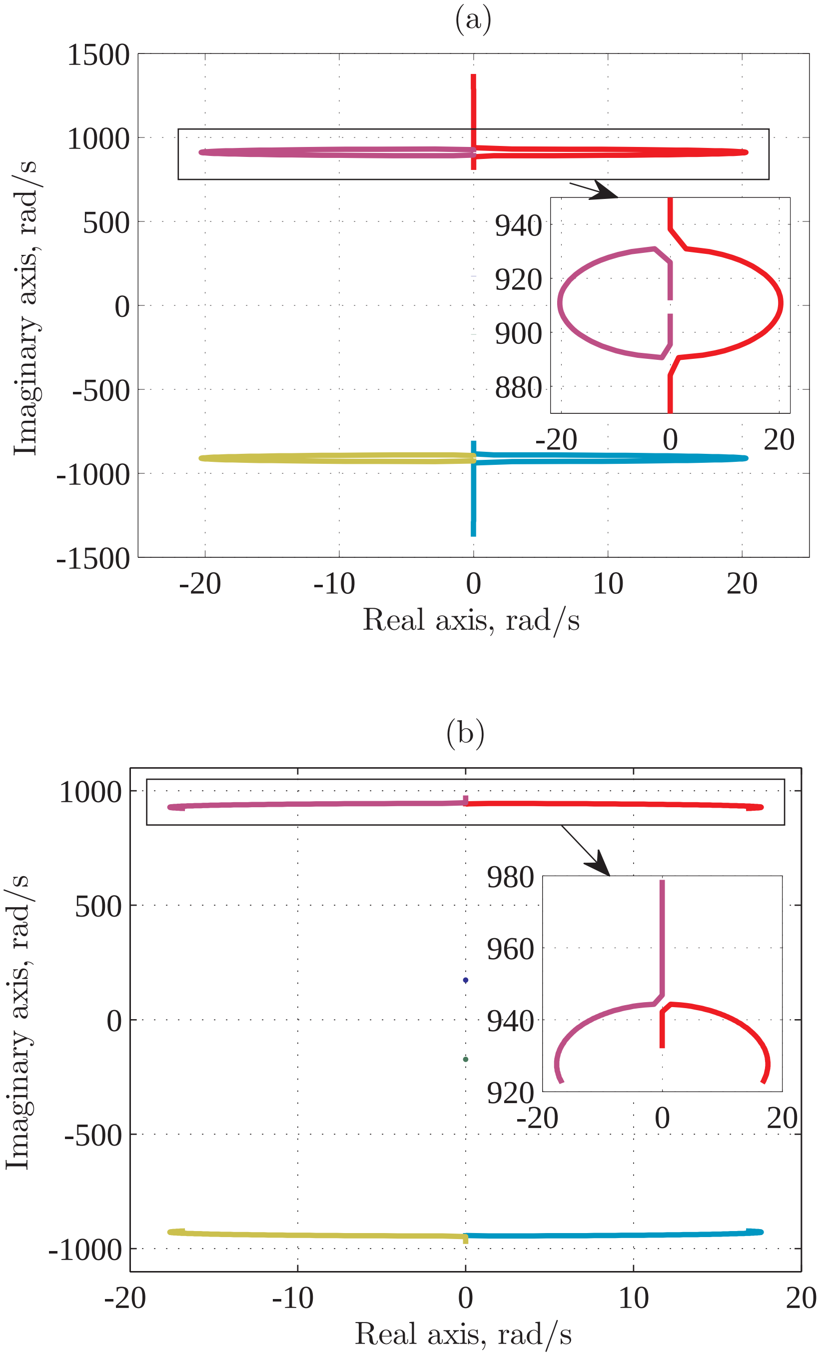

Fig. 4.12: Locus of zeros for $G_{xx}(s)$ with (a) mass variation (m_2) (b) operating point (δ)

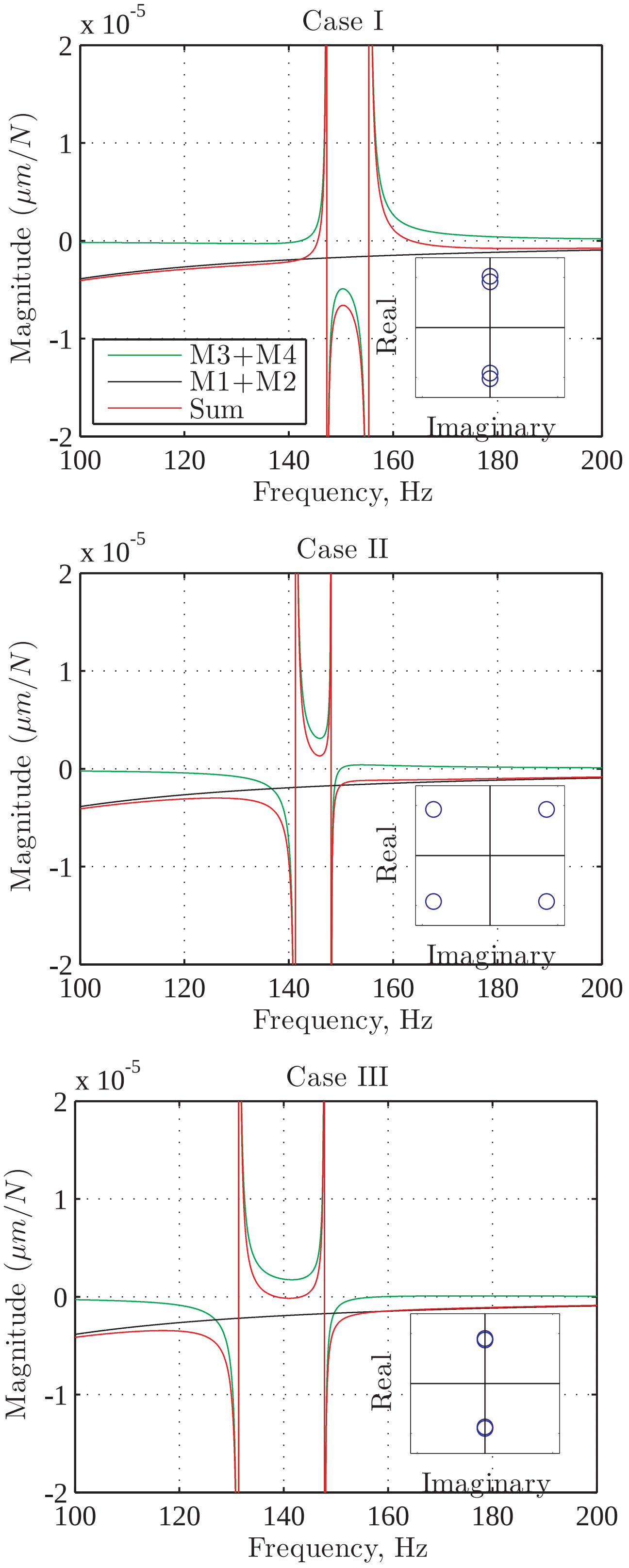

Fig. 4.13: Modal participation factors for transfer function, $G_{xx}(s)$, for cases shown in Table 4.2

damping present is neglected. Near the 150 Hz frequency range, the primary contribution to the transfer function comes from the terms corresponding to the third and the forth modes. In comparison, the contribution of the first two modes, with natural frequencies much below 150 Hz, remains small. These contributions, as well as their sum, are plotted for the three cases considered above in Fig. 4.13. The frequencies at which the sum equals zero are the corresponding zero frequencies of the transfer function $G_{xx}(s)$. When m_2 is lighter by 10% (*Case I*), the sum crosses zero values before and after the two natural frequencies. This leads to two minimum phase zero pairs on the left of the imaginary axis (shown in inset). In case of m_2 being heavier by 10% (*Case II*), sum never crosses zero. However, this case leads to complex-conjugate zero pairs on either side of the imaginary axis. If the mass asymmetry is further increased to 40% (*Case III*), the intersection points move inside the two natural frequencies, again leading to minimum phase zero pairs on the left of the imaginary axis.

4.5 Dynamic model of the XY flexure mechanism

In this section, the assumptions and modeling procedure described in the Section 4.4 are extended to the entire XY mechanism shown in Fig. 4.1. As shown in Fig. 4.14, there are 13 rigid stages in the model, each having 2 DoFs, and 16 PFMs, each providing one kinematic constraint. Therefore, the resulting model can be described by 10 DoFs. A constant force ($\bar{F}$) is applied to displace the motion stage to the operating point $(0, \bar{Y}_1)$ and the transfer function from the X actuation force ($\hat{P}$) to the displacement of the motion stage along the X direction ($\hat{X}_1$) is sought. All the eight secondary stage masses, as well as the operating point, were randomly varied to study the variation in the transfer function via simulation. As observed before in the 4 DoF model, it was found that the transfer function zeros around 150 Hz are highly sensitive to these parameter variations. Although no particular trend was observed, the variation seen in the transfer function could be broadly classified

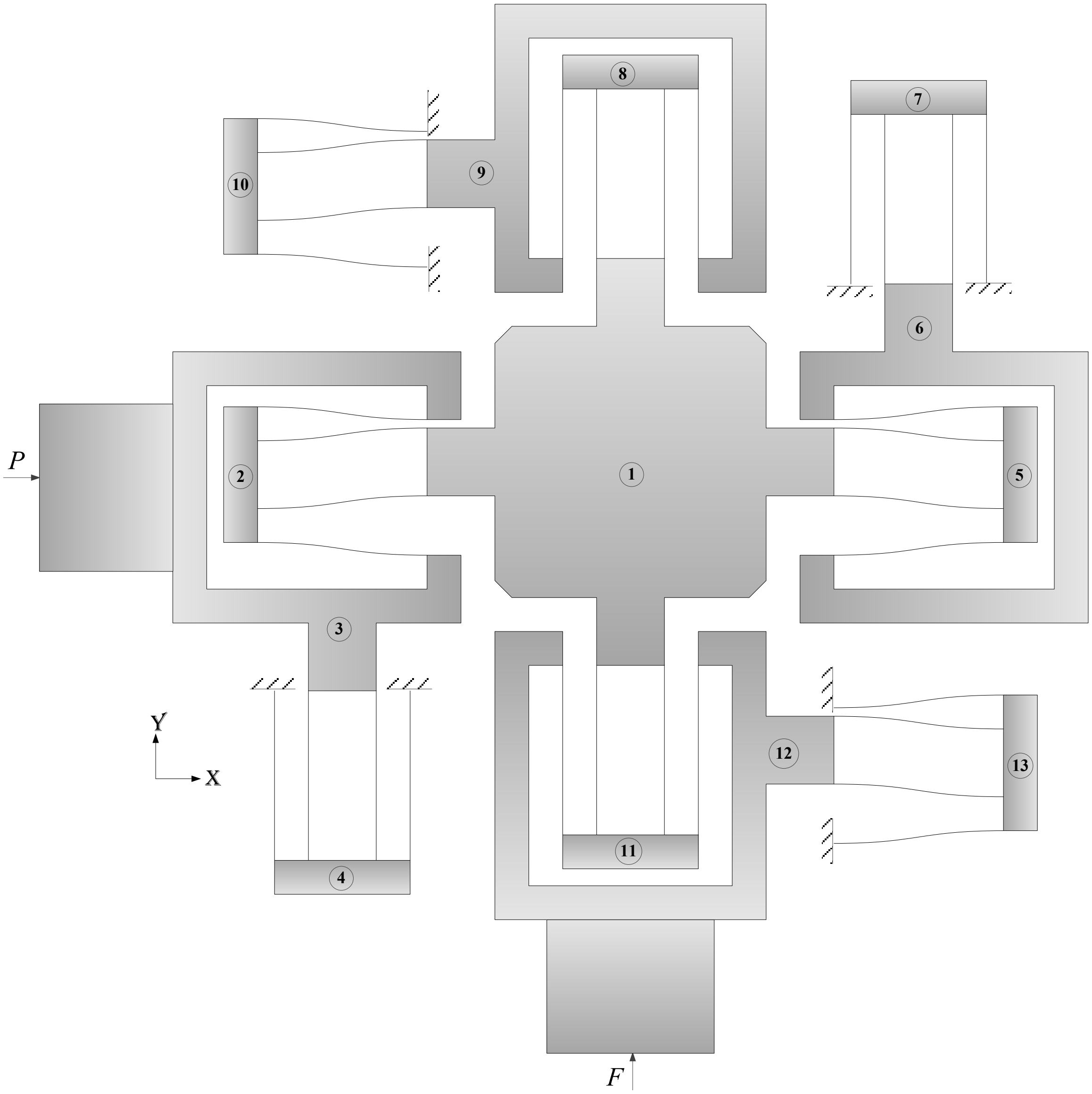

Fig. 4.14: XY Mechanism

Table 4.3: Parameter values for Fig. 4.15

Case	$\bar{Y}_1$ **mm**	**% deviation in mass** m_2	m_4	m_5	m_7	m_8	m_{10}	m_{11}	m_{13}	**NMP zero pairs**
I	1.99	-0.79	0.31	-0.01	0.56	0.43	0.81	0.78	-0.33	0
II	1.68	0.07	-0.78	0.65	-0.32	-0.41	0.49	-0.98	-0.90	1
III	-1.04	-0.77	0.63	-0.35	-0.51	-0.31	-0.25	0.09	0.12	2

in three categories, according to the number of NMP zeros observed. These cases are shown in Fig. 4.15 and the corresponding parameters are tabulated in Table 4.3. The simulations corroborate the experimental frequency response observed in Fig. 4.2. It should be noted that, in addition to asymmetry in masses, dimensional tolerances on the beams will also introduce small asymmetries in the stiffness of PFMs, which in turn could lead to NMP complex-conjugate zeros.

While small asymmetry in mass as well as stiffness is always expected in practice, intentional use of large asymmetry in the design could be employed to overcome the occurrence of NMP zeros. One such experimental result is shown in Fig. 4.16. In this experiment, additional weight was added to increase the mass m_2 in the XY mechanism by 30%. It is intuitive to add additional weight on m_2, as this is the only secondary stage between the actuator and the sensor locations. With this modification, all the zeros in the frequency response of $G_{xx}(s)$ remain minimum phase throughout the operating points along the Y axis.

4.6 Closure

The main contribution of this chapter is to show that the coupling between closely spaced resonances may conspire to produce complex-conjugate nonminimum phase zeros in mechanical structures. In the modeling of the XY flexure mechanism, the kinematic coupling arises due to beam geometric nonlinearities that cannot be neglected in case of beams undergoing large deformations. Additionally, the small asymmetries in the modal parameters (mass and stiffness) result in closely-spaced resonances.

In the future, such modeling efforts would in turn pave the way for structural optimization or modification of mechanisms in the design phase itself to avoid the NMP phenomenon and thereby ensure improved control system performance. For example, in this chapter, intentional use of large asymmetry is shown to overcome the problem of nonminimum phase zeros. Another approach worth exploring would

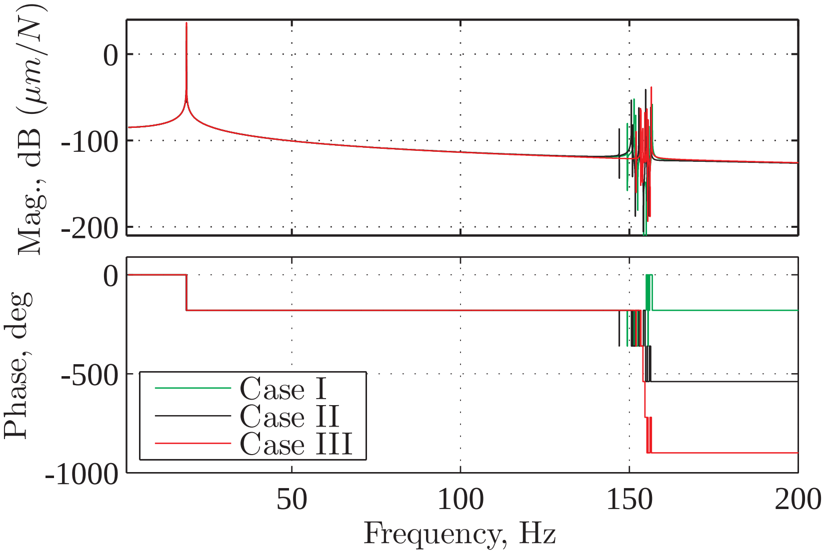

Fig. 4.15: Variation in transfer function, $G_{xx}(s)$, for XY mechanism

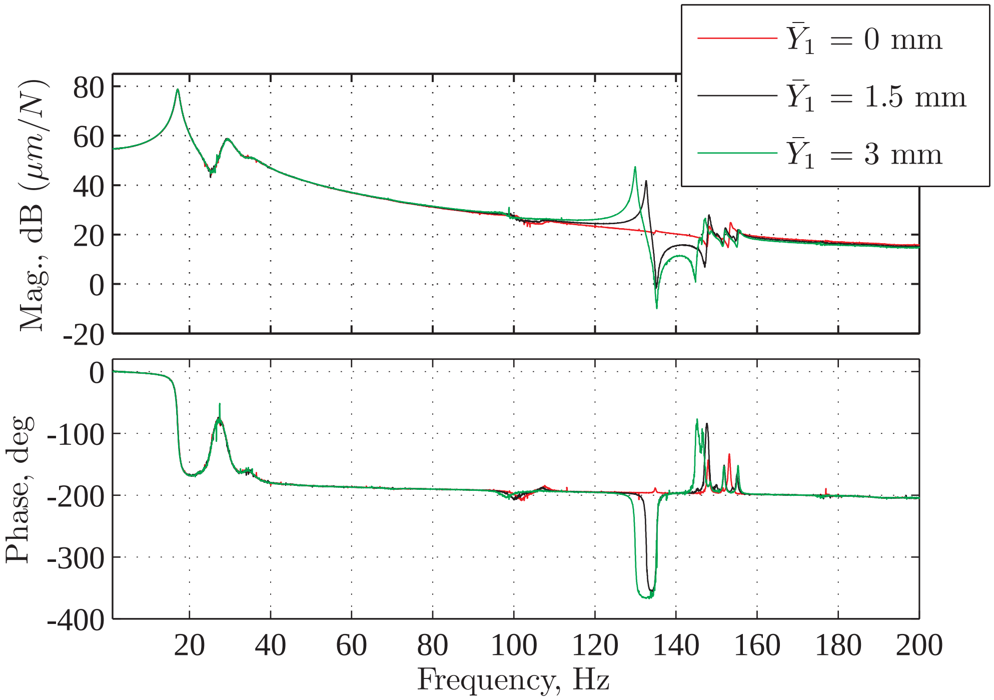

Fig. 4.16: Variation in transfer function, $G_{xx}(s)$, with intentional use of asymmetry

be to exactly constrain the secondary stages inside the DPFM [134]. This is because the modes near 150 Hz in the XY mechanism are related to the transverse vibration of these secondary stages, which are underconstrained in the current design. Lastly, effect of passive damping on complex-conjugate nonminimum phase zeros needs to be explored. For example, by coupling the flexure blades with a low wave-speed medium such as foam, a relatively high degree of damping can be introduced in most of the modes of the mechanism [135]. Fig. 4.17 shows a picture of the XY nanopositioning system with flexure blades bonded with EAR C–301 energy absorbing foam. The frequency response of the system along the X axis, $G_{xx}(s)$, is plotted for the undamped and damped cases in Fig. 4.18. While damping is substantially increased at almost all the poles and zeros, it is also interesting to note that the nonminimum phase behavior, that is observed in the undamped case for operating points with Y coordinate more than 1.5 mm, is not seen when the flexure is damped with foam. The damped XY mechanism remains minimum phase throughout the operating range of motion. However, the passive damping employed also resulted in increased stiffness by a factor of 2, thereby necessitating a correspondingly high actuation force. Therefore, a more systematic study is needed to intelligently couple the beams with foam instead of the *ad hoc* damping experiment shown in Fig. 4.17.

An interesting but unanswered aspect remains the physical explanation of complex-conjugate nonminimum phase zeros in mechanical structures. Mechanism II, described in Section 4.4.3, is one of the simplest structures that is found to exhibit this phenomenon. A study of the energy transfer between modes at the nonminimum phase zero frequency in this mechanism could be a good starting point in this regard.

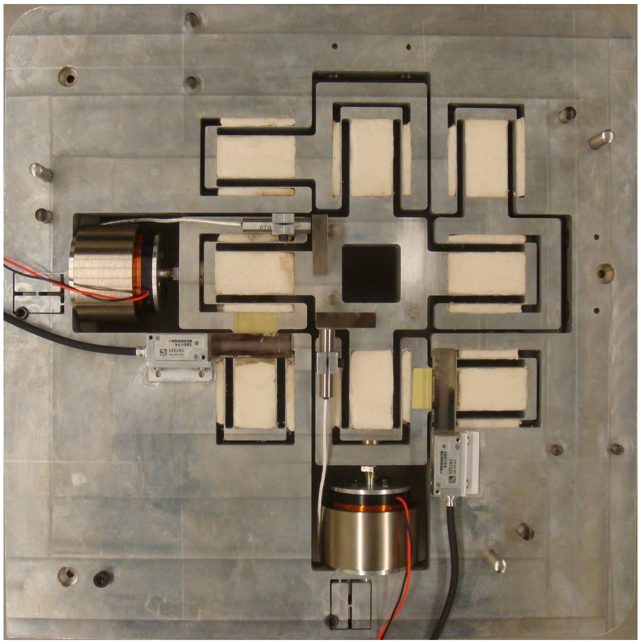

Fig. 4.17: Foam-based passive damping

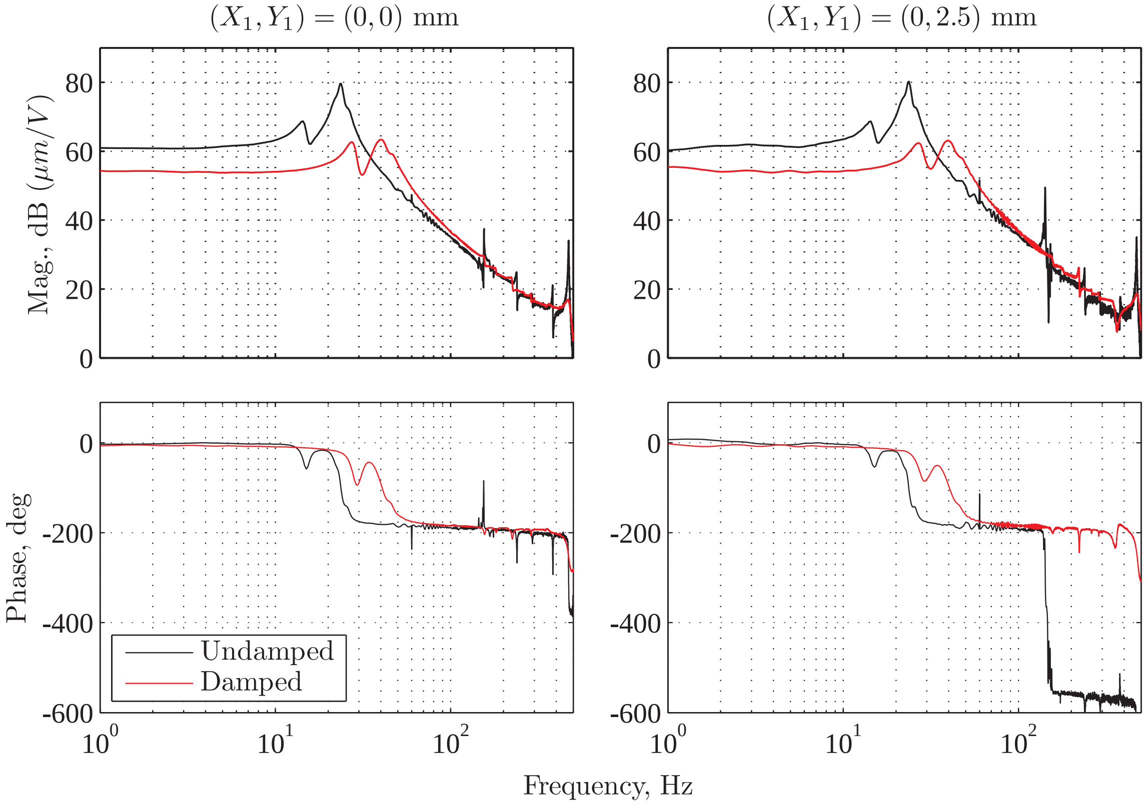

Fig. 4.18: Effect of foam-based damping on the open-loop frequency response along X axis

CHAPTER V

Control System Design for XY Nanopositioning System

In this chapter, the control system design and resulting positioning performance of a large range flexure-based XY nanopositioning system is presented. In addition to motion range, the performance of a nanopositioning system is specified in terms of its motion precision, accuracy, and resolution, along with speed of operation. In a closed-loop setup, these specifications can be translated to equivalent control system design objectives. Accuracy and precision depend on command tracking as well as low frequency disturbance rejection. Positioning noise and the minimum incremental motion determine the resolution. While positioning noise depends on high frequency noise and disturbance rejection, minimum incremental motion is determined by command tracking. Closed-loop bandwidth determines the speed and response time of the nanopositioning system. Finally, closed-loop robustness against modeling uncertainties and parameter variations affect all of the above.

5.1 Control System Challenges

In the context of the XY nanopositioning system described in Chapter IV, several control design challenges and trade-offs are identified in achieving the abovementioned performance objectives:

1. Most existing nanopositioning systems have a high first natural frequency because they operate over a relatively small motion range. Therefore, simple lower-order integral controllers with loop crossover frequency far less than the first resonance provide good overall performance [3]. In our case, an extended range of motion leads to low primary stiffness, resulting in a low first natural frequency ($\sim$18 Hz). In order to achieve a bandwidth greater than this first natural frequency, a higher-order controller is needed, which poses greater performance trade-offs in terms of actuation effort, robustness, and noise and disturbance rejection.

2. In general, lightly-damped poles and zeros in a flexible system severely affect the closed loop stability and performance [136]. In addition to this, the non-collocation of the sensor and the actuator places additional limitations on the achievable bandwidth [130].

3. As discussed in Chapter IV, small asymmetry and kinematic coupling results in parameter variation in the frequency response along each axis over the operating motion range of the nanopositioning system. This includes not only the small variations in pole and zero frequencies, but also a change in the zero dynamics from minimum phase to nonminimum phase. The latter poses greater challenges and puts hard limitations to obtaining robust stability and performance, especially near frequencies where nonminimum phase zeros appear [111, 112]. Additionally, static and dynamic cross-axis coupling between the two axes, defined as the motion along one axis due to actuation along the other axis, also degrades the positioning performance. This cross-axis coupling can be either linear or non-linear, depending on its source.

4. Various sources of noise and disturbance limit the achievable positioning noise. This includes feedback sensor noise, actuator driver noise and harmonic distortion,

electronic noise in the data acquisition hardware, and mechanical floor vibrations. The individual contribution of these sources to the positioning noise depends upon their respective magnitude, where they enter the feedback system, the control architecture, and the controller design (See Fig. 3.3).

5. In additional to the challenges that are specific to this XY system, any closed-loop framework, in general, is subject to fundamental limitations and trade-offs [111, 137]. One such trade-off, between disturbance rejection and stability robustness in the case of low open-loop bandwidth, is discussed in further detail later in this chapter.

5.2 Feedback Design and Implementation

Having identified various control system objectives, challenges, and limitations, the goal of this section is to evaluate the performance of a classical controller on the XY nanopositioning system. The system can be thought of as a 2-input 2-output dynamical system with the voltage signals to the current drivers as inputs ($\hat{u}_x$ and $\hat{u}_y$) and the corresponding displacement of the motion stage ($\hat{x}_1$ and $\hat{y}_1$) along the X and Y directions as outputs. This would result in four transfer functions, as shown below.

$$\begin{Bmatrix} \hat{x}_1 \\ \hat{y}_1 \end{Bmatrix} = \begin{bmatrix} G_{xx} & G_{xy} \\ G_{yx} & G_{yy} \end{bmatrix} \begin{Bmatrix} \hat{u}_x \\ \hat{u}_y \end{Bmatrix} \tag{5.1}$$

It is important to note that all the transfer functions vary with the operating point of the motion stage in the XY plane, i.e., $G_{ij} \equiv G_{ij}(\bar{X}_1, \bar{Y}_1)$, where $i,\ j \in x,\ y$. Here, we make a few observations. First, after the design modification employed in the previous chapter, the transfer function $G_{xx}(s)$ and $G_{yy}(s)$ remain minimum phase throughout the operating range. The parameter variation, in terms of the variation of pole and zero frequencies, remains small and manageable. The variation in transfer

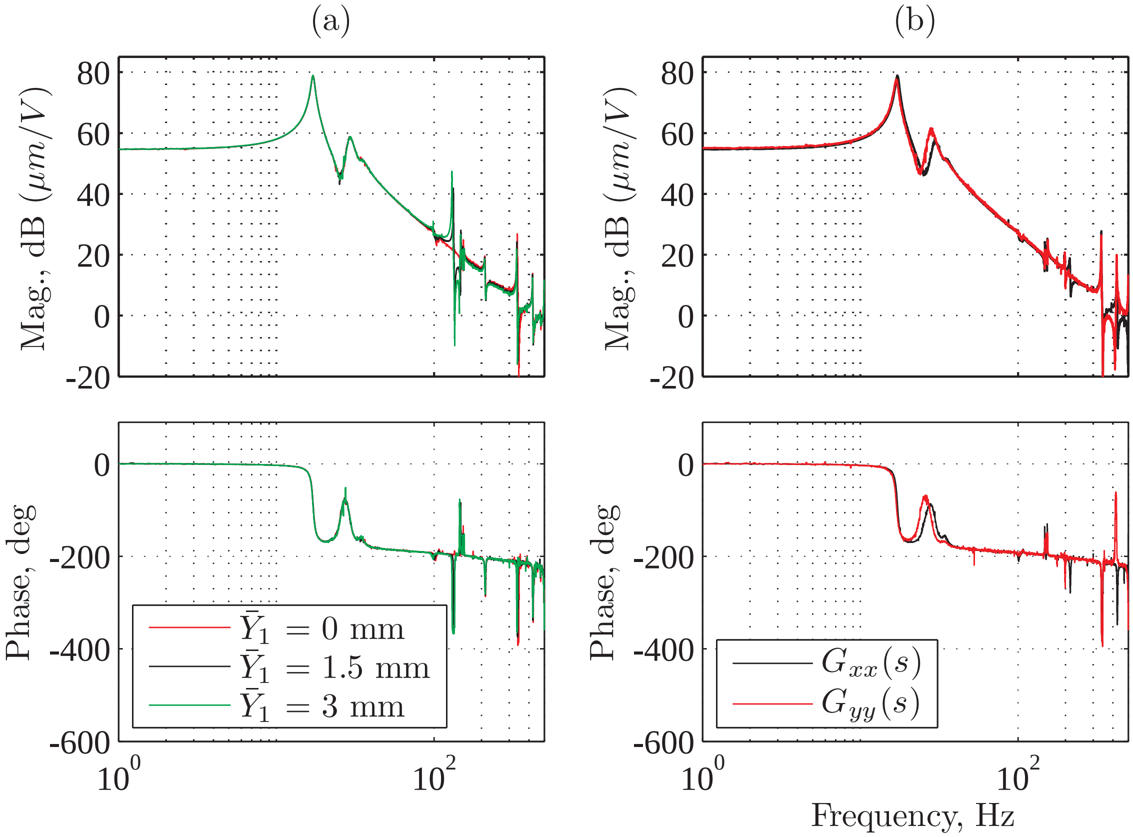

Fig. 5.1: Experimentally measured frequency responses for the XY nanopositioning system. (a) Parameter variation in $G_{xx}(s)$ after design modification with operating point $(\bar{X}_1, \bar{Y}_1) = (0, \bar{Y}_1)$ mm. (b) Comparison between transfer function along X axis and Y axis at the nominal operating point $(\bar{X}_1, \bar{Y}_1) = (0, 0)$ mm

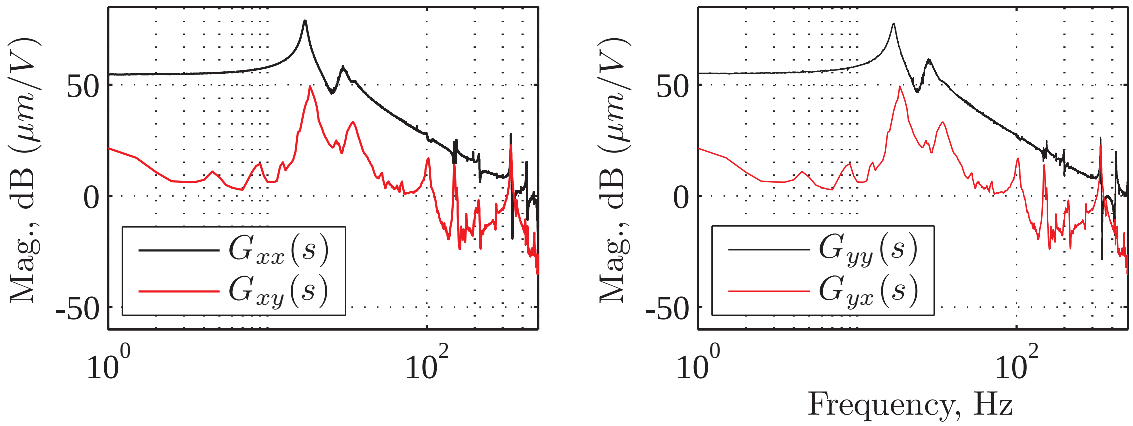

Fig. 5.2: Comparison of the cross-axis transfer functions with the transfer functions along the two axes

function $G_{xx}(s)$ is shown in Fig. 5.1(a). Second, as seen in Fig. 5.1(b), there is a good match between the transfer functions along both the axes up to 400 Hz, due to the symmetry in the setup. After 400 Hz, a pole-zero pair is reversed. And third, the cross-axis transfer functions, $G_{xy}(s)$ and $G_{yx}(s)$, are more than 50 times smaller than the transfer functions along the two axes, at frequencies below 100 Hz, as seen in Fig. 5.2. The cross-axis coupling between the two axes in this frequency range can be treated as an output disturbance from the perspective of each individual axis. Next, the linear controller design along the Y axis, for the plant transfer function $G_{yy}(s)$ at the nominal operating point $(0, 0)$ mm, is presented. An identical controller is implemented along the X axis as well.

The Matlab™ function *invfreqs* [104] was used to fit a continuous-time stable transfer function, $G_{yy}(s)$, to the open-loop frequency response along the Y axis at the nominal operating point $(0, 0)$ mm. The resulting 11$^{\text{th}}$ order transfer function is given by

$$\begin{aligned} G_{yy}(s) = {} & \frac{-8.38 \times 10^6}{(s^2 + 5.77s + 1.164 \times 10^4)} \frac{(s^2 + 21.12s + 2.28 \times 10^4)}{(s^2 + 24.43s + 3.14 \times 10^4)} \\ & \times \frac{(s^2 + 11.27s + 1.58 \times 10^6)}{(s^2 + 17.50s + 1.54 \times 10^6)} \frac{(s^2 + 3.25s + 4.72 \times 10^6)}{(s^2 + 6.99s + 4.49 \times 10^6)} \\ & \times \frac{(s^2 + 20.72s + 6.71 \times 10^6)}{(s^2 + 14.76s + 7.04 \times 10^6)} \frac{(s - 7500)}{(s + 7500)} \end{aligned} \tag{5.2}$$

A comparison between the analytical transfer function and the experimentally obtained frequency response in shown in Fig. 5.3. The analytical transfer function has a high-frequency nonminimum phase pole-zero pair at around 1.2 kHz to account for the phase loss at high frequencies. The source of this phase loss is not explored. It may be due to the eddy current dynamics of the actuator or due to the structural dynamics of the mechanism itself.

The open-loop plant transfer function is used to design a lag-lead controller,

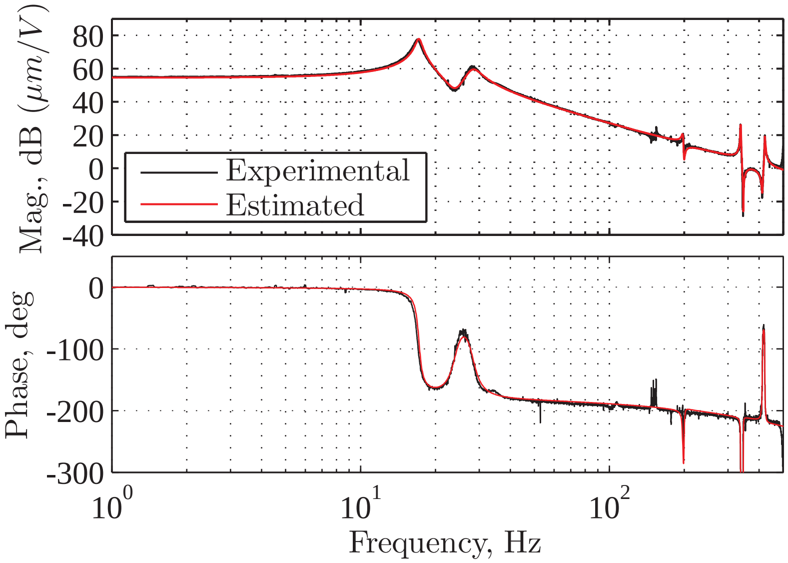

Fig. 5.3: Open-loop plant transfer functions along the Y axis at the nominal operating point $(0, 0)$ mm

$C_{yy}(s)$, to achieve acceptable closed-loop stability and performance. The lag part includes an integrator to achieve zero steady state error and low frequency disturbance rejection, and the lead part is needed to increase the phase near gain crossover frequency. In order to ensure a good roll-off at higher frequencies, an additional pole is added after the crossover frequency. The following feedback controller was finally implemented:

$$C_{yy}(s) = \frac{260(s+100)^2}{s(s+2000)(s+3000)} \tag{5.3}$$

The experimentally measured frequency response of the resulting loop transfer function $L_{yy}(s) = G_{yy}(s)C_{yy}(s)$ along with corresponding stability margins is shown in Fig. 5.4. This confirms a Gain Margin (GM) or 12.9 dB and a Phase Margin (PM) of 37.2° at a gain crossover frequency of approximately 70 Hz. Fig. 5.5 shows the experimentally obtained frequency response of the closed-loop transfer function along Y axis from the command $\hat{r}_y$ to $\hat{y}_1$. The dip in gain and phase seen at lower frequencies is due to the zeros of the $C_{yy}(s)$.

From the perspective of each axis and its respective independent controller, the

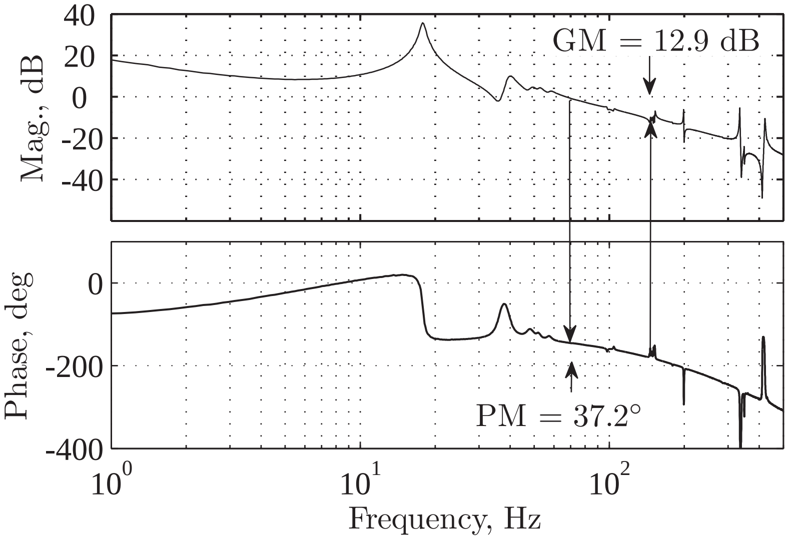

Fig. 5.4: Experimentally measured frequency response of the loop transfer function along Y axis, $L_{yy}(s)$

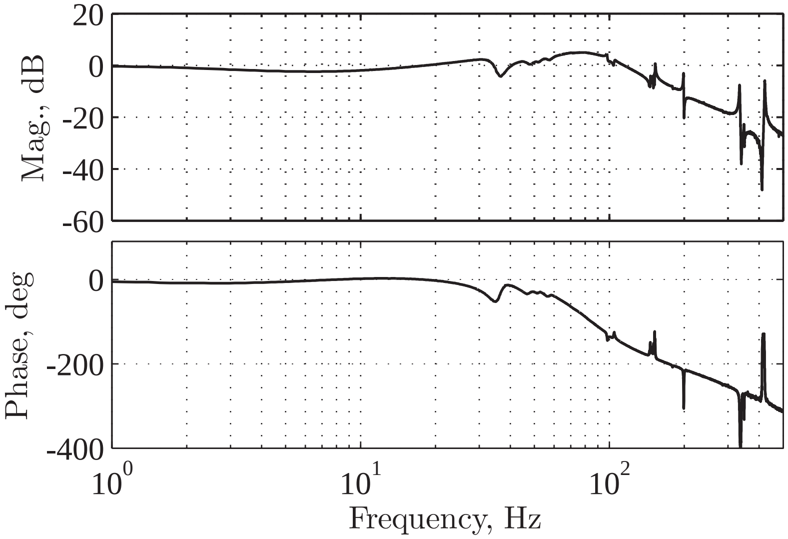

Fig. 5.5: Experimentally measured frequency response of the closed-loop transfer function along Y axis, $T_{yy}(s)$

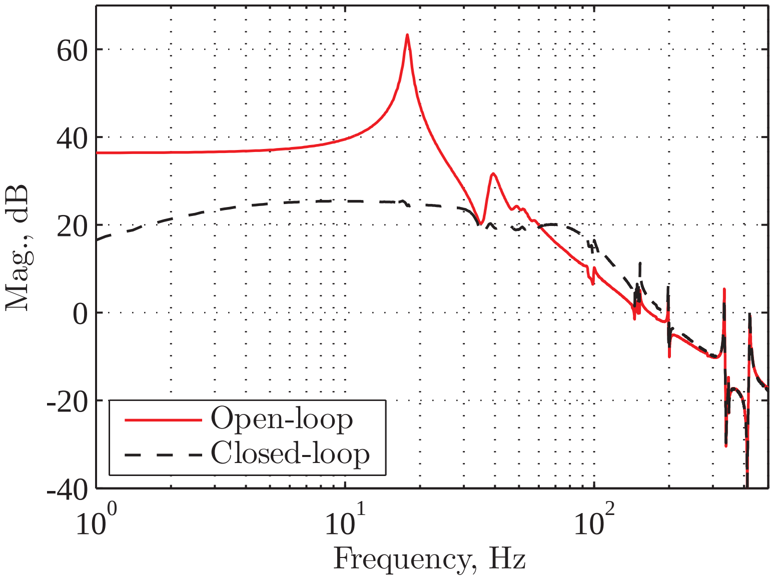

Fig. 5.6: Input disturbance rejection achieved by linear feedback

amplifier noise and distortion serve as input disturbance, while the cross-axis coupling and the ground vibration can be thought of as output disturbances. Therefore, it is important to consider the effect of the feedback controller in rejecting these disturbances. The closed-loop transfer functions from the input disturbance d_i and the output disturbance d_o to the motion stage displacement along the Y axis, $\hat{y}_1$, are given by:

$$T_{d_i \to \hat{y}_1}(s) = \frac{G_{yy}(s)}{1 + G_{yy}(s)C_{yy}(s)} \tag{5.4}$$

$$T_{d_o \to \hat{y}_1}(s) = \frac{1}{1 + G_{yy}(s)C_{yy}(s)} \tag{5.5}$$

It is clear that the ability of the feedback system to reject both the disturbances depends upon the magnitude of $C_{yy}(s)$. In other words, higher closed-loop bandwidth, which requires a high control gain over a certain frequency range, ensures improved disturbance rejection. However, there is obviously a limit to which controller gain can be increased due to concerns arising from stability margins and sensor noise amplification. For the controller $C_{yy}(s)$ given in Eq. (5.3), Fig. 5.6 shows the compar-

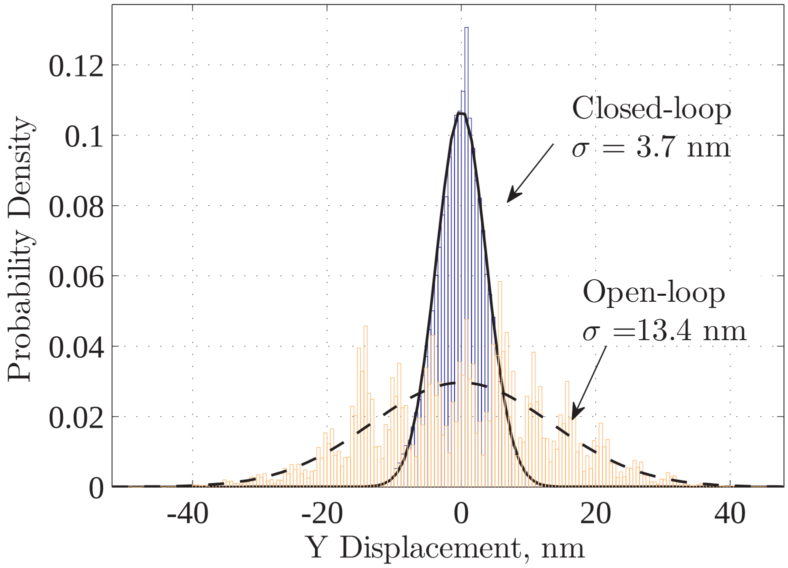

Fig. 5.7: Amplitude distribution of the open-loop and closed-loop positioning noise

ison between the open-loop and closed-loop transfer functions from d_i to $\hat{y}_1$, $G_{yy}(s)$ and $T_{d_i \to \hat{y}_1}(s)$, respectively. Thus, the improvement in input disturbance rejection is clearly evident. A similar trend exists for the output disturbance rejection.

Next, the positioning performance for the XY nanopositioning system based on the controller design are presented. To measure the positioning noise, which is also representative of the resolution, the stage was commanded to stay at a fixed position. In steady-state, the current amplifier harmonics and cross-axis coupling are absent and the amplifier's broad-band Gaussian noise is the dominant contributor to positioning noise. The effect of this input disturbance on $\hat{y}_1$ is directly proportional to the area under the transfer function $T_{d_i \to \hat{y}_1}(s)$ in Fig. 5.6 [138]. This area is approximately 4 times less than the area under the transfer function $G_{yy}(s)$, which indicates a corresponding improvement in input disturbance rejection. Indeed, this is corroborated by the time domain analysis of positioning noise in Fig. 5.7, which shows the probability density function of the open-loop and closed-loop positioning noise of $\hat{y}_1$. The closed-loop positioning noise is approximately 4 nm RMS, which is

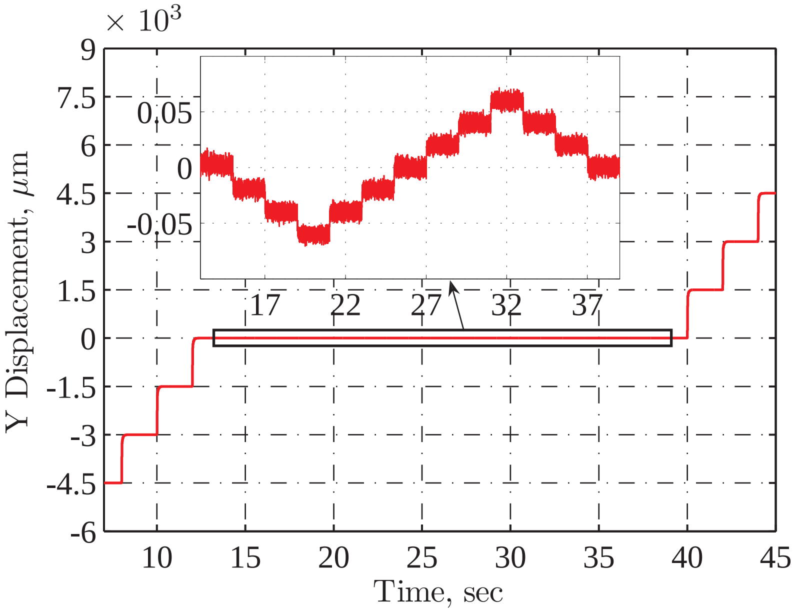

Fig. 5.8: Motion stage position response for 1.5 mm steps and 20 nm steps along Y axis

3.6 times better than that measured in the open-loop.

Fig. 5.8 shows the position response of the motion stage to step commands of size 1.5 mm and 20 nm (inset) along the Y axis, over a 9 mm range. The steady-state positioning resolution as seen in this time-domain plot is under 4 nm RMS, in agreement with Fig. 5.7. Similar closed-loop positioning resolution, in point-to-point motion commands, was measured for the X axis actuation, as well as simultaneous X and Y axis actuation. Because of the absence of friction and backlash, the figure (inset) also indicates a positioning repeatability or precision on the order of the positioning resolution.

Next, the motion stage was commanded to move in a 5 mm diameter circle at 1 Hz. This was done by sending sinusoidal reference commands along both axes with a magnitude of 2.5 mm and separated in phase by 90°. The measured trajectory along with the ideal commanded circle is plotted in Fig. 5.9. For better visualization, the radial deviation from the ideal circle is magnified 25 times. The RMS of the radial error between the measured trajectory and the ideal circle is approximately 2.9 μm.

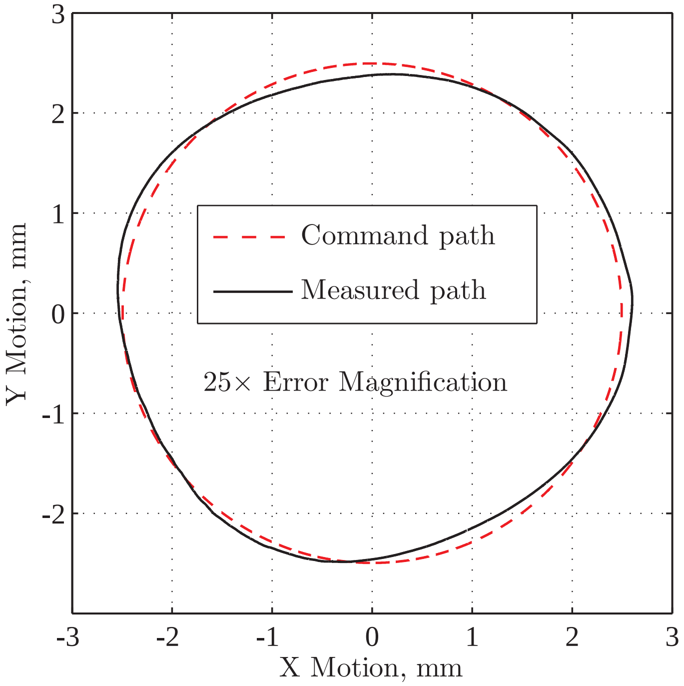

Fig. 5.9: Motion stage tracking a 5 mm diameter circle

Corresponding RMS errors for the same diameter circle tracking at frequencies 0.1 Hz and 0.01 Hz were also measured and found to be 319 nm and 58 nm, respectively. A power spectrum analysis of these closed-loop tracking errors at various frequencies reveals the presence of three components: 1. Magnitude and phase errors in the actual motion profile along each axis with respect to the sine and cosine commands, 2. Higher order harmonics of the commanded frequency and 3. Broad-band Gaussian noise. The magnitude and phase error is due to lack of adequate closed-loop command following. The higher order harmonics in the measured trajectory arise from inadequate attenuation of the nonlinearities in the actuator and its driver as well as the cross-axis coupling (i.e., lack of input and output disturbance rejection). The broad-band positioning noise is largely due to the corresponding broad-band noise in the current amplifier. The circle tracking performance at lower frequencies is better, as noted above, due to relatively better command following and disturbance rejection provided by the feedback controller at these frequencies. However, achieving better command tracking and disturbance rejection at higher frequencies via linear feedback controllers results in tradeoffs with stability margins and sensor noise rejection. Thus, large range and nanometric motion quality is achieved in point-to-point positioning but not in dynamic command tracking, even at low frequencies.

For periodic commands, the deterministic part of the tracking error due to the nonlinearities and lack of command following is relatively large compared to the stochastic part due to various sources of noise and disturbances. Therefore, in a manner similar to the control of the single-axis nanopositioning system presented in Chapter III, independent iterative learning controllers can to be implemented in conjunction with the feedback along each axis to reduce the repeating part of the tracking error.

5.3 Iterative Learning Controller

In this section, the design and performance of the iterative learning controller (ILC) along the Y axis is presented. The control architecture remains similar to that shown earlier in Fig. 3.10. A similar arrangement is repeated along the X axis as well. The closed-loop transfer function $T_{yy}(s)$, shown in Fig. 5.5, encounters gain and phase errors even in the low frequency range after 30 Hz. To compensate for this error, the learning controller could be designed to be a constant gain (λ) times the inverse of the closed-loop transfer function. Since the transfer function has a high frequency non-minimum phase zero, a stable inverse is designed via the zero-phase error tracking controller (ZPETC) algorithm [139]. The resulting learning controller is given below:

$$L_{yy}(z) = \lambda \frac{1535.9(z-0.4464)(z-0.4806)(z-0.6805)(z-0.9172)}{z^2(z+0.1676)(z-0.99)} \times \frac{(z-0.9949)(z+0.4727)(z^2-1.997z+0.997)(z^2-1.959z+0.9604)}{(z-0.9901)(z^2-1.997z+0.9971)} \tag{5.6}$$

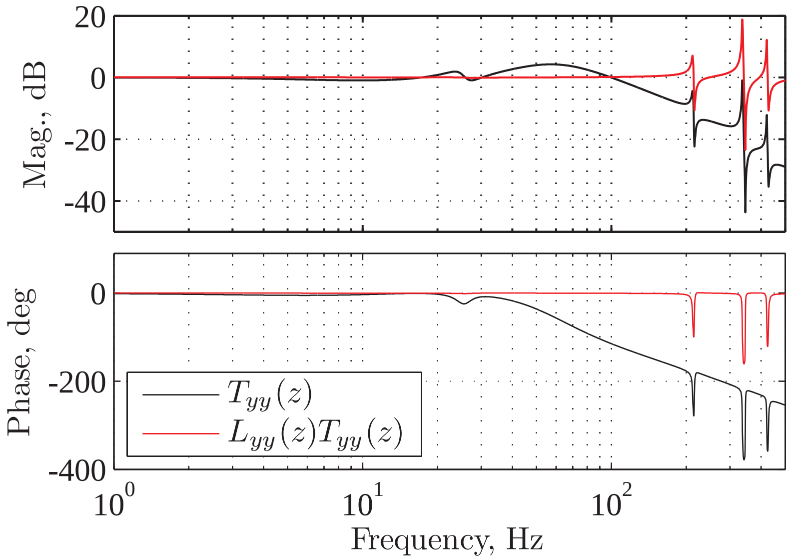

Fig. 5.10: Closed-loop transfer function with and without non-causal zero-phase learning controller

Note that $L_{yy}(z)$ has more zeros than poles and therefore is a non-causal compensator. However, as mentioned before, its offline implementation is not an issue because the ILC computations are performed retrospectively. For example, if $L_{yy}(z)$ has m number of excess zeros, then the classical ILC update law given in Eq. (3.9) can be modified according to the following equation:

$$u_{j+1}(k) = Q(z)[u_j(k) + z^{-m}L(z)e_j(k+m)] \tag{5.7}$$

Figure 5.10 shows the comparison between the discrete-time closed-loop transfer function, $T_{yy}(z)$ with and without the learning controller. The gain and phase of the compensated transfer function remains close to 0 dB and 0°, respectively, up to 200 Hz. The high frequency pole-zero pairs after 200 Hz are not compensated. The robustness filter $Q(z)$ is designed as a low-pass 7^{th} order Butterworth filter with a bandwidth ω_n of 200 Hz to ensure monotonic convergence as well as stability. Figure 5.11 shows the Nyquist plot of $Q(z)(1 - L(z)T(z))$ for values of $\lambda = 0.5$ and $\omega_n = \infty$, 200 Hz. With 200 Hz Q filter bandwidth, the plot remains within the unit

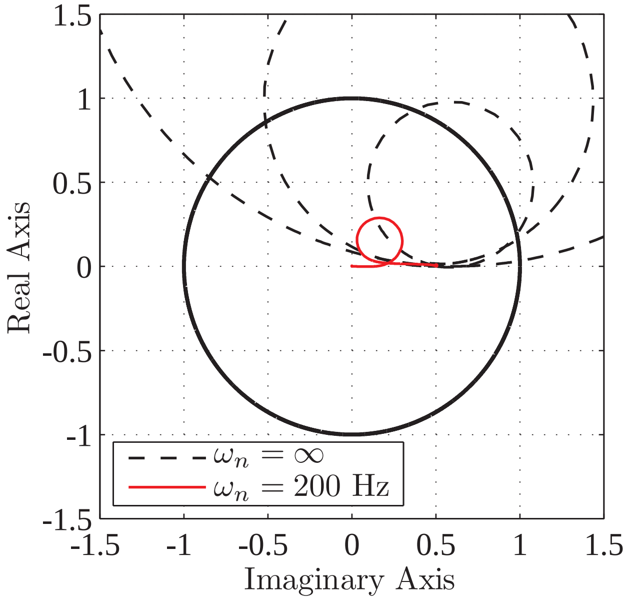

Fig. 5.11: Nyquist plot for $Q_{yy}(z)(1-\lambda L_{yy}(z)T_{yy}(z))$ showing monotonic convergence criterion

circle over the entire frequency range with the maximum value of $|Q(z)(1-L(z)T(z))|$ being 0.5, thus satisfying the stability criterion mentioned in Eq. (3.10).

The combined feedback and ILC controller described above was implemented along the Y axis of the XY nanopositioning system. Figure. 5.12 shows the resulting tracking performance for a 1 mm amplitude (i.e., 2 mm peak-to-peak), 1 Hz sinusoidal command. Figure 5.12(a) shows the decrease in the tracking error as a function of the iteration number. The RMS of the tracking error is reduced from about 7.8 µm to 15.8 nm in approximately 70 iterations. This corresponds to a reduction by a factor of about 500. The tracking errors before the application of ILC and at the end of the 70th iteration are plotted in Fig. 5.12(b). The performance improvement, compared to the linear feedback control by itself, comes from a reduction in the repeating portion of the tracking error at the command frequency and its harmonics (see Fig. 5.12(c)).

The final tracking error is still 4 times larger than that obtained in a position hold experiment. This is also reflected in the comparison of the power spectrum of the tracking error for 1 mm, 2 Hz sinusoidal command and zero command, shown

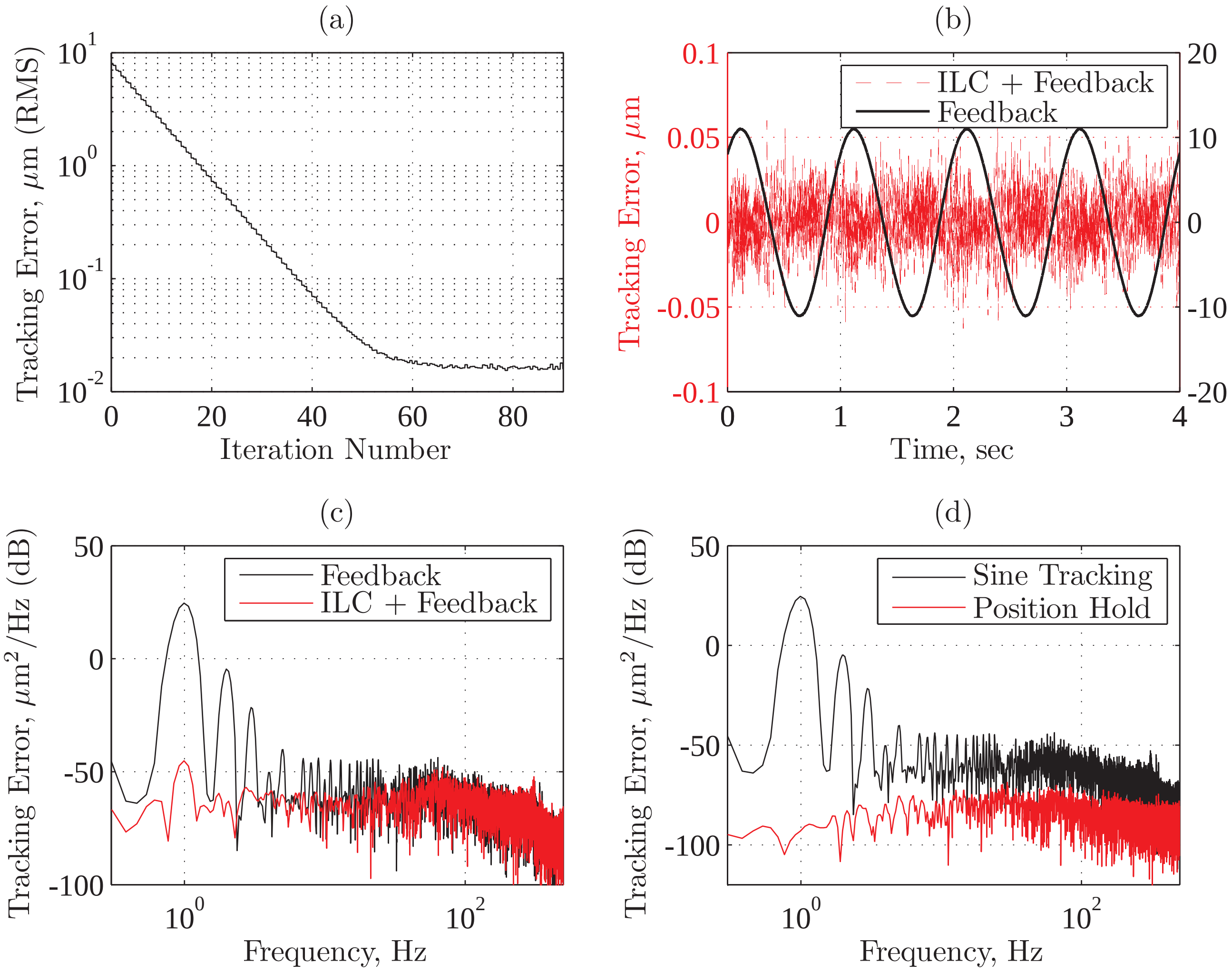

Fig. 5.12: Tracking performance with combined feedback and ILC along Y axis: (a) Tracking error convergence (b) Tracking error with and without ILC (c) and (d) Power spectrum of the tracking error

Table 5.1: Comparison of the radial tracking error (in nm RMS) obtained for circle tracking experiments

	2 mm, 1 Hz	3 mm, 1 Hz	2 mm, 2 Hz
Feedback Only	184	845	379
Feedback + ILC	18	22	20

in Fig. 5.12(d). The noise floor in the sinusoidal tracking experiment is much larger leading to an increased final tracking error. Also, it was observed that the noise floor increases with increasing the amplitude of the command signal. This behavior may be a result of the increase in electrical noise in the current amplifier or the power supply with increasing electrical power, but the actual cause remains to be investigated.

5.4 Circle Tracking Experiments

The performance of the combined ILC and feedback controller was evaluated for the motion stage tracking a circular command. This was done by sending equal amplitude sinusoidal reference commands along both the axes separated in phase by 90°. The measured trajectory before and after the application of ILC, along with the commanded circle, is plotted in Fig. 5.13. For better visualization, the contour error (radial deviation from the ideal circle) is magnified. The RMS of the contour error for three separate experiments are mentioned in Table 5.1. With ILC, the RMS of the contour error is reduced by a factor of 10 to 40.

5.5 Closure

In this chapter, the potential and capability of a flexure-based XY nanopositioning system in simultaneously achieving large range and high motion quality is demonstrated experimentally. It is shown that by modifying the dynamics of the accompanying XY flexure mechanism, feedback and iterative learning controllers de-

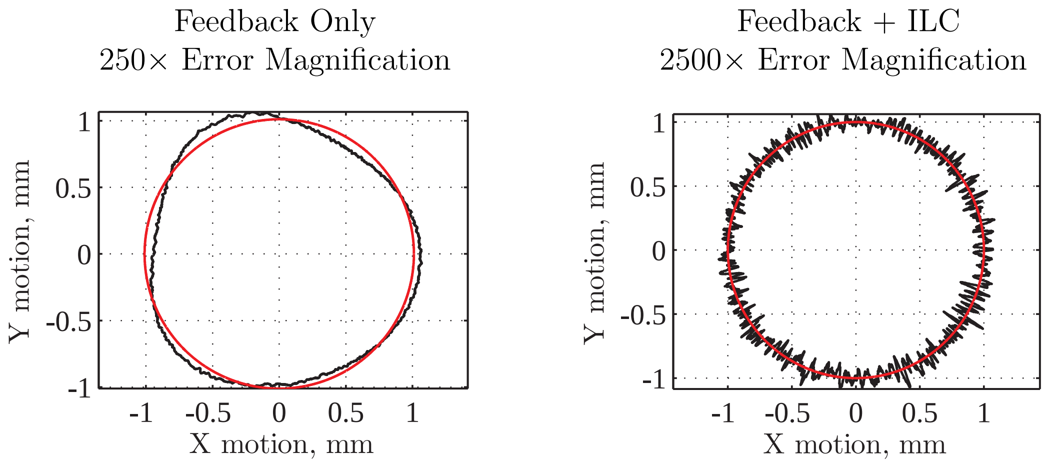
Feedback Only
250× Error Magnification

Feedback + ILC
2500× Error Magnification

2 mm Diameter, 1 Hz

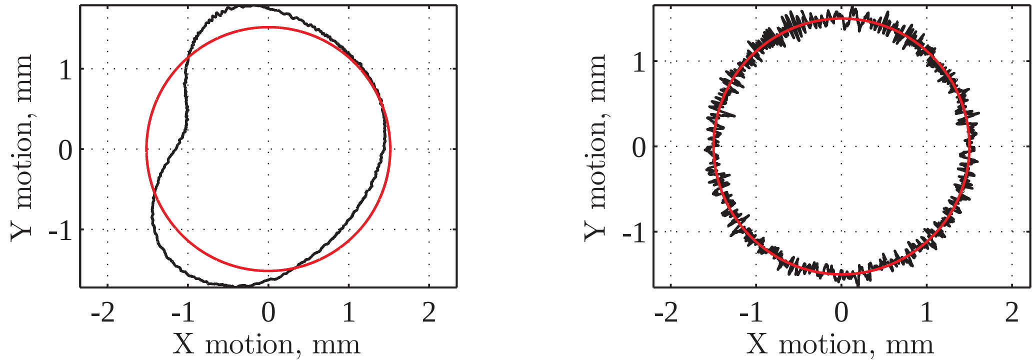

3 mm Diameter, 1 Hz

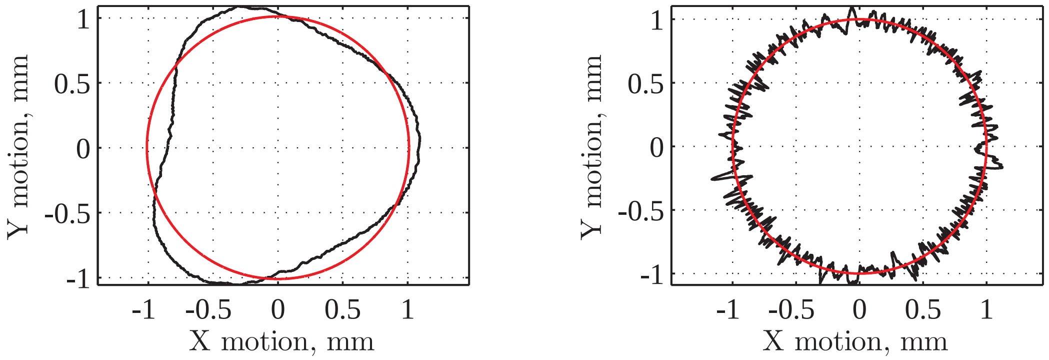

2 mm Diameter, 2 Hz

Fig. 5.13: Radial tracking error for circle tracking experiments: (—) Command path, (—) Measured Path

signed for the nominal operating point can be applied over a large operating range of motion, without robustness issues.

Further reduction in the tracking error could be achieved by reducing the noise and disturbance at the sources by using better hardware, as mentioned in Section 1.7. Additionally, incorporation of passive damping needs to be investigated. By coupling the flexure blades with a low wave-speed medium such as foam, relatively high degree of damping can be introduced over a wide frequency range, without being affected by the variation in pole and zero frequencies [135]. Damping of lightly-damped high-frequency poles in the flexure mechanism will ease the trade-off between the achievable closed-loop stability and disturbance rejection, and thereby lead to an improvement in the closed-loop bandwidth and positioning performance. In order to achieve a higher closed-loop bandwidth, it will also be necessary to take into account the cross-coupling transfer functions. A MIMO feedback controller design should be pursued in this regard [140].

Moving forward, a cross-coupling controller [141] may be applied in addition to the existing controllers. The control objective of the cross-coupling controller is to reduce the contour error (tracking error perpendicular to the command trajectory), rather than focusing on reducing the tracking error along individual axis. This will be especially useful in case of trajectories that involve sharp turns, where the tracking error will have high-frequency components beyond the bandwidth of the feedback loop. In such cases, independent ILCs will not be able to completely eliminate the tracking error along each axis. The cross-coupling controller can also be applied within the framework of iterative learning controller, resulting in a cross-coupled iterative learning control (CCILC) system [142]. In a manner similar to ILC, CCILC helps reduce the repeating portion of the contour tracking error in case of periodic command trajectories.

APPENDICES

APPENDIX A

Iterative Learning Controller Implementation in Simulink™

In this appendix, the implementation procedure for the combined feedback control and iterative learning control (ILC) on the single-axis nanopositioning system, described in Chapter III, is presented. The code was developed in Simulink™ and deployed real-time via dSPACE DS1103 microcontroller. A snapshot of the code is shown in Fig. A.1. The input to the code is the position signal from the linear optical encoder and the output command is the voltage signal to the servoamplifier. The feedback loop runs at a fixed loop-rate of 10 kHz. Within every repetition of the command period, the tracking error is stored in a form of an array using the *Buffer* block. The ILC input is computed based on these arrays and is applied as an additional input to the feedback loop in the subsequent cycles using the *Unbuffer* block.

The ILC computations are performed, once per command period, inside the *Matlab Function* block via the script shown below:

```
%% Define function inputs and outputs
function [unewfilt,RMS] = fcn(enew,Lgain,Ldelay)

%% Define global variables
global earray uarray evec uvec;

%% Initialize variables
evec = [earray(3,:) earray(2,:) earray(1,:)];
uvec = [uarray(3,:) uarray(2,:) uarray(1,:)];

%% Implement learning function
unewvec = uvec + Lgain*circshift(evec',-ceil(Ldelay))';

%% Implement Q-filter
Qnum = 1e-6*[0.29,2.03,6.11,10.19,10.19,6.11,2.03,0.29];
Qden = [1,-5.87,14.85,-20.97,17.84,-9.15,2.61,-0.32];
unewfiltvec = filtfilt(Qnum,Qden,unewvec);
unewfilt = unewfiltvec(10001:20000)';

%% Update variable histories
uarray = circshift(uarray,1);
uarray(1,:) = unewfilt';
earray = circshift(earray,1);
earray(1,:) = enew;

%% Compute RMS error
RMS = 20*log10(norm(enew)/sqrt(length(enew)));
```

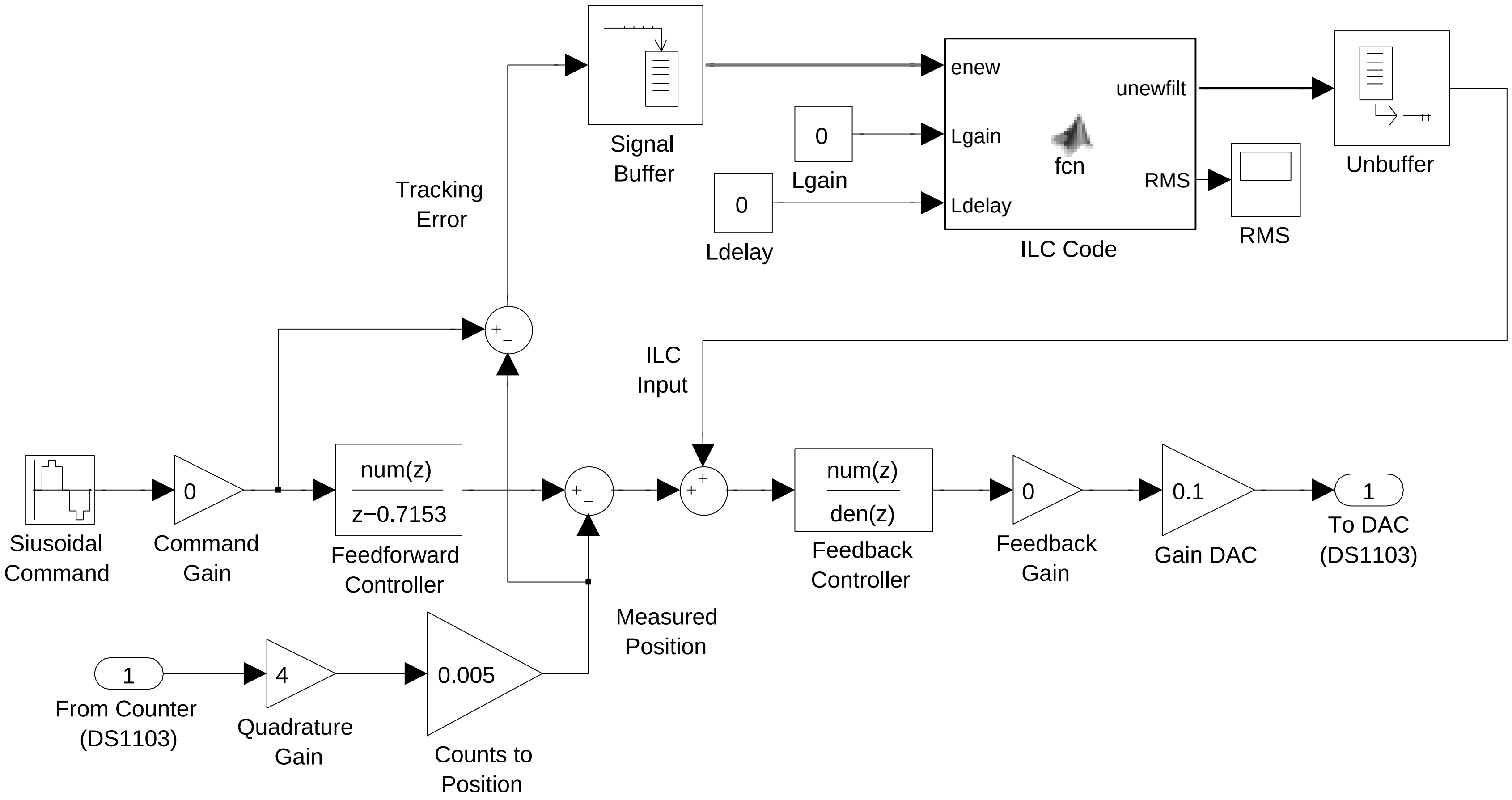

Fig. A.1: Simulink™ model for ILC implementation

APPENDIX B

Servoamplifier Design and Characterization

Introduction

Servoamplifiers are used to drive electromagnetic actuators by providing control over either coil current or voltage. They are generally classified into the following two categories: Pulse-width-modulated (PWM) servoamplifiers and linear servoamplifiers. PWM servoamplifiers regulate the power through the actuator coil via on-off switching of a constant voltage, at a very high frequency of about 10 kHz or higher. While PWM amplifiers are widely used due to their high efficiency ($> 90\%$) and low cost, they suffer from high-frequency noise as well as *dead-band* near zero crossing. The high-frequency noise leads to unwanted velocity ripples, which degrade the position stability. Also, the dead-band near zero causes increased dynamic errors during direction reversals [143, 144]. Linear amplifiers, in contrast to their PWM counterparts, vary the power in the coil proportionally to the input command. Therefore, they have a relatively higher linearity near zero as well as lower noise. However, they are not very efficient ($< 50\%$) and are expensive as compared to the PWM servoamplifiers. In low-power high-precision positioning applications, therefore, linear servoamplifiers prove to be a better choice.

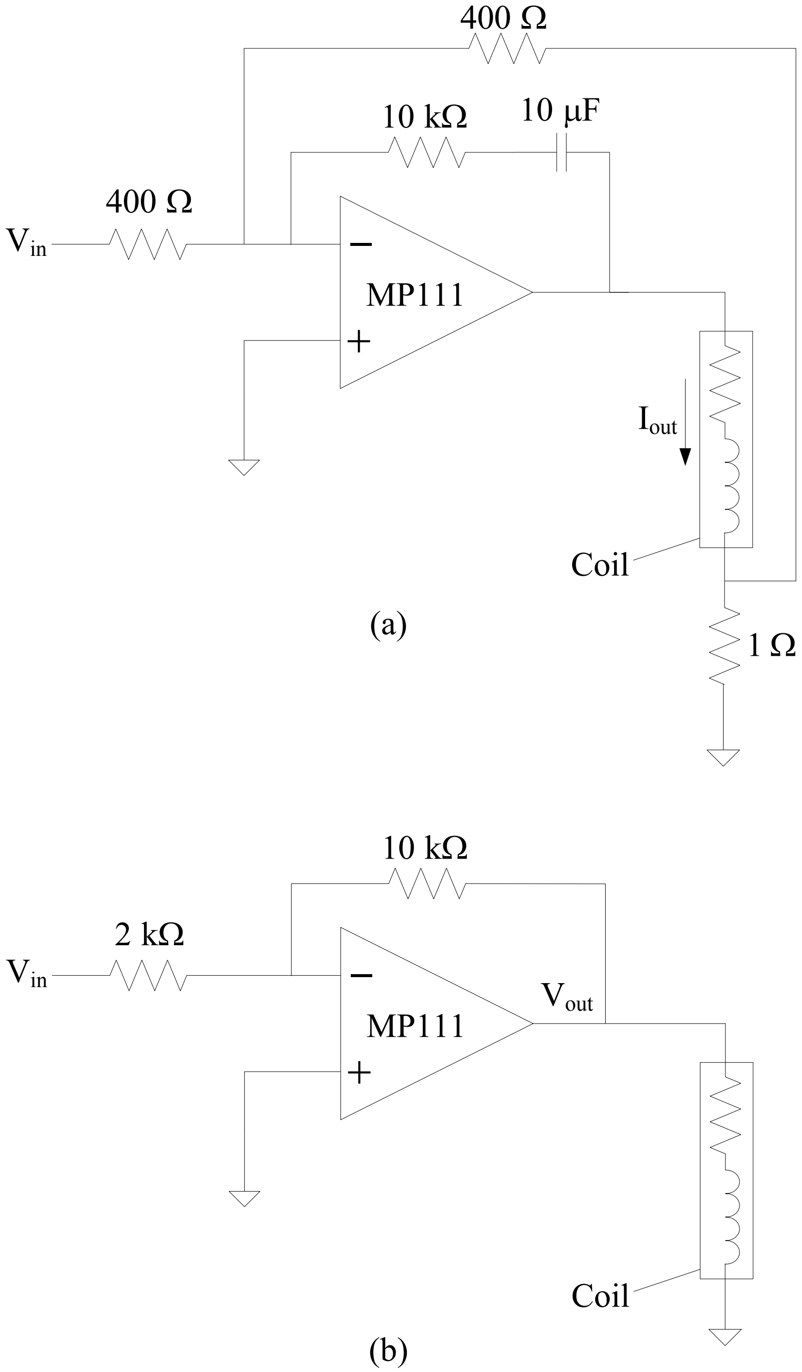

Fig. B.1: Circuit diagram for the servoamplifier operating in (a) Current mode (b) Voltage mode

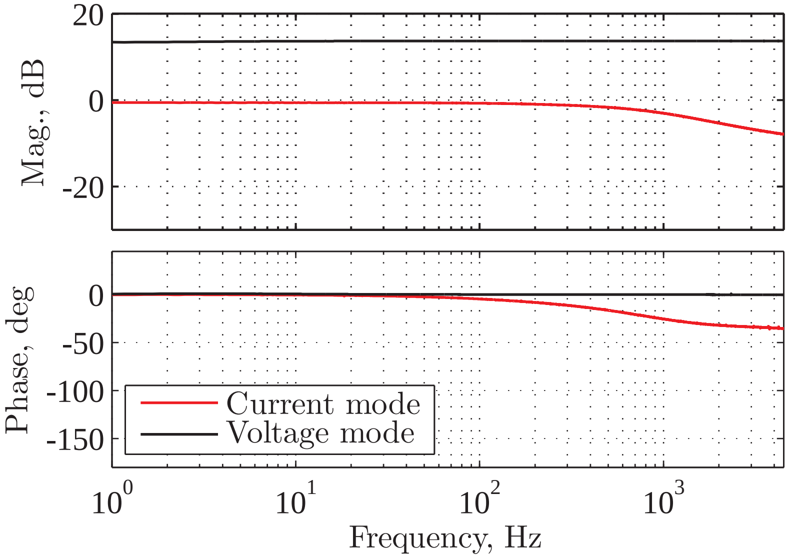

Fig. B.2: Frequency response of the servoamplifier operating in current mode [A/V] and voltage mode [V/V]

Servoamplifier Design

After considering several off-the-shelf linear servoamplifiers, which proved to be inadequate in their noise and distortion characteristics, a custom-built linear servoamplifier using was designed. This amplifier consists of a low-noise power Op-Amp (MP111) from Apex Microtechnology, which was chosen due to its high current capability and 10 μV RMS output noise at 1 MHz bandwidth. The servoamplifier was assembled using an evaluation board (EK57) from the same vendor. As shown in Fig. B.1, the servoamplifier is designed to be operated in both current mode as well as voltage mode. For the current mode, an inverting voltage-controlled-current-source circuit in a floating load configuration is used [145]. The gain and the bandwidth of the amplifier were set to be –1 A/V and 1 kHz, respectively. The bandwidth is set well above the frequency range of motion control. For the voltage mode, the Op-Amp is operated in an inverting feedback configuration, with gain of –5 V/V and bandwidth of about 10 kHz. The experimentally measured input-output frequency response of the servoamplifiers is shown in Fig. B.2.

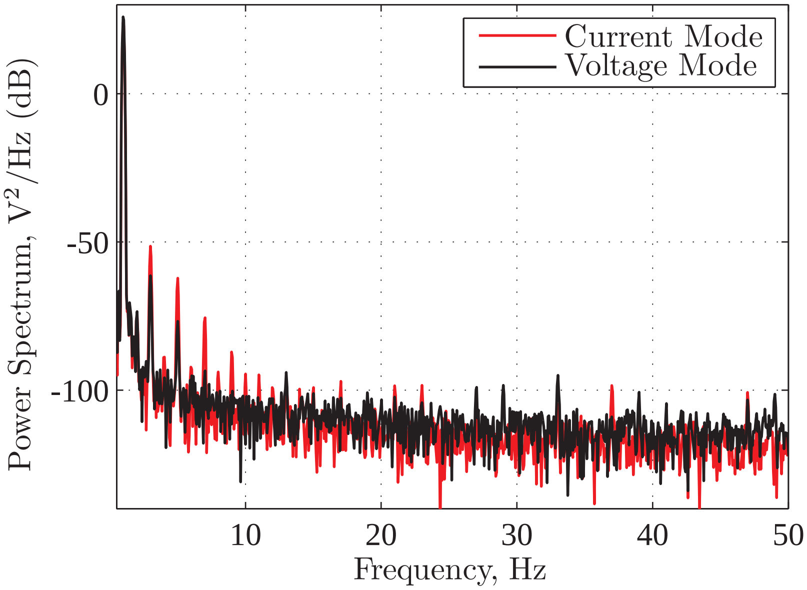

Fig. B.3: Power spectrum of the servoamplifier voltage output in current mode and voltage mode

Servoamplifier Characterization

The noise and distortion in the servoamplifier directly impacts the positioning resolution and dynamic command tracking, respectively. In order to measure these performance specifications, a 1 Hz sinusoidal command was applied as input. The magnitude of the command was varied to set the voltage across the 2.2Ω, 2.05 mH coil to be 19 V peal-to-peak. For this experiment, NI PXI–4461 from National Instruments was used for data-acquisition. It consists of 24–bit ADCs and DACs with a high dynamic range of 118 dB. The power spectrum of the output voltage, for both the current mode and the voltage mode operation, is shown in Fig. B.3. Based on this figure, the signal-to-noise ratio (SNR[1]) for both cases was estimated to be about 110 dB, corresponding to a value of 20 μV RMS in the time-domain. However, the

---

[1] SNR is the ratio of the RMS amplitude of the signal to the RMS amplitude of the noise which is not harmonic distortion [146].

total harmonic distortion (THD[2]) up to 50 Hz was found to be slightly higher in the current mode (–76 dB) than in the voltage mode (–87 dB). It should be noted that THD generally gets worse with increasing command amplitude or command frequency.

In the current mode, the servoamplifier circuit incorporates a current feedback loop. The current feedback loop not only compensates for the coil inductance dynamics but also overcomes the effect of back–EMF in the coil. Since the actuator force is proportional to coil current, the frequency response from the servoamplifier command to the actuator force can be approximated by a constant gain up to the bandwidth of the servoamplifier, which is typically at least 10 times higher than the bandwidth of the overall position control loop. In contrast, when operated in the voltage mode, the back-EMF dynamics produces additional damping in the fundamental mode. Secondly, the coil inductance leads to an additional pole with the corresponding phase lag in the overall open-loop frequency response of the motion system. However, this effect can be mitigated by placing an additional lead-pair in the position feedback loop. In this thesis, both the current mode and the voltage mode servoamplifiers are used. Positioning results for the single-axis nanopositioning system, presented in Chapter III, are based on the voltage mode servoamplifier. For the experiments on the XY nanopositioning system in Chapter V, the servoamplifier was operated in the current mode. Although the current mode servoamplifier has more distortion than the voltage mode, the noise level in both the modes of operation are the same. Hence, with the application of combined feedback and iterative learning control in the position control loop, similar positioning performance was obtained irrespective of the mode of operation.

---

[2] THD is the ratio between the root-sum-of-squares of all the harmonic distortion components that can be distinguished from the noise floor and the RMS value of the component at the input frequency [146].

BIBLIOGRAPHY

BIBLIOGRAPHY

[1] Slocum, A. H., 1992. *Precision machine design.* Society of Manufacturing Engineers.

[2] Parmar, G., 2012. "Performance specifications of nanopositioning systems: accuracy, precision, and resolution". Master's thesis, University of Michigan, Ann Arbor, MI.

[3] Devasia, S., Eleftheriou, E., and Moheimani, S. O. R., 2007. "A survey of control issues in nanopositioning". *IEEE Transactions on Control Systems Technology,* **15**(5), pp. 802–23.

[4] O'Brien, W., 2005. Long range motion with nanometric precision. Tech. note, Mad City Labs. [Web Link].

[5] Magonov, S. N., and Whangbo, M.-H., 1996. *Surface analysis with STM and AFM: experimental and theoretical aspects of image analysis.* VCH, Weinheim, New York.

[6] Hyongsok T. Soh, Kathryn Wilder Guarini, C. F. Q., 2001. *Scanning probe lithography.* Lkluwer Academic Publishers.

[7] Taniguchi, N., 1974. "On the basic concept of nanotechnology". In Proceedings of International Conference on Performance Engineering, Vol. 2, pp. 18–23.

[8] Fukada, S., and Nishimura, K., 2007. "Nanometric positioning over a one-millimeter stroke using a flexure guide and electromagnetic linear motor". *International Journal of Precision Engineering and Manufacturing,* **8**(2), pp. 49–53.

[9] Hubbard, N. B., Culpepper, M. L., and Howell, L. L., 2006. "Actuators for micropositioners and nanopositioners". *Applied Mechanics Reviews,* **59**(6), pp. 324–334.

[10] Zhelyaskov, V., Broderick, M., Raphalovitz, A., and Davies, B., 2006. "Automated piezoelectric nanopositioning systems – long travel ranges and accurate angular movement create new opportunities in biomedical manipulation systems". *IEEE Circuits and Devices Magazine,* **22**(6), pp. 75–78.

[11] Hennessey, B., C. D., and Fuller, D., 2004. "Positioning systems make submicron-level moves". *Photonics Spectra,* **38**.

[12] Sun, L. N., Jie, D. G., Liu, Y. J., Chen, Z. C., and Cai, H. G., 2006. "Investigation on a novel dual-grating macro-micro driven high speed precision positioning system for nems". 1st IEEE International Conference on Nano/Micro Engineered and Molecular Systems, pp. 644–648.

[13] Vorndran, S., 2004. "Nanopositioning: fighting the myths". *Opto & Laser Europe,* **122**, pp. 25–7.

[14] *Product Model # P-542.2.* Physik Instrumente. [Web Link].

[15] *Product Model # PXY100.* Piezosystems Jena. [Web Link].

[16] *Product Model # NTS10.* Discovery Technology International. [Web Link].

[17] *Product Model # NPXY100C.* nPoint Inc. [Web Link].

[18] *Product Model # Nano-LR200.* Mad City Labs. [Web Link].

[19] *Product Model # NPS-XY-100A.* Queensgate Instruments. [Web Link].

[20] *Product Model # ANT95-25-XY-PLUS.* Aerotech Inc. [Web Link].

[21] *Product Model # P-629.2.* Physik Instrumente. [Web Link].

[22] Minne, S. C., Adams, J. D., Yaralioglu, G., Manalis, S. R., Atalar, A., and Quate, C. F., 1998. "Centimeter scale atomic force microscope imaging and lithography". *Applied Physics Letters,* **73**(12), pp. 1742–1744.

[23] Lenhert, S., Sun, P., Wang, Y., Fuchs, H., and Mirkin, C. A., 2007. "Massively parallel dip-pen nanolithography of heterogeneous supported phospholipid multilayer patterns". *Small,* **3**(1).

[24] Haaheim, J., and Nafday, O. A., 2008. "Dip pen nanolithography: A "Desktop Nanofab™" approach using high-throughput flexible nanopatterning". *Scanning,* **30**(2), pp. 137–150.

[25] Analyzing large surfaces using afm stitching. Tech. note, NanoSurf. [Web Link].

[26] Van de Moosdijk, M., Van den Brink, E., Simon, K., Friz, A., Phillipps, G., Travers, R., and Raaymakers, E., 2002. "Collinearity and stitching performance on an ASML stepper". Proceedings of SPIE – Internatinal Society of Optical Engineers, pp. 858–66.

[27] Preibisch, S., Saalfeld, S., and Tomancak, P., 2009. "Globally optimal stitching of tiled 3D microscopic image acquisitions". *Bioinformatics,* **25**(11), pp. 1463–1465.

[28] Imre, A., Ocola, L. E., Rich, L., and Klingfus, J., 2010. "Large area direct-write focused ion-beam lithography with a dual-beam microscope". *Journal of Vacuum Science Technology B: Microelectronics and Nanometer Structures,* **28**(2), pp. 304 –309.

[29] Klapetek, P., Valtr, M., and Matula, M., 2011. “A long-range scanning probe microscope for automotive reflector optical quality inspection”. *Measurement Science & Technology,* **22**(9), p. 094011.

[30] Gao, W., 2010. “Large area scanning probe microscope for micro-textured surfaces”. In *Precision Nanometrology*, Springer Series in Advanced Manufacturing. Springer, London, pp. 245–281.

[31] Dai, G. L., Jung, L., Pohlenz, F., Danzebrink, H. U., Kruger-Sehm, R., Hasche, K., and Wilkening, G., 2004. “Measurement of micro-roughness using a metrological large range scanning force microscope”. *Measurement Science & Technology,* **15**(10), pp. 2039–2046.

[32] Dai, G. L., Pohlenz, F., Danzebrink, H. U., Xu, M., Hasche, K., and Wilkening, G., 2004. “Metrological large range scanning probe microscope”. *Review of Scientific Instruments,* **75**(4), pp. 962–969.

[33] Kramar, J. A., 2005. “Nanometre resolution metrology with the molecular measuring machine”. *Measurement Science & Technology,* **16**(11), pp. 2121–2128.

[34] Salaita, K., Wang, Y. H., Fragala, J., Vega, R. A., Liu, C., and Mirkin, C. A., 2006. “Massively parallel dip-pen nanolithography with 55000-pen two-dimensional arrays”. *Angewandte Chemie-International Edition,* **45**(43), pp. 7220–7223.

[35] Large area scans on tablets. Tech. note, Witec Wissenschaftliche Instrumente. [Web Link].

[36] Maeda, G. J., and Sato, K., 2008. “Practical control method for ultra-precision positioning using a ballscrew mechanism”. *Precision Engineering,* **32**(4), pp. 309–18.

[37] Lihua, L., Yingchun, L., Yongfeng, G., and Akira, S., 2010. “Design and testing of a nanometer positioning system”. *Journal of Dynamic Systems, Measurement, and Control,* **132**(2), pp. 021011–6.

[38] Buice, E. S., Otten, D., Yang, R. H., Smith, S. T., Hocken, R. J., and Trumper, D. L., 2009. “Design evaluation of a single-axis precision controlled positioning stage”. *Precision Engineering,* **33**(4), pp. 418–424.

[39] Young-Man, C., Jung Jae, K., Jinwoo, K., and Dae-Gab, G., 2008. “Design and control of a nanoprecision XY scanner”. *Review of Scientific Instruments,* **79**(4), pp. 045109–7.

[40] Zschaeck, S., Amthor, A., and Ament, C., 2011. “Decentralized high precision motion control for nanopositioning and nanomeasuring machines”. 37th Annual Conference on IEEE Industrial Electronics Society, pp. 546–551.

[41] Chassagne, L., Wakim, M., Xu, S., Topcu, S., Ruaux, P., Juncar, P., and Alayli, Y., 2007. "A 2D nano-positioning system with sub-nanometric repeatability over the millimetre displacement range". *Measurement Science and Technology,* **18**(11), pp. 3267–3272.

[42] Michellod, Y., Mullhaupt, P., and Gillet, D., 2006. "Strategy for the control of a dual-stage nano-positioning system with a single metrology". 2006 IEEE Conference on Robotics, Automation and Mechatronics, pp. 1–8.

[43] Kosinskiy, M., Liu, Y., Ahmed, S. I. U., Scherge, M., and Schafer, J. A., 2006. "Tribology of nanopositioning characterization of precision linear bearings on nanometre scale". *VDI Berichte*(1950), pp. 215–224.

[44] Liu, Y., 2010. "Nanopositioning and nanomeasuring system: Friction and its control". In *Advanced Tribology.* Springer Berlin Heidelberg, pp. 592–593.

[45] Fan, K.-C., Fei, Y., Yu, X., Wang, W., and Chen, Y., 2007. "Study of a noncontact type micro-CMM with arch-bridge and nanopositioning stages". *Robotics and Computer-Integrated Manufacturing,* **23**(3), pp. 276–284.

[46] Pritschow, G., 1998. "A comparison of linear and conventional electromechanical dives". *CIRP Annals - Manufacturing Technology,* **47**(2), pp. 541–548.

[47] Kim, W.-J., and Verma, S., 2007. "Multiaxis maglev positioner with nanometer resolution over extended travel range". *Journal of Dynamic Systems, Measurement and Control, Transactions of the ASME,* **129**(6), pp. 777–785.

[48] Holmes, M., Hocken, R., and Trumper, D., 2000. "The long-range scanning stage: a novel platform for scanned-probe microscopy". *Precision Engineering,* **24**(3), pp. 191–209.

[49] Khan, M. U., Bencheikh, N., Prelle, C., Lamarque, F., Beutel, T., and Buttgenbach, S., 2011. "A long stroke electromagnetic XY positioning stage for micro applications". *Mechatronics, IEEE/ASME Transactions on,* **17**(5), pp. 866–875.

[50] Dejima, S., Wei, G., Katakura, K., Kiyono, S., and Tomita, Y., 2005. "Dynamic modeling, controller design and experimental validation of a planar motion stage for precision positioning". *Precision Engineering,* **29**(3), pp. 263–71.

[51] Shinno, H., Hashizume, H., Yoshioka, H., Komatsu, K., Shinshi, T., and Sato, K., 2004. "X-Y-θ nano-positioning table system for a mother machine". *CIRP Annals - Manufacturing Technology,* **53**(1), pp. 337–340.

[52] Maeda, G. J., Sato, K., Hashizume, H., and Shinshi, T., 2006. "Control of an XY nano-positioning table for a compact nano-machine tool". *JSME International Journal, Series C: Mechanical Systems, Machine Elements and Manufacturing,* **49**(1), pp. 21–7.

[53] Kang, D., Kim, K., Kim, D., Shim, J., Gweon, D.-G., and Jeong, J., 2009. "Optimal design of high precision XY-scanner with nanometer-level resolution and millimeter-level working range". *Mechatronics,* **19**(4), pp. 562–570.

[54] Aoyama, T., Koizumi, K., Kakinuma, Y., and Kobayashi, Y., 2009. "Numerical and experimental analysis of transient state micro-bounce of aerostatic guideways caused by small pores". *CIRP Annals - Manufacturing Technology,* **58**(1), pp. 367–370.

[55] Chen, X., Chen, H., Luo, X., Ye, Y., Hu, Y., and Xu, J., 2011. "Air vortices and nano-vibration of aerostatic bearings". *Tribology Letters,* **42**(2), pp. 179–183.

[56] Butler, H., 2011. "Position control in lithographic equipment". *IEEE Control Systems Technology,* **31**(5), pp. 28–47.

[57] Awtar, S., 2004. "Analysis and synthesis of planer kinematic XY mechanisms". PhD thesis, Massachusetts Institute of Technology, Cambridge, MA.

[58] Awtar, S., Ustick, J., and Sen, S., 2011. "An XYZ parallel kinematic flexure mechanism with geometrically decoupled degrees of freedom". In ASME International Design Engineering Technical Conference, Vol. 6, pp. 119–126.

[59] Awtar, S., and Slocum, A., 2005. "Design of flexure stages based on a symmetric diaphragm flexure". In Proceedings of American Society for Precision Engineering, Annual Meeting No. 1803.

[60] Howell, L. L., Magleby, S. P., and Olsen, B. M., 2013. *Handbook of Compliant Mechanisms.* John Wiley & Sons, Inc.

[61] Schellekens, P., Rosielle, N., Vermeulen, H., Vermeulen, M., Wetzels, S., and Pril, W., 1998. "Design for precision: Current status and trends". *CIRP Annals - Manufacturing Technology,* **47**(2), pp. 557–586.

[62] Amick, H., Gendreau, M., and Gordon, C. G., 2002. "Facility vibration issues for nanotechnology research". In Symposium on Nano Device Technology, Citeseer, pp. 2–3.

[63] Awtar, S., and Slocum, A. H., 2006. "Constraint-based design of parallel kinematic XY flexure mechanisms". *Journal of Mechanical Design,* **129**(8), pp. 816–830.

[64] Hiemstra, D., Parmar, G., and Awtar, S., 2014. "Performance tradeoffs posed by moving magnet actuators in flexure-based nanopositioning". *Mechatronics, IEEE/ASME Transactions on,* **19**(1), pp. 201–212.

[65] Banik, R., and Gweon, D. G., 2007. "Design and optimization of voice coil motor for application in active vibration isolation". *Sensors and Actuators, A: Physical,* **137**(2), pp. 236–243.

[66] Yamada, T., Koganezawa, S., Aruga, K., and Mizoshita, Y., 1994. "A high-performance and low-profile moving-magnet actuator for disk drives". *IEEE Transactions on Magnetics,* **30**(6), pp. 4227–4229.

[67] Braune, S., and Liu, S., 2005. "Design of a novel moving magnet linear motor for use as a valve actuator". In 31st Annual Conference of the IEEE Industrial Electronics Society, pp. 2041–2046.

[68] Smith, S. T., and Seugling, R. M., 2006. "Sensor and actuator considerations for precision, small machines". *Precision Engineering,* **30**(3), pp. 245–64.

[69] Huber, J. E., Fleck, N. A., and Ashby, M. F., 1997. "The selection of mechanical actuators based on performance indices". *Proceedings of the Royal Society of London. Series A: Mathematical, Physical and Engineering Sciences,* **453**(1965), pp. 2185–2205.

[70] Furukawa, E., Mizuno, M., and Doi, T., 1995. "Development of a flexure-hinged translation mechanism driven by two piezoelectric stacks". *JSME International Journal, Series C,* **38**(4), pp. 743–8.

[71] Kim, J.-J., Choi, Y.-M., Ahn, D., Hwang, B., Gweon, D.-G., and Jeong, J., 2012. "A millimeter-range flexure-based nano-positioning stage using a self-guided displacement amplification mechanism". *Mechanism and Machine Theory,* **50**(0), pp. 109–120.

[72] Woody, S. C., and Smith, S. T., 2004. "Performance comparison and modeling of PZN, PMN, and PZT stacked actuators in a levered flexure mechanism". *Review of Scientific Instruments,* **75**(4), pp. 842–848.

[73] Higuchi, T., Yamagata, Y., Furutani, K., and Kudoh, K., 1990. "Precise positioning mechanism utilizing rapid deformations of piezoelectric elements". In IEEE Micro Electro Mechanical Systems, pp. 222–226.

[74] Uchino, K., 1998. "Piezoelectric ultrasonic motors: Overview". *Smart Materials and Structures,* **7**(3), pp. 273–285.

[75] Verma, S., Shakir, H., and Kim, W.-J., 2006. "Novel electromagnetic actuation scheme for multiaxis nanopositioning". *IEEE Transactions on Magnetics,* **42**(8), pp. 2052–2062.

[76] Youm, W., Jung, J., Lee, S., and Park, K., 2008. "Control of voice coil motor nanoscanners for an atomic force microscopy system using a loop shaping technique". *Review of Scientific Instruments,* **79**(1), pp. 013707–6.

[77] Tat Joo, T., Chen, I. M., Guilin, Y., and Wei, L., 2008. "A flexure-based electromagnetic linear actuator". *Nanotechnology,* **19**(31), pp. 1–10.

[78] Vrijsen, N. H., Jansen, J. W., and Lomonova, E. A., 2010. "Comparison of linear voice coil and reluctance actuators for high-precision applications". In 14th International Power Electronics and Motion Control Conference, pp. S329–S336.

[79] Yao, B., Hu, C., Hong, Y., and Wang, Q., 2007. "Precision motion control of linear motor drive systems for micro/nano-positioning". In International Conference on Integration and Commercialization of Micro and Nanosystems, Vol. B, ASME, pp. 1605–1614.

[80] Lee, M. G., Lee, S. Q., and Dae-Gab, G., 2004. "Analysis of halbach magnet array and its application to linear motor". *Mechatronics,* **14**(1), pp. 115–28.

[81] de Boeij, J., Lomonova, E., Duarte, J. L., and Vandenput, A. J. A., 2008. "Contactless power supply for moving sensors and actuators in high-precision mechatronic systems with long-stroke power transfer capability in XY plane". *Sensors and Actuators A: Physical,* **148**(1), pp. 319–328.

[82] Freudenberg, J. S., and Looze, D. P., 1988. *Frequency Domain Properties of Scalar and Multivariable Feedback Systems*, Vol. 70 of *Lecture Notes in Control and Information Sciences 104*. Springer-Verlag, Berlin.

[83] Clark, R. E., Smith, D. S., Mellor, P. H., and Howe, D., 1995. "Design optimization of moving-magnet actuators for reciprocating electro-mechanical systems". *IEEE Transactions on Magnetics,* **31**(6), pp. 3746–3748.

[84] Patt, P. J., 2002. *Frictionless motor material testing.* U.S. Patent Number: 6405599, Bose Corporation.

[85] Bolton, H. R., 1994. "Design aspects of electromagnetic actuators". In IEE Colloquium on Magnetic Materials for Sensors and Actuators, Vol. 6, pp. 1–5.

[86] Furlani, E. P., 2001. *Permanent Magnet and Electromechanical Devices.* Academic Press, New York.

[87] *Product Model # NCM03-06-005-5JB.* H2W Technologies. [Web Link].

[88] *Product Model # NCM05-28-180-2LB.* H2W Technologies. [Web Link].

[89] *Product Model # 6033.* Magnetic Innovations. [Web Link].

[90] *Product Model # LA16-19-001A.* Bei Kimko Magnetics. [Web Link].

[91] Moser, M. A., 1996. "Shorted turn effects in rotary voice coil actuators". *Magnetics, IEEE Transactions on,* **32**(3), pp. 1736–1742.

[92] Jansen, J. W., Lomonova, E. A., and Rovers, J. M. M., 2009. "Effects of eddy currents due to a vacuum chamber wall in the airgap of a moving-magnet linear actuator". *Journal of Applied Physics,* **105**(7), pp. 07–111.

[93] Coey, J. M. D., 1996. *Rare-Earth Iron Permanent Magnets.* Oxford University Press, New York.

[94] *SiGNUM™RELM high accuracy linear encoder.* Renishaw Inc. [Web Link].

[95] Hiemstra, D. B., 2014. "Design of the moving magnet actautors for flexure based nanopositioning". Master's thesis, University of Michigan, Ann Arbor, MI.

[96] Awtar, S., Slocum, A. H., and Sevincer, E., 2007. "Characteristics of beam-based flexure modules". *Transactions of the ASME, Journal of Mechanical Design,* **129**(6), pp. 625–39.

[97] Sun, Y., Ho, Y.-S., and Yu, L., 2009. "Dynamic stiffnesses of active magnetic thrust bearing including eddy-current effects". *Magnetics, IEEE Transactions on,* **45**(1), pp. 139–149.

[98] Hiemstra, D., Parmar, G., Welch, C., and Awtar, S., 2013. *Electromagnetic Actuators and Component Designs Therefor.* Provisional Patent, US Application Number: 61801212.

[99] Parmar, G., Barton, K., and Awtar, S., 2014. "Large dynamic range nanopositioning using iterative learning control". *Precision Engineering,* **38**(1), pp. 48–56.

[100] Longman, R. W., 2000. "Iterative learning control and repetitive control for engineering practice". *International Journal of Control,* **73**(10), pp. 930–54.

[101] Otten, G., de Vries, T. J. A., van Amerongen, J., Rankers, A. M., and Gaal, E. W., 1997. "Linear motor motion control using a learning feedforward controller". *IEEE/ASME Transactions on Mechatronics,* **2**(3), pp. 179–187.

[102] Steinbuch, M., and Molengraft, M. J. G. V. D., 2000. "Iterative learning control of industrial motion systems". In 1st IFAC Conference on Mechatronic Systems, pp. 967–972.

[103] Fujita, T., KONO, D., MATSUBARA, A., YAMAJI, I., and IBARAKI, S., 2007. "Dynamic characteristics and positioning performance of piezoactuator-integrated ball screw drive". In Proceedings of the 4th International Conference on Leading Edge Manufacturing in 21st Century, no. 07–205, pp. 507–510.

[104] Signal processing toolbox™user's guide. Tech. note, MathWorks Inc. [Web Link].

[105] Bristow, D. A., Tharayil, M., and Alleyne, A. G., 2006. "A survey of iterative learning control". *IEEE Control Systems Magazine,* **26**(3), pp. 96–114.

[106] Norrlf, M., and Gunnarsson, S., 2002. "Time and frequency domain convergence properties in iterative learning control". *International Journal of Control,* **75**(14), pp. 1114–1126.

[107] Heinzinger, G., Fenwick, D., Paden, B., and Miyazaki, F., 1992. "Stability of learning control with disturbances and uncertain initial conditions". *Automatic Control, IEEE Transactions on,* **37**(1), pp. 110–114.

[108] Fleming, A. J., and Wills, A. G., 2009. "Optimal periodic trajectories for band-limited systems". *IEEE Transactions on Control Systems Technology,* **17**(3), pp. 552–62.

[109] Merry, R., van de Molengraft, R., and Steinbuch, M., 2006. "Removing non-repetitive disturbances in iterative learning control by wavelet filtering". In American Control Conference, pp. 226–231.

[110] Awtar, S., and Parmar, G., 2013. "Design of a large range XY nanopositioning system". *Journal of Mechanisms and Robotics,* **5**(2), pp. 021008–10.

[111] Skogestad, S., and Postlethwaite, I., 1996. *Multivariable feedback control: analysis and design.* John Wiley & Sons, Inc.

[112] Hoagg, J. B., and Bernstein, D. S., 2007. "Nonminimum-phase zeros: Much to do about nothing – classical control revisited, Part II". *IEEE Control Systems Magazine,* **27**(3), pp. 45–57.

[113] Kim, D., Kang, D., Shim, J., Song, I., and Gweon, D., 2005. "Optimal design of a flexure hinge-based XYZ atomic force microscopy scanner for minimizing abbe errors". *Review of Scientific Instruments,* **76**(7), pp. 073706–7.

[114] Choi, K.-B., and Lee, J. J., 2005. "Passive compliant wafer stage for single-step nano-imprint lithography". *Review of Scientific Instruments,* **76**(7), pp. 075106–6.

[115] Kota, S., Joo, J., Li, Z., Rodgers, S. M., and Sniegowski, J., 2001. "Design of compliant mechanisms: applications to MEMS". *Analog Integrated Circuits and Signal Processing,* **29**(1-2), pp. 7–15.

[116] Kim, G.-W., and Kim, J., 2013. "Compliant bistable mechanism for low frequency vibration energy harvester inspired by auditory hair bundle structures". *Smart Materials and Structures,* **22**(1), pp. 014005–6.

[117] Dwivedy, S. K., and Eberhard, P., 2006. "Dynamic analysis of flexible manipulators, a literature review". *Mechanism and Machine Theory,* **41**(7), pp. 749–777.

[118] Crespo Da Silva, M. R. M., 1998. "A reduced-order analytical model for the nonlinear dynamics of a class of flexible multi-beam structures". *International Journal of Solids and Structures,* **35**(25), pp. 3299–3315.

[119] Crespo Da Silva, M. R. M., 1988. "Non-linear flexural flexural torsional extensional dynamics of beams .1. formulation". *International Journal of Solids and Structures,* **24**(12), pp. 1225–1234.

[120] Crespo Da Silva, M. R. M., 1988. "Non-linear flexural flexural torsional extensional dynamics of beams .2. response analysis". *International Journal of Solids and Structures,* **24**(12), pp. 1235–1242.

[121] Howell, L. L., 2001. *Compliant mechanisms.* Wiley-Interscience.

[122] Saxena, A., and Ananthasuresh, G. K., 2001. "Topology synthesis of compliant mechanisms for nonlinear force-deflection and curved path specifications". *Journal of Mechanical Design,* **123**, p. 33.

[123] Lan, C.-C., and Lee, K.-M., 2005. "Dynamic model of mechanisms with highly compliant members". In ASME International Mechanical Engineering Congress and Exposition, Dynamic Systems and Control Division, Vol. 74, pp. 1743–1750.

[124] Wang, W., and Yu, Y., 2008. "Dynamic analysis of compliant mechanisms using the finite element method". In IEEE/ASME International Conference on Advanced Intelligent Mechatronics, pp. 247–251.

[125] Akano, T. T., and Fakinlede, O. A., 2013. "An effective finite element method for beam based compliant mechanism". *International Journal of Engineering and Technology,* **3**(4), pp. 407–419.

[126] Shilpiekandula, V., and Youcef-Toumi, K., 2008. "Characterization of dynamic behavior of flexure-based mechanisms for precision angular alignment". In IEEE American Control Conference, pp. 3005–10.

[127] Yue-Qing, Y., Howell, L. L., Lusk, C., Ying, Y., and Mao-Gen, H., 2005. "Dynamic modeling of compliant mechanisms based on the pseudo-rigid-body model". *Transactions of the ASME, Journal of Mechanical Design,* **127**(4), pp. 760–5.

[128] Boyle, C., Howell, L. L., Magleby, S. P., and Evans, M. S., 2003. "Dynamic modeling of compliant constant-force compression mechanisms". *Mechanism and Machine Theory,* **38**(12), pp. 1469–1487.

[129] Nayfeh, A., and Mook, D., 2008. *Nonlinear Oscillations.* Wiley.com.

[130] Spector, V. A., and Flashner, H., 1990. "Modeling and design implications of noncollocated control in flexible systems". *Transactions of the ASME, Journal of Dynamic Systems, Measurement and Control,* **112**(2), pp. 186–93.

[131] Miu, D. K., 1991. "Physical interpretation of transfer function zeros for simple control systems with mechanical flexibilities". *Transactions of the ASME, Journal of Dynamic Systems, Measurement and Control,* **113**(3), pp. 419–24.

[132] Tohyama, M., and Lyon, R. H., 1989. "Zeros of a transfer function in a multidegree-of-freedom vibrating system". *Journal of the Acoustical Society of America,* **86**(5), pp. 1854–63.

[133] Loix, N., Kozanek, J., and Foltete, E., 1996. "On the complex zeros of non-colocated systems". *Journal of Structural Control,* **3**(1-2), pp. 79–87.

[134] Awtar, S., Sood, S., and Olfatnia, M., 2012. *Linear Flexure Bearing Designs with high Off-axis Stiffness.* Provisional Patent, US Application Number: 793530481.

[135] Varanasi, K. K., and Nayfeh, S. A., 2006. "Damping of flexural vibration using low-density, low-wave-speed media". *Journal of Sound and Vibration,* **292**(1), pp. 402–414.

[136] Book, W. J., 1993. "Controlled motion in an elastic world". *Journal of Dynamic Systems, Measurement and Control, 50th Anniversary Issue*, pp. 252–261.

[137] Lee, C., and Salapaka, S. M., 2009. "Robust broadband nanopositioning: fundamental trade-offs, analysis, and design in a two-degree-of-freedom control framework". *Nanotechnology,* **20**(3), p. 035501.

[138] Aphale, S. S., Bhikkaji, B., and Moheimani, S. R., 2008. "Minimizing scanning errors in piezoelectric stack-actuated nanopositioning platforms". *Nanotechnology, IEEE Transactions on,* **7**(1), pp. 79–90.

[139] Tomizuka, M., 1987. "Zero phase error tracking algorithm for digital control". *Transactions of ASME, Journal of Dynamic Systems, Measurement, and Control,* **109**, pp. 65–68.

[140] Sebastian, A., and Salapaka, S. M., 2005. "Design methodologies for robust nano-positioning". *Control Systems Technology, IEEE Transactions on,* **13**(6), pp. 868–876.

[141] Koren, Y., and Lo, C.-C., 1991. "Variable-gain cross-coupling controller for contouring". *CIRP Annals of Manufacturing Technology,* **40**(1), pp. 371–374.

[142] Barton, K. L., and Alleyne, A. G., 2008. "A cross-coupled iterative learning control design for precision motion control". *Control Systems Technology, IEEE Transactions on,* **16**(6), pp. 1218–1231.

[143] De Silva, C., 2005. *Mechatronics: An Integrated Approach.* CRC Press Inc.

[144] Schaeffer, R., 2012. *Fundamentals of Laser Micromachining.* Taylor & Francis.

[145] Application note 13: Voltage to current conversion. Tech. note, Apex Microtechnology. [Web Link].

[146] Rapuano, S., Daponte, P., Balestrieri, E., De Vito, L., Tilden, S. J., Max, S., and Blair, J., 2005. "ADC parameters and characteristics". *IEEE Instrumentation & Measurement Magazine,* **8**(5), pp. 44–54.